4-23-2020 11:00 AM

# Strategies for Ultraprecise Single Point Cutting of V-grooves

Delfim A C Joao, *The University of Western Ontario*

Supervisor: Tutunea-Fatan, Remus, *The University of Western Ontario*
Joint Supervisor: Bordatchev, Evgueni, *The University of Western Ontario*
A thesis submitted in partial fulfillment of the requirements for the Master of Engineering
Science degree in Mechanical and Materials Engineering
© Delfim A C Joao 2020

# Abstract

V-groove microstructures have found numerous functionalization applications in mechanical, electronic, photonic, biomechanical and optical components. However, despite their wide use, the manufacturing processes associated with their fabrication are limited to axial strategies with a constant depth of cut that do not allow the control of the cutting force and cutting time, and therefore leading to significant micro-burrs as well as an inability to fabricate high aspect ratio grooves. The current thesis addresses this problem with the development of three cutting strategies that make use of a single point cutting process. The study to be detailed herein includes analytical, numerical and experimental approaches with respect to cross-sectional area calculations, tool path planning, finite element modelling as well as experimental measurements of the cutting force and surface roughness. The results revealed that a relationship exists between the number of passes/depth of cut and the magnitude of cutting force as measured along the feed direction as well as the existence of a relationship between chip thickness and surface quality. The developed cutting strategies proved to be efficient in manufacturing of symmetrical V-groove microstructures and augmented the field of micromachining with alternative cutting strategies.

## Keywords

# Summary for Lay Audience

The increase in convenience and value of many industrial and household products due to their size and weight reduction over the years has triggered rapid development of the micromachining field. The functionalization of these products - a procedure through which microstructures are added on a surface of the product to enhance some of its properties such as optical and thermal - receives a growing attention in micromachining because of the enhanced capabilities added to the part's surface. Among the different microstructures used for functionalization purposes, V-grooves stand out due to their applications in the enhancement of many components in different fields. V-groove structures have found numerous applications in mechanical, electronic, photonic, biomechanical and optical components. However, despite their wide use, their manufacturing processes are limited to an axial cutting strategy with a constant depth of cut that does not allow controlling cutting force and cutting time, and therefore it leads to significant micro-burrs and inability to fabricate high aspect ratio grooves. To address these issues, three cutting strategies are developed in this thesis, having each two implementations for cutting: constant chip thickness and constant cutting area. The three strategies are divided into one axial and two non-axial cutting strategies. The development of each cutting strategy on its two implementations included a cutting mechanics model for material removal, post-processor, finite element analysis and experimental verification for a single groove. The results of this work revealed that a relationship exists between the number of passes/depth of cut and the magnitude of cutting force as measured along the feed direction as well as the existence of a relationship between the chip thickness and surface quality. The developed cutting strategies proved to be efficient in manufacturing of a single ultraprecise symmetrical V-groove microstructure with areal surface quality and have improved the micromachining field with alternative cutting strategies.

# Dedication

To the Creator of all I know; the good and faithful One.

"And whatever you do, whether in

word or deed, do it all in the name

of the Lord Jesus, giving thanks to

God the Father through him."

# Acknowledgments

My warmest thanks are directed to my supervisors Dr. O. Remus Tutunea-Fatan and Dr. Evgueni Bordatchev, as well as to my research colleague Mr. Nicolas Milliken for their limitless support and wealth of knowledge. I am grateful to have been given the opportunity to pursue a master's degree under the guidance and care of people such as yourselves. Dr. Tutunea-Fatan, I appreciate your promptness to receive me as a research assistant, giving me the opportunity to be part of such an amazing team. Moreover, I will always hold dear your prompt availability and willingness to assist me will all my inquiries, allowing to grow as a researcher. Dr. Bordatchev, I appreciate your guidance and experience with technical research, your critical insights and innovative ideas are inspiring. I will always hold valuable your instructions and insights that allowed me to be enriched in research knowledge beyond the scope of our research applications. Milliken, I appreciate your mentorship, patience and willingness to help me with all my enquiries. I would be unable to express my gratitude and appreciation if I tried to put in words how valuable your help and mentorship are to me.

I further my thankfulness to my colleague Otoniel Rangel for his support and motivation in completing all the research done for this work. It was a pleasure to work along your side. Finally, I would like to thank my family, friends, and loved ones for their support. Your motivation, support and generosity are truly appreciated.

# Table of Contents

# List of Tables

# List of Figures

xi

# List of Abbreviations

| | |
|---|---|
| BC | Boundary Condition |
| CAD | Computer Aided Design |
| CAM | Computer Aided Manufacturing |
| CCA | Constant Cutting Area |
| CCT | Constant Chip Thickness |
| CNC | Computer Numerical Control |
| NC | Numerical Control |
| DAQ | Data Acquisition |
| FEA | Finite Element Analysis |
| WCS | Workpiece Coordinate System |

# List of Symbols

| | |
|---|---|
| $A_{th}$ | Cutting Area |
| $\delta_{th}$ | Chip Thickness |
| $d_i$ | Depth of Cut |
| $\alpha$ | Tool Included Angle |

Chapter 1

# 1 Introduction

This chapter will provide a general introduction on V-grooves, some of their major applications as well as literature review on their current manufacturing processes. This will be followed by a comprehensive explanation of the motivation for the current thesis, its purpose and contribution to the field of micromachining. Finally, and overview of the subsequent chapters will be presented.

## 1.1 V-grooves and major applications

The significance of microfabrication is directly related to the increase in convenience and value of many industrial and household-use products influenced by the size and weight reduction of these products [1]. Generally speaking, microfabrication relies on precision cutting, defined as a cutting technique that enables the production of components with micrometer or submicrometer form accuracy and surface roughness within tens of a nanometer [2]. The functionalization of the surfaces of the previously mentioned products - a procedure through which microstructures are added on a surface of the product to enhance some of its properties such as optical and thermal - received a recent growing attention in micromachining because of the benefits provided to products. Among the different structures used to improve the functionalization of numerous products, V-groove structures play an important role, primarily due to the enhancements brought to many components involved in different applications. V-groove features have found numerous uses in mechanical, electronic, photonic, biomechanical and optical components [1].

### 1.1.1 Anisotropic Surfaces

Anisotropic surfaces for directional water motion have attracted enormous research attention owed to their various applications from fundamental to practical aspects such as liquid transportation [3], water-directional collection [4], drag reductions[5], and microfluidic devices [6]. For ideal solid surfaces (i.e., perfectly smooth, chemically homogeneous, rigid, insoluble, and nonreactive surfaces), the wetting characteristics are

defined as a function of the interfacial free energies [7]. Despite this, most of the real/natural surfaces, fabricated in laboratories and processed by different technologies are rough and/or chemically heterogenous. In broad terms, strategies for the fabrication of anisotropic surfaces are mainly focused on the regulation of chemical heterogeneity [8], as well as the introduction of anisotropic micro/nanostructures onto surfaces [9]. The second focus will be summarized further.

To achieve the anisotropic sliding of water droplets, two criteria must be satisfied: (1) the surface must be easy for water droplets to slide; (2) and there must be anisotropic structures on the surface to guide the directional sliding of water droplets. To meet the second criterion, periodic micro-grooves [10] are often used as powerful structures that can provide the anisotropic structure with the advantages of simple fabrication, large-area capability, and flexibility.
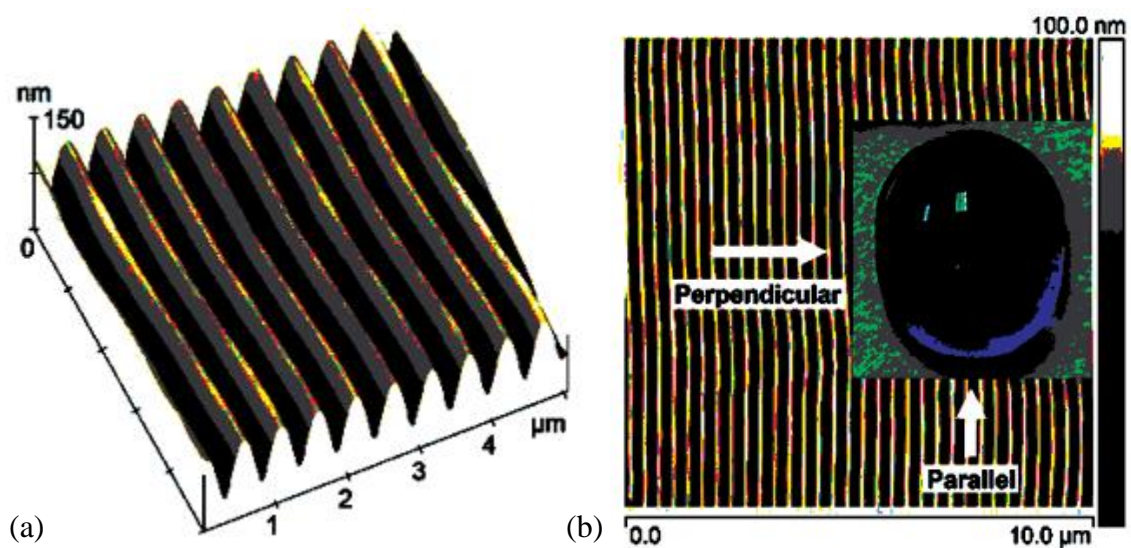


**Figure 1.1: Topographical AFM image of the grooved structure:**
**(a) Three-dimensional image; (b)and top view (inset) of a 5 μL water drop [7]**

Structural gradients of surfaces can direct the motion of water droplets by gradually changing the periods of micro-grooves [11] or the width and spacing of micro-pillars simultaneously [12]. Although these gradient surfaces are promising, most of them are characterized by a slow motion of water droplets. Moreover, the rapid rolling of water

droplets is attributed to high contact angles (> 150°), and low contact angle hysteresis (<10°) [13], that are accomplished thorough an anisotropic arrangement of hierarchical micro/nanostructures forming anisotropic superhydrophobic surfaces.

Zhao et al [7], by studying wetting characteristics on patterned surfaces through measurements of contact angles discovered that macroscopic distortion of water drops was found on such small-scale surface structures, and the contact angles measured from the direction parallel to the grooves were larger than those measured from the perpendicular direction (Figure 1.1). Furthermore, with increasing groove depth, both the degree of wetting anisotropy and the contact angle hysteresis (perpendicular to the grooves) increased because of the increase in the energy barrier. The theoretical critical value of the groove depth, above which the anisotropic wetting appears, was determined by Zhao et al [7] to be 16 nm for the grooved surface with a wavelength of 396 nm [7, 14]. Liu et al [14] concluded that unless the spacing between grooves is very large (>100µm), the parallel-grooved surface feature normally increases the apparent wetting behavior of the droplets.

Finally, the preliminary results observed with the application of microgrooves on anisotropic surfaces showed promise for water drainage enhancement by economically changing the morphology of the surface. Smaller groove spacing, larger depth and steeper groove sidewalls were observed to be favorable for drainage enhancement [14], therefore guiding the efforts to improve the fabrication techniques in this direction.

## 1.1.2    Cell Migration

The growing percentage of elderly people in the population - translating into an increase of patients suffering from geriatric diseases - has triggered the production and use of implants for their treatment [15]. Within the medical context it is known that for implant devices, final tissue reaction towards an implanted device is greatly influenced by the initial reaction of cells towards the device [15]. Therefore, studies performed during the past two decades have focused on acquiring an understanding of the interactions between different cells and tissues of the body and implant materials. It is important that the implant material used fits in and functions in a living organism. For instance, when

implants are placed in the soft tissues of the body, minimal capsule formation around the implant, and implant migration are desired [15]. Past research in this field [16] has found that microgrooves influence cell behavior: cells align themselves and migrate guided by the surface of the grooves (Figure 1.2).
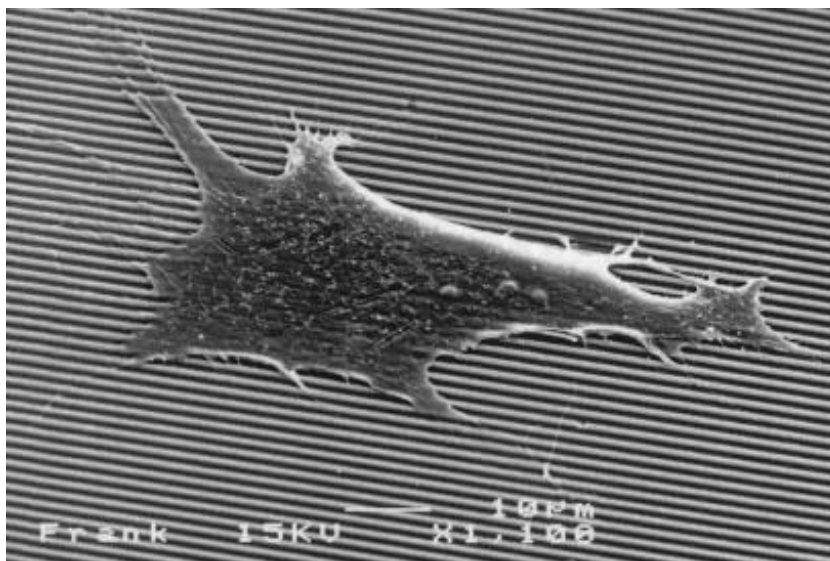


**Figure 1.2: Scanning electron micrograph, showing alignment of fibroblast cell on a microgrooved substrate surface [15]**

Over the years, some critical conclusions have been reached throughout the studies involving microgrooves on implants. Curtis and colleagues [17, 18] have found that groove depth was more important in the establishment of cell alignment than groove width and pitch. Supported by these results, and in agreement with Dunn and Brown [19] they suggest that cytoskeletal flexibility and success in making a cellular protrusion are the most likely properties of cells to result in topographic guidance. Dalton et al [20] found that cellular extensions generally follow the microgroove direction by tracking along the top of the ridges or following the ridge walls.

On the basis of a previous study, Walboomers et al [21] suggested that the contact guidance phenomenon is probably based on mechanical clues [22]. The breakdown and formation of fibrous cellular components is influenced by microgrooves by creating a pattern of mechanical stress, which influences cell spreading and causes cell alignment.

Additionally, these researchers noticed that the extracellular matrix (ECM) possesses certain specific mechanical properties. Many in vitro studies already indicated that cell-generated forces of tension can actually reorganize the organization of the ECM into structures that direct the behavior of single cells [23, 24]. As cells cannot penetrate narrow (<2 µm) or deep (>0.5 µm) grooves, and only attach to the ridge surface [25, 26] the exerted forces can achieve a reorganization of deposited ECM proteins. Consequently, this will have an effect on cellular spreading and elongation. In this way, alignment, and directed cell migration will be established [21].

The effect of microgrooves on surface of implants may conduct to other possible applications in the medical field. For example, microgrooved surfaces can perhaps be applied to membranes used for the guided tissue regeneration (GTR) techniques employed in periodontology. Because microgrooves orient the migration of cells, they may be useful for the support of the healing of large tissue defects, such as cleft palates, and for enhancing the repair of highly oriented structures such as nerve bundles and tendons [15].

## 1.1.3  Light Guiding

Most liquid crystal display (LCD) devices are passive devices in which images are displayed by controlling an amount of light inputted from an external light source. Thus, a separate light source (for example, backlight module) is generally employed for illuminating an LCD panel [27].

Generally, backlight modules include a light source, a light guide plate, a reflective sheet, and a diffusion sheet. The light guide plate includes a light incident surface, a light emitting surface adjoining the light incident surface, and a bottom surface facing an opposite direction of the light emitting surface. The light source is located adjacent to the light incident surface of the light guide plate. The light guide plate is located between the reflective sheet and the diffusion sheet with the bottom surface adjacent to the reflective sheet and the light emitting surface adjacent to the diffusion sheet. When light rays produced by the light source are emitted into the light guide plate, the light guide plate redirects the light rays. The light rays from the light source projected towards the

reflective sheet are reflected towards the light guide plate to increase the utilization efficiency of light energy. The diffusion sheet diffuses the light rays emitted from the light emitting surface of the light guide plate and thus the brightness of the light incident on the LCD panel would end up being more uniform [28].

The light incident surface defines a plurality of V-shaped grooves perpendicular to the light emitting surface. Light rays produced by a light source are emitted into the light guide plate via the light incident surface, the light rays are reflected at the bottom surface and are then emitted out from the light emitting surface of the light guide plate. However, when the light source is a point light source, a plurality of dark and bright areas are generated unavoidably adjacent the light incident surface, thus decreasing the optical uniformity [29].
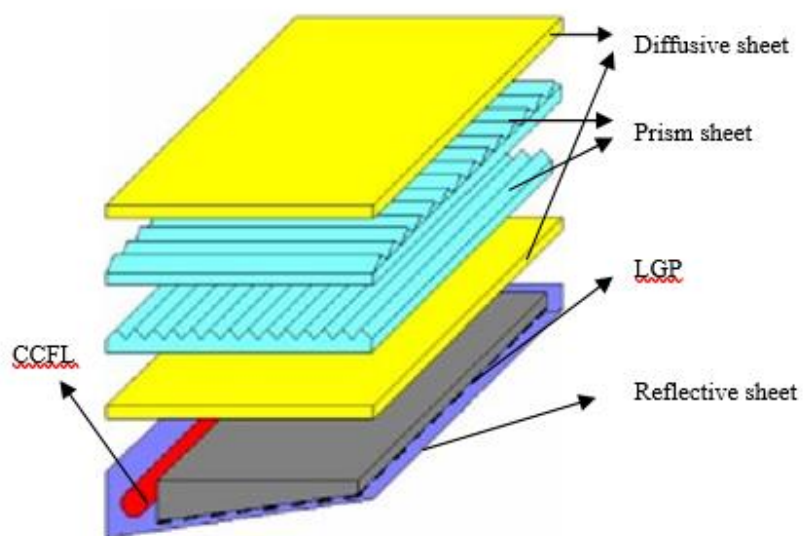


**Figure 1.3: Traditional backlight module [28]**

Injection molding technique is generally applied to fabricate the traditional light guiding plate. However, Chien and Chen [28] apply MEMS and hot-embossing techniques to fabricate the concentric circle light guiding plate (CCLGP). The concentric circle V-groove structure and the micro-pyramid structure are constructed on the CCLGP. The V-groove structure and the micro-pyramid structure of the CCLGP are considered to alter

the direction of the light travels and to make light source emit in a direction perpendicular to the top surface of the CCLGP [30].

## 1.1.4 Optical fiber alignment

The manufacture of optoelectronic modules, such as optoelectronic receivers and optoelectronic transmitters requires that an optical fiber be properly aligned and fixed in an optical subassembly. In an optical receiver, a fiber is aligned with an optical detector. usually a PiN photodiode. In an optical transmitter, an optical fiber is aligned with a light- emitting diode (LED) or a laser diode. A goal of optical alignment is to maximize the amount of light coupling between the optical detector, LED or laser diode and the optical fiber. The alignment of the fiber member with the LED laser diode or optical detector is a critical step in the manufacture of an optoelectronic subassembly [31].

Optical subassemblies are often used in harsh environments where they are subjected to wide variations in temperature, pressure, and g-forces. To withstand such environments, such subassemblies are often mounted in hermetically sealed packages. Each package is adapted to mate with a connector that contains an optical fiber.
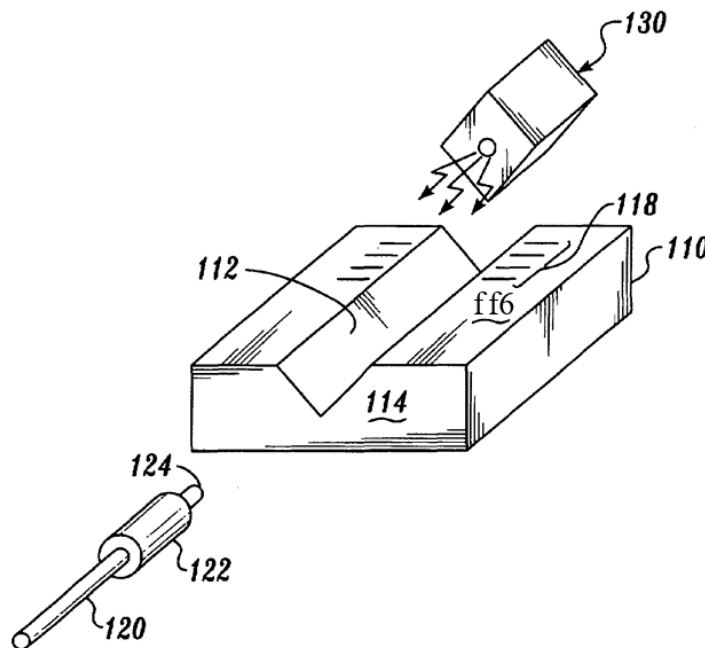


**Figure 1.4: Invention using V-grooves for optical fiber alignment [31]**

Typically, the connectors made by each manufacturer require a different type of latching mechanism to be mounted to the package. In addition to the problem of aligning the optical fiber with the optical detector, LED, or laser diode. it has also been difficult to produce a subassembly package that can be easily adapted to mate with a variety of optical connectors made by different manufacturers [31].

In optical fiber communication, there are a number of techniques being adapted for alignment of optical fiber passive elements. One is the fused biconical taper technique which aligns two optical fibers directly, then fuses the aligned fibers and stretches the fibers to connect the fiber cores at two ends together under the polymerization force effect. The connection made by this technique tends to cause power loss because the diameters of the coupling optical fibers could be no equal, the alignment of the fibers not precise, or the surfaces of the fiber connection ends not even and smooth [32].

As shown in Figure 1.4, V-grooves are incorporated in the solution to meet the need for a method of producing optical subassemblies in a cost- effective manner that does not require the active alignment of an optical fiber with an optical detector, LED, or laser diode. In addition, they are also useful in meeting the need for a subassembly package that is easily adapted to mate with a variety of connector types [31].

## 1.1.5    Retroflectors

Retroreflectors composed of micron-sized cube corner elements are widely used as reflectors on clothes for safety reasons or for measuring applications. Due to the small size of the individual reflector elements, structured films can be extensively flexed without affecting the geometry of each element too much so that it can still fulfill its function [33]. A retroreflector consists of three perpendicular mirrors as can be seen in Figure 1.5(a). A light beam with the unit vector ($n_x$, $n_y$, $n_z$) hits a reflecting surface in the $x$–$z$ plane in a Cartesian system and the sign of the $y$-component of the incoming beam vector is inverted. Therefore, the unit vector of the reflected beam will be ($n_x$, -$n_y$, nz). The multiple reflection in the $x$–$y$ and the $y$–$z$ plane leads to a beam vector in ($-n_x$, -$n_y$, $-n_z$) direction, parallel to the incoming beam but with reversed direction. The maximum offset of the beam is determined by the size of the individual retroreflector.
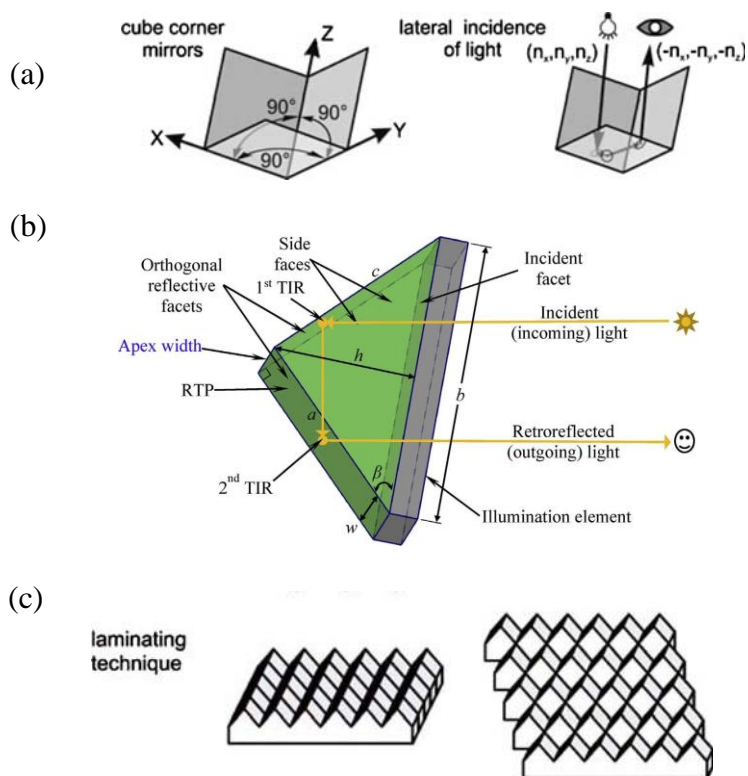
**Figure 1.5: (a) Cube corner retroreflector [33]; (b) design and functionality of the right triangular prism (RTP) retroreflector [34]; (c) laminated technique for retroreflectors [33]**

Fabrication of cube corner retroflectors is conventionally done by means of pin-bundling technique [35]. However, they could also be made by means of the laminating technique (Figure 1.5), in which V-grooves are fabricated on multiple workpieces and an offset is imposed on the assembly to generated cube corner retroreflectors. Novel techniques have been suggested for the manufacture of both cube corner retroreflectors [33] and right triangular prisms retroreflectors [34]. These novel techniques use either diamond micro chiseling or ultraprecise single point inverted cutting. In any case, generation of V-grooves with different tools orientations is a component of any of the novel techniques presented above.

## 1.1.6    Riblets

Research on drag reduction methodologies relevant to flight vehicles has received considerable attention during the past decades [36-38]. In the context of a civil or

commercial transport aircraft, depending on the size, viscous or skin friction drag accounts for about 40–50% of the total drag under cruise conditions. Payoff is generally high even with a small level of drag reduction [39]. There has been continuous and focused activity around the globe concerning development of new techniques for skin friction drag reduction [38]. Most of the past attempts have progressed broadly in two directions: methods for delaying laminar-turbulent boundary layer transition and methods for altering or modifying the turbulent structure of a turbulent boundary layer. The passive techniques that have been extensively investigated for turbulent drag reduction include riblets and large eddy break-up devices.
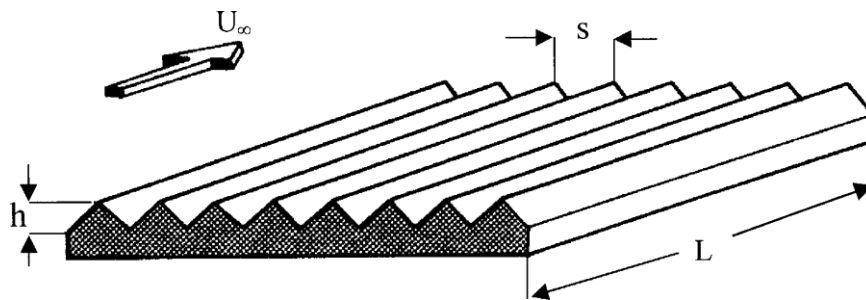


**Figure 1.6: Sketch of riblet geometry [36]**

Riblets, which are micro-grooves on the surface and aligned to the freestream direction (Figure 1.6), have been studied most extensively [36, 40] and the results from these studies have been sufficiently promising and encouraging that the concept has been evaluated in flight tests. Riblets with symmetric V-grooves (height equal to spacing) with adhesive backed film have been widely investigated earliest work and the results have revealed enormous consistency with regard to the degree of drag reduction as well as certain aspects of flow structure [36]. The introduction of grooves onto a surface can reduce drag by changing the near-surface flow structure [41]. Maximum viscous drag reduction in the range of 4–8% has been measured on a variety of two-dimensional flows with zero or mild pressure gradients [36].

## 1.2   Fabrication Methods

The processes used to manufacture V-grooves are mainly divided into two groups essentially involving rotational cutting tools and non-rotational ones [42, 43]. Both

manufacturing variants can produce V-groove microstructure with submicron dimensional accuracies and nanometric surface roughness. Past studies involving rotational tools noted that although this machining approach is very good for shape accuracy and surface quality, long slopes tend to be produced at the ends of the microgrooves [44]. By contrast, grooves generated with non-rotational tools revealed that the characteristic slopes that are present at the end of the microstructure are shorter. Furthermore, this cutting technique tends to be more versatile in a sense that it enables the generation of microgrooves with a broad variety of curvatures [44]. Moreover, the aforementioned slope reductions are primarily influenced by the tighter control of the tool and workpiece angle of entrance [44].

To date, V-grooves structures are produced through several fabrication methods such as fly-cutting [45], raster milling [46], precision grinding [47], and eletrondischarge machining [48] .

## 1.2.1   Fly-Cutting

The process of making V-groove microstructure by using fly-cutting is also known as fly-grooving, which is part of a single point diamond cutting technic. It uses a diamond tool that scratches the workpiece once during each rotation period of the cutter as shown in Figure 1.7 [49].
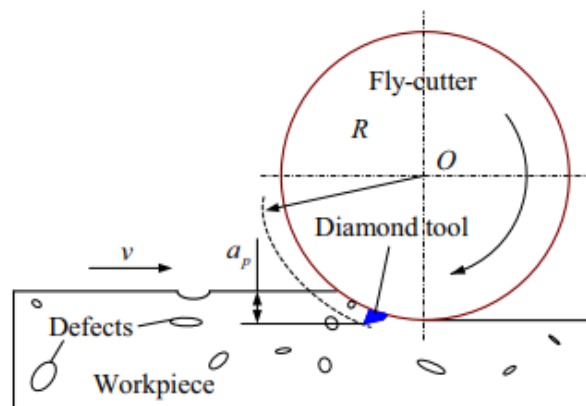


**Figure 1.7: Schematic of single-point diamond fly-cutting [49]**

Materials such as silicon, glass, and sapphire are now experiencing a growing use in applications pertaining semiconductor industry, infrared optics, optoelectronic, MEMS, bioengineering, because of their excellent thermal, chemical, and wear resistance [50]. However, machining them remains a considerably challenging task due to their low fracture toughness [51]. By using fly-cutting, high-quality surface damage-free and excellent surface roughness can be achieved on these materials [49].

Fly cutting is a promising and favorable machining method for brittle materials and the generated surfaces do not require any further finishing procedures, such as lapping or polishing [49]. Moreover, by using fly-cutting it is possible to machine free-form optical components maintaining and controlling shape deviations with the sub-micrometer range [52].

Zhao and Guo examined the kinematics of fly-cutting and built a mechanistic cutting force model [53]. Moreover, numerical simulations of fly-cutting revealed that this could result in high-pressure phase transformation, which is responsible for the ductile removal of silicon (Si) and silicon carbide (SiC) [54]. By conducting a series of diamond fly-cutting tests on single crystal germanium it was discovered that the rake angle of the tool significantly affected the surface quality of the workpiece. It was observed that tools with a large negative rake angle help to achieve a greater surface quality [18].

Fly-cutting, however, could leave defects called "burrs" on the surfaces during the manufacturing of V-grooves [49]. These burrs affect significantly the functionality of the component and could be formed as follows. In the initial stage, the chip formed in front of the cutting tool has a positive shear angle. With the advancement of the cutting tool toward the workpiece edge, the plastic zone around the primary shear zone is extended toward the edge. At this critical point, the shear angle becomes smaller and negative shear starts to occur. As the negative shear continues, the cutting edge causes the work material to pivot and the positive shear angle continues to decrease to near zero. With further advancement of the cutting tool, the work corner will continue to pivot with the chip and finally the chip will be deposited on the workpiece edges, thus forming a burr.

## 1.2.2    Raster Milling

The manufacturing process of microstructures such as V-grooves done through raster milling is called ultra-precision raster milling (UPRM). Raster milling is a modification of fly-cutting. In UPRM a single crystal diamond tool is located on the spindle and the workpiece is positioned by fixtures on the table. The motions of the diamond tool in UPRM include the rotations around the spindle axis and linear movement along ZM-axis and YM-axis of the machine coordinate system as illustrated in Figure 1.8 [46]. This process can directly produce a non-symmetric freeform surface with a nanometric surface finish and sub-micrometric from accuracy without the need for post-processing [46].
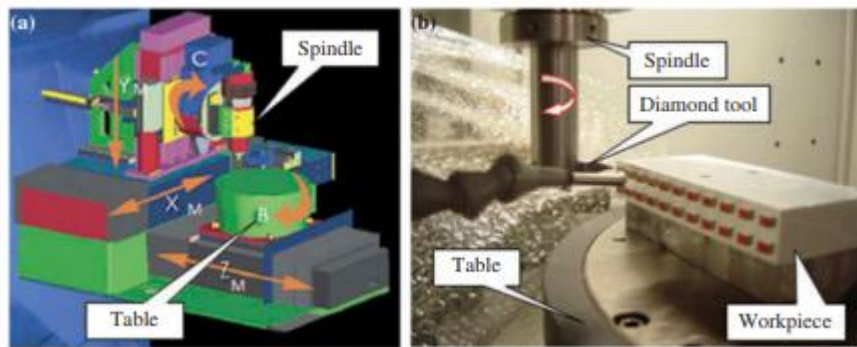


**Figure 1.8: Ultra-precision raster milling process of the freeform machine: (a) schematic of machine configuration and (b) ultra-precision raster milling process [46]**

The UPRM process in the fabrication of V-grooves contains much more freedom as compared with the precision grinding [46]. This is due to the fact that the achievable V-shape of the V-groove structure by precision grinding technology relies on the geometry of the wheel V-tip and the profile accuracy of the machined V-groove is affected by grinding wheel topography and the edge sharpness of the wheel [55].

By planning different tool paths in the fabrication of micro V-groove structures, ultra-precision raster milling technology with a single crystal diamond tool can achieve different types of V-shapes. Considering the ever-growing applications of UPRM in the fabrication of high-quality freeform surfaces, some researchers have focused on studying

the factors affecting surface generation in UPRM and developed prediction models for surface roughness and form accuracy [56].

Researchers attempted to predict the actual machining time during the process of precision cutting under the consideration of the acceleration and deceleration effect [57]. This was done due to the fact that the conventional method of machining time prediction is based on the numerical control (NC) program with the assumption that the cutting tool moves along a straight line with a constant feed rate [46]. This method was effective and widely employed in commercial computer-aided manufacturing (CAM) software for the applications in conventional machining, however, the conventional prediction method is not sufficiently precise for the application in ultra-precision machining [46].

Finally, by conducting experiments on an aluminum alloy workpiece, it was observed that the feed rate had a significant effect on surface roughness and the core pitch during ultra-precise raster milling [46]. It was observed that as the surface roughness followed a linear relationship with the feed rate. In order words, as the feed rate increased the surface roughness increased as well. The deviation from the core pitch, however, remained fairly consistent with the increase in the feed rate [46].

## 1.2.3    Precision Grinding

Precision grinding is the manufacturing process that essentially involves a grinding wheel, a spindle, and a workpiece. The cutting process is done by joining the rotating grinding wheel to the workpiece as illustrated in Figure 1.9. In the manufacturing of V-grooves, a diamond wheel is used which has a V-shape on its tip.
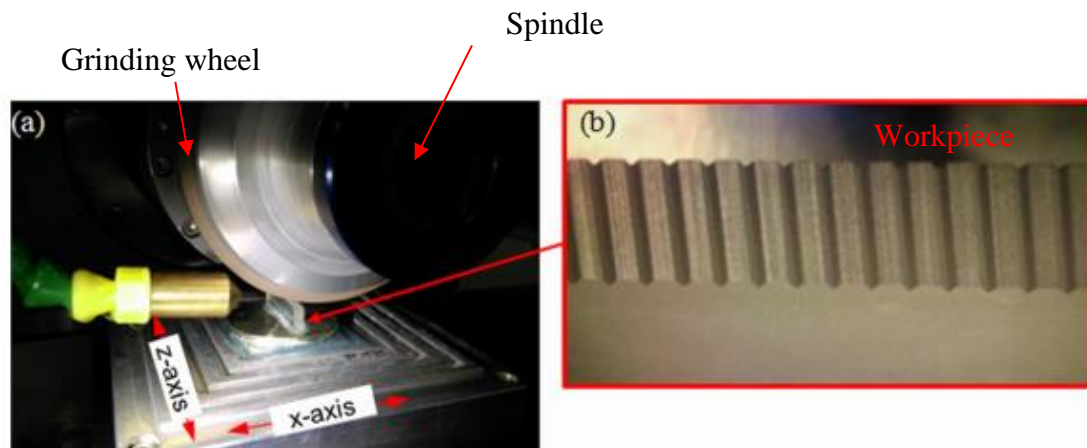
**Figure 1.9: Fabrication of V-grooves array in precision grinding machine (a) Machine process (b) The machined Component [47]**

Diamond grinding is an effective machining method for a wide range of hard non-ferrous materials with relatively low wheel wear [58]. For example, precision grinding of optical glasses has extended its applications in aerospace, automotive, semiconductor, and communication industry [47]. Furthermore, precision grinding was widely applied on the machining of aspheric surface, continuous and discontinuous freeform surface on brittle materials, which makes an improvement for the limitation of ultra-precision freeform machining technologies [47].

To achieve a low form error and surface roughness, research was conducted in diamond grinding of brittle materials which mostly focused on machining parameters effect, material removal mechanism, surface generation, grinding force, and subsurface damage as well as prediction models for surface finish. Furthermore, the high quality of a grinding process was observed to be highly dependent of a machine tool that meets the following requirements: precise, smooth, vibration, and backlash free motions, low levels of synchronous and asynchronous spindle errors, high static/ dynamic loop stiffness, and long-term thermal dimensional control [59].

When planning the grinding of micro V-grooves array, the rough, half rough, and finishing processes are designed with different grinding depths [47]. Moreover, in order

to obtain sub-micrometer from accuracy on the V-grooves the straightens and the positioning of the machine axis have to be carefully calibrated as well as the wheel profile have to be very accurate.

Finally, even though diamond grinding is a well-established machining process for a wide range of hard non-ferrous materials, offering the benefits of high material removal rates with relatively low wheel wear, it can be a time-consuming and hence expensive process.

## 1.2.4    Electrodischarge machining

The fabrication methods summarized above are seen as very effective techniques for machining microgrooves on metal and single crystalline materials. However, cutting harder materials, such as stainless steels, hardened alloys and ceramics materials tool wear becomes a critical problem. Yan et al [48] suggest alternative methods to fabricate microgrooves using micro-electrodischarge machining (μ-EDM) and micro-electrochemical machining (μ-ECM).

Yan et al [48] propose a two-step μ-EDM method for fabricating microgrooves with varied cross-sections. In the first step, a wire electrodischarge grinding (WEDG) technique is used to fabricate tool electrodes; in the second step, μ-EDM grooving tests are performed by using the WEDG-fabricated tool electrodes. In the second step, the tool electrode is rotated at a high speed (∼3,000 rpm) to generate a kind of "polishing effect" between the tool electrode and the workpiece.

Two methods of EDM are usable in the fabrication of microgrooves. One is to use a shaped block electrode, as shown in Figure 1.10(a). When feeding the block electrode against the workpiece, electrodischarges occur between the electrode and the workpiece, and a reverse shape can be then transcribed into the workpiece. This method is suitable for fabricating straight grooves with a uniform cross-section and depth. To generate longitudinally curved microgrooves or grooves having a varied depth and cross-sectional

shape, the preparation of the block electrode will be difficult.
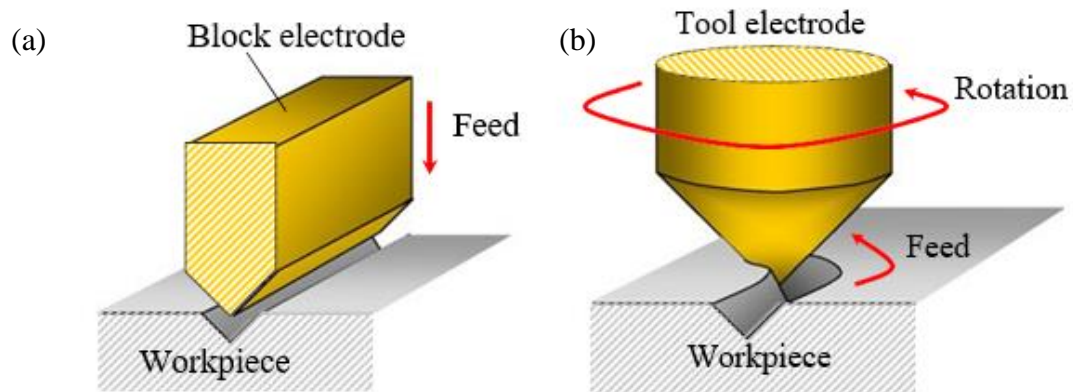


**Figure 1.10: Schematic of two EDM methods for fabricating microgrooves: (a) the conventional method using a shaped block electrode; (b) the proposed method using a rotating and three-dimensionally moving tool electrode [48]**

The other method, proposed by Yan et al [48] consists in using a high-speed rotating and moving tool electrode to generate microgrooves, as shown in Figure 1.10 (b). This method has excellent processing flexibility and enables the manufacturing of longitudinally curved microgrooves and grooves having varied cross-sections. In this method, preparation of the microtool electrodes is an important step. WEDG is used to fabricate the tool electrodes. A fine metal wire supported by a guiding wheel was used as the electrode to generate the objective shape on the tool electrode through electrodischarging. As the interference area between the wire and the tool electrode was extremely small, approaching a single point, complicated shapes could be freely generated on the tool electrode by precisely controlling the relative movement between the wire and the tool electrode. Additionally, during microgrooving by rotating the tool electrode at a high speed (~3,000 rpm), a kind of "polishing effect" is expected to take place.

Finally, it was observed that in WEDG, as electrodischarge energy decreased, tool electrode surface roughness and tool tip radius decreased too [48]. Moreover, it was also observed that the smallest tool tip radius was 1.1 µm, and the minimum surface roughness that could be generated with this process was 0.3 µm Ra [48]. This could pose

as a major disadvantage of this manufacturing process on certain V-groove applications which require much lower surface roughness. In addition to this, there is significant tool wear when high voltages are used [48].

## 1.3  Motivation

V-grooves represent one of the most useful microstructures to improve the functionality of numerous products. The range of their application is far from short as demonstrated in previous sections. However, surveyed literature revealed that little was reported so far on detailed fabrication techniques of such microstructures, making this a necessary research area to explore. In addition to this, each of the reported manufacturing processes is characterized by specific disadvantage that renders it inefficient for the specific use of microgrooves functionality. For example, the formation of burrs in fly cutting [49] and poor surface finish in eletrodischarge machining [48] could significantly affect the functionality of the microgrooves on applications such as optical fiber positioning and cell migration respectively.
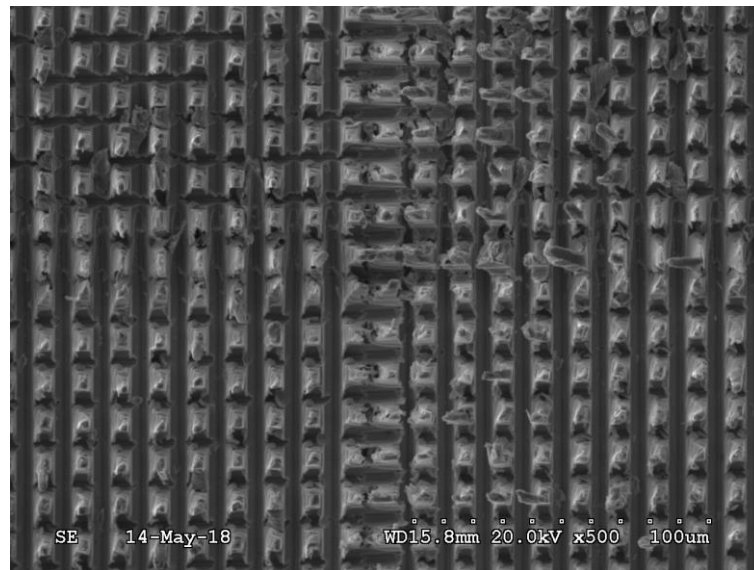


**Figure 1.11: SEM image of bent high aspect ratio V-groove tips manufactured with a conventional method**

In addition to specific disadvantages associated with each of the presented techniques, they all share in common the strategy of fabricating the micro grooves from its center.

Although this conventional approach may be satisfactory for microgrooves with low aspect ratio between the tip and valley angles, it is not efficient for high aspect ratio V-groove arrays. The conventional manufacturing strategies cutting from groove centers tend to cause the bend/breakage of the tips of the pyramids on high aspect ratio V-groove arrays. Figure 1.11 illustrates an SEM image of bent high aspect ratio V-groove tips manufactured with an included angle of 15°, a depth of 100 µm. The consequence of the aforementioned issues is critical as they affect the functionality of these microstructures. Finally, the disadvantages associated with conventional fabrications methods motivated the development of new material removal techniques to be outlined further in this work.

## 1.4   Objectives

Building on the conventional fabrication strategy for V-grooves (axial cutting strategy with constant chip thickness), this study has as a primary objective the development of three cutting strategies that use a single point cutting process. As illustrated in Figure 1.12, each cutting strategy has two implementations: cutting with constant chip thickens (CCT) and cutting with constant cutting are (CCA). The Development of each implementation in all cutting strategies included a cutting mechanics model, post-processor, FEA (finite element analysis) model and experimental verification for the fabrication of a single V-groove. The scope of this thesis was contained within the fabrication of a single V-groove as opposed to multi-groove fabrication. The cutting mechanics to be outlined for each implementation of a cutting strategy allows the calculation of material removed from the workpiece. The postprocessor will allow the conversion of tool path generated into machining code to be used during the experiments. The FEA models will allow the prediction of chip formation and cutting forces magnitudes, which will be further validated by means of experimental results.

The following chapters of this thesis contribute to the overall goal as follows. In the first chapter, starting with the implementation of the conventional strategy used to manufacture these microstructures (essentially involving cutting with a constant chip thickness from the center of the groove), a second variant of the same conventional strategy using a constant cutting area is implemented. In the first conventional

implementation, cutting forces present a linear trend [60] that could lead to tool breakage depending on the depth of the V-groove to be fabricated.
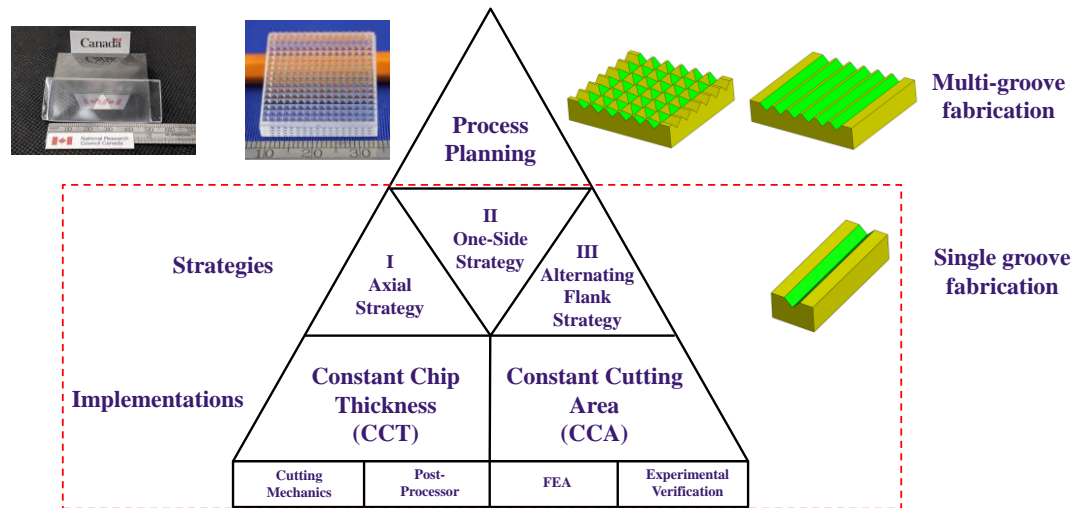


**Figure 1.12: Thesis objective and scope**

The second variant of the same axial strategy was developed to avoid the linear trend of the cutting force by aiming at a constant cutting force instead. This constant cutting force could bring advantages to the process related to tool wear/breakage, burr formation and surface quality. In the following chapter, a new strategy was developed by making use of a single flank of the tool. This non-axial cutting strategy was developed with the purpose of exploring cutting force reduction and burrs formation improvement that tend to be formed when both cutting edges of the tool are used (i.e., the case of the conventional axial strategy [49]). Finally, in the last chapter, alternating flank cutting was explored in order to investigate the effect of an alternate non-axial cutting strategy on cutting force magnitudes as well as surface roughness.

## 1.5  Contributions

The work presented on this thesis contributes to the field of micromachining with the development of new efficient ultraprecise single point cutting strategies to be used during microfabrication of V-grooves. The contribution to the field is tight with the objectives outlined previously, namely the development of mechanical models, finite elements models, post-processors and experimental verification.

The development of mathematical models associated with specific tool kinematics for material removal enables the understanding of the cutting mechanics associated with V-groove fabrication. The understanding of process cutting mechanics provides significant benefits when attempting to improve precision, increase tool life and avoid undesirable cutting forces. Developed and verified post-processors allow the optimization of cutting parameters that are critical for the control of cutting force magnitudes and generated surface roughness of V-groove microstructures. The developed finite elements models provide further insight in the cutting mechanics of each cutting strategy. Finally, the proposed experimental methodology sets a new standard for the fabrication of V-grooves by means of the ultraprecise single point cutting technology.

## 1.6   Thesis Overview

The organization of this thesis is relevant to its overall objective and each chapter configuration will follow an identical structure.

Chapter 2 presents an axial strategy to be used in the manufacturing of V-grooves. In this chapter, two variants are presented: one using a constant chip thickness (CCT) implementation and the other using a constant cutting area (CCA) implementation. The beginning of the presentation of each variant starts with the development of cutting mechanics model of the implementation, followed by tool path planning. The last section is followed by finite element analysis of the cutting process which will contribute for further insights in the cutting mechanics. Next, this will be followed by an outline of experimental setup, and each variant is concluded with presentation of the experimental results and their discussion.

Chapter 3 brings the development a one-side cutting strategy for V-grooves outlined in exact same manner as the previous chapter. Here two variants of the same strategy are also presented: CCT and CCA. Finally, an alternating flank cutting strategy is presented in chapter 4 also following the same outline as chapter 2. However, here only one variant of the cutting strategy is presented that is the CCT. This is because of satisfactory understanding was obtained from previous chapters in the variation of two implementation of the same strategy.

Chapter 5 is the conclusion of the work presented in this thesis and includes a summary of the critical achievements and advancements made to the ultraprecise single point cutting strategies for V-groove manufacturing. The observations made throughout the previous chapters are significant for future work recommendations.

Chapter 2

# 2    Axial Cutting Strategy

This chapter brings the complete presentation of an axial strategy with two implementations. Building from the conventional form of V-groove fabrication, that is, from its center with a constant chip thickness, a new implementation using a constant cutting approach is explored. The exploration of both implementations includes a cutting mechanics model, finite element models, post-processing and experimental results.

## 2.1    Definition and Implementations of the Axial Cutting Strategy

The cutting strategy detailed herein relies on two principal motions: a linear travel along the Y-axis workpiece and an incremental move down along Z-axis controlled by a preset cutting depth (Figure 2.1$a$). This particular cutting strategy was termed "axial" due to the fact that the tip of the cutting tool remains always aligned with the center of the V-groove profile to be cut. More specifically, cutting motion remains predominantly contained within Y-Z plane such that $P_aP_b$ represents the length during which the tool remains in contact with the workpiece (Figure 2.1$b$). Due to the center alignment of the cutting tool, both lateral cutting edges of the tool are involved in the fabrication process. In this particular strategy, V-grooves are usually machined by means of a single point cutting tool characterized by a geometry that fully matches that of the intended V-groove structure [61].

The axial strategy presented in this chapter can be separated into two main variants: cutting with constant chip thickness (CCT) and cutting with constant cutting area (CCA). Among them, CCT remains the most used one primarily due to its facile implementation on the CNC machine. The core characteristic of CCT is represented by the constant value of its chip thickness ($\delta_{th}$ = const). The constant chip thickness translates into a constant depth of cut associated with points $P_1$, $P_2$, $P_3$ and $P_4$ (Figure 2.2). However, despite the constant depth of cut, the area and volume of material being removed increase on each cutting pass ($A_{th}$ = var). Therefore, the magnitude of the cutting force increases linearly with each pass. This linear increase is caused by the known proportionality between

cutting force and area of material removed. Nonetheless, the constantly increasing cutting forces may have a negative impact on tool life, wear and surface quality. Since the maximum amount of load to be tolerated by the tool is typically unknown a priori, the maximum cutting depth is difficult to estimate and thereby sudden tool breakages remain possible (with undesirable consequences on the length of the V-groove fabrication time). Moreover, the increasing magnitude of the cutting forces has negative consequences on the fabrication of high aspect ratio V-groove, mainly because it might lead to breakage or bending of the adjacent V-grooves that were generated in the prior longitudinal pass.
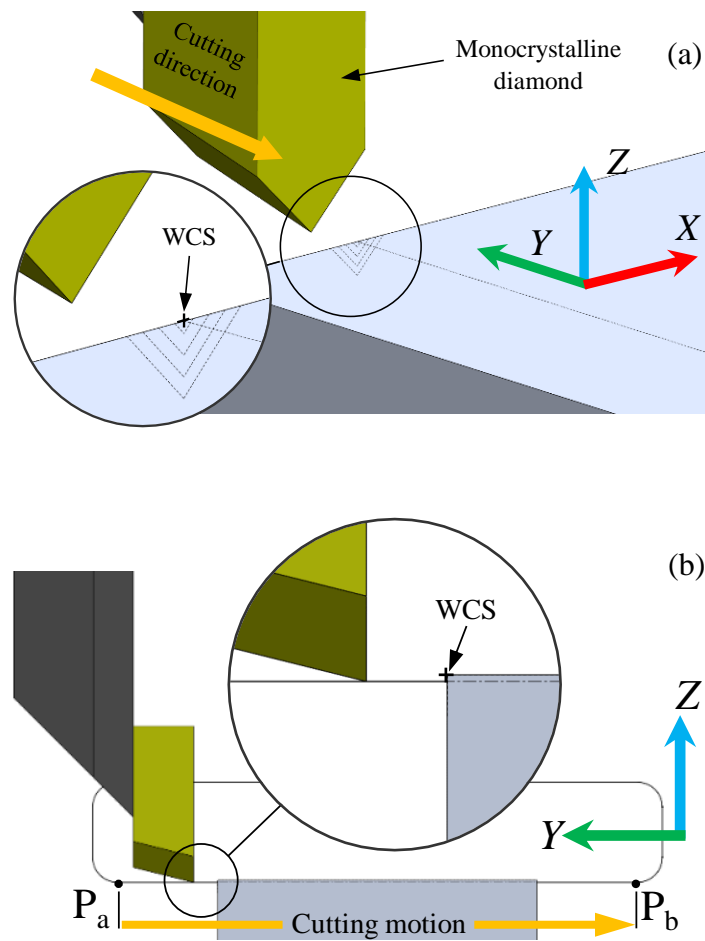


**Figure 2.1: Cutting kinematics: (a) Isometric view; (b) side view along the +X direction**

The second implementation of the axial cutting strategy relies on a constant cutting area (CCA). This approach alleviates some of the aforementioned limitations of the CCT technique. Along these lines, Lee et al [62] proposed an algorithm capable of generating V-grooves by maintaining the magnitude of the cutting forces within a preset interval [62].

Although the two approaches presented here share a number of similarities, they are also different in a number of aspects outlined further. Clearly, since CCA implies that $A_{th}$= const., this translates into a variable chip thickness ($\delta_{th}$ = var.) for each pass across the workpiece. This elevates the need for a more complex geometrical formulation of the cutting mechanics model as well as a postprocessor for the calculation of the cutting tool path trajectory in a manner that is different from CCT implementation. The direct relationship between the cutting area and cutting force implies that cutting force will remain constant in the current CCA implementation. As such, unlike CCT, cutting force thresholds can be set in advance in order to avoid tool overload/breakage.

## 2.2   Axial Cutting Strategy with Constant Chip Thickness

### 2.2.1   Mechanics of CCT Implementation

Here, the repeating tool path becomes incrementally deeper into the V-groove structure. Clearly, the distance between points $P_1$, $P_2$, $P_3$, and $P_4$ is constant and is determined by the specified chip thickness ($\delta_{th}$) (Figure 2.2). The only exception from this rule might be constituted by the first cut across the workpiece that might happen at a layer smaller than $\delta_{th}$.

According to this cutting strategy, the cut area will increase linearly proportional with the number of passes across the workpiece. It is hypothesized that the same linear trend will show on the relation between the cutting forces and the number of passes, since there is a correlation between the cutting area and the cutting force in the feed direction. Of note, "number of passes" are equivalent with depth of cut within a certain V-groove.

The small chip thickness (< 20 µm) and workpiece surface tolerances make the accurately setting of the $Z$-height relatively difficult. Because of this, the first cut at $d_1$ is

always accompanied by an inherent error. By assuming that this error is within the range of $\Delta d$ $(\Delta d = d_n - d_{n-1})$, then: $d_1 = \Delta d^{+0.0}_{-\Delta d}$.
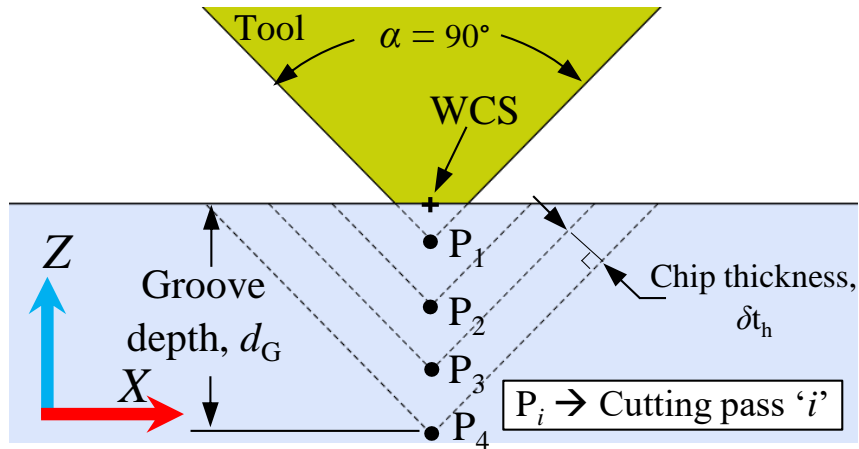


**Figure 2.2: Cutting kinematics: Front view along +Y direction**

In this strategy, $\Delta d$ is assumed as constant, therefore after the first cutting pass, the depth can be calculated as $d_n = (d_{n-1} + \Delta d)^{+0.0}_{-\Delta d}$. Based on the error in $d_1$ and by assuming that a negligible manufacturing error is associated with tool's included angle ($\alpha$), the error with respect to the cross-section area can be determined as $e_A = A^{+0.0}_{-\Delta d^2}$.
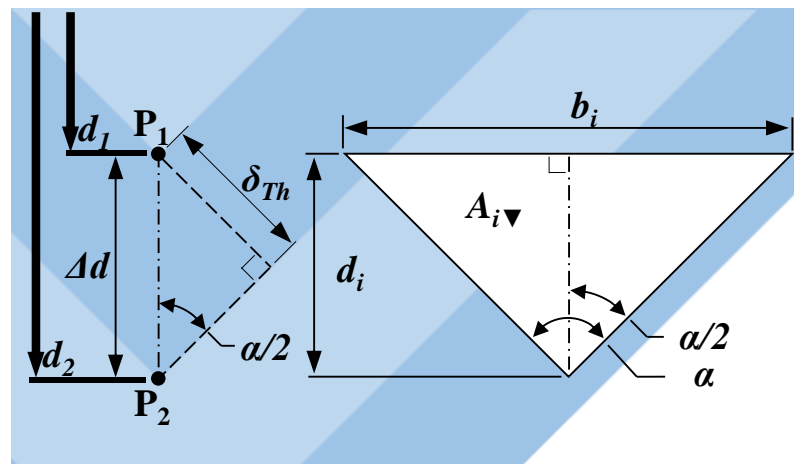


**Figure 2.3: Geometric parameters associated with the symmetrical V-groove characterized by an included angle α: a) CCT implementation**

The typical geometry of the V-groove is characterized by cutting depth ($d_i$) and groove included angle ($\alpha$) as shown in Figure 2.3. Eqs. 1-4 are formulated based on these parameters and by employing elementary trigonometric relationships in order to determine the cutting area of material being removed ($A_i$) on each pass.

$$\Delta d = \frac{\delta_{th}}{\sin\left(\dfrac{\alpha}{2}\right)} \quad \textbf{(2.1)}$$

$$b_i = 2d_i \tan\left(\frac{\alpha}{2}\right) \quad \textbf{(2.2)}$$

$$A_{i\blacktriangledown} = \frac{b_i d_i}{2} = d_i^2 \tan\left(\frac{\alpha}{2}\right) \quad \textbf{(2.3)}$$

$$A_i = A_{i\blacktriangledown} - A_{(i-1)\blacktriangledown} \quad \textbf{(2.4)}$$
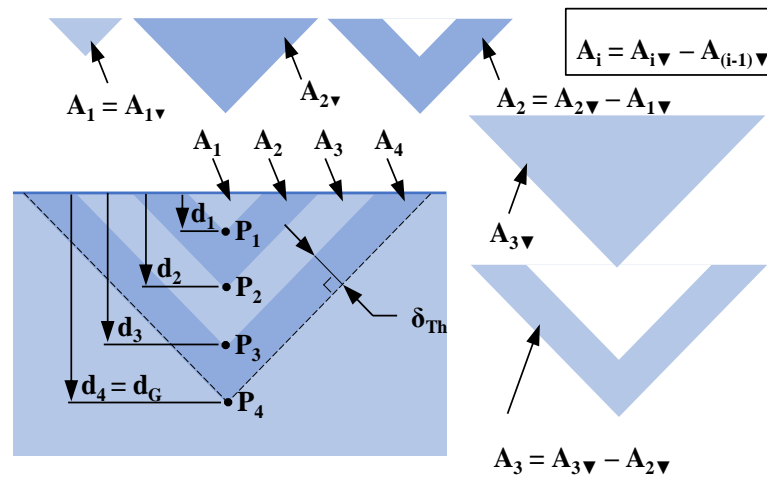


**Figure 2.4 : Dependence between cutting area and cutting pass for CCT implementation**

In the above relationships, the cutting area of the first cut is calculated by Equation 2.3 (i.e., a complete triangle in Figure 2.4). However, this calculation is no longer valid for the subsequent cuts whose outlined by the alternating blue-toned colors in Figure 2.4,

which require instead triangular area subtractions. The results of the cut area calculations were represented in a graphical form in Figure 2.5. Here, the linear trend is obvious and expected and it will be further verified against the experimental measurements of the main component of the cutting force obtained in a perpendicular-to-feed or Y-axis direction.
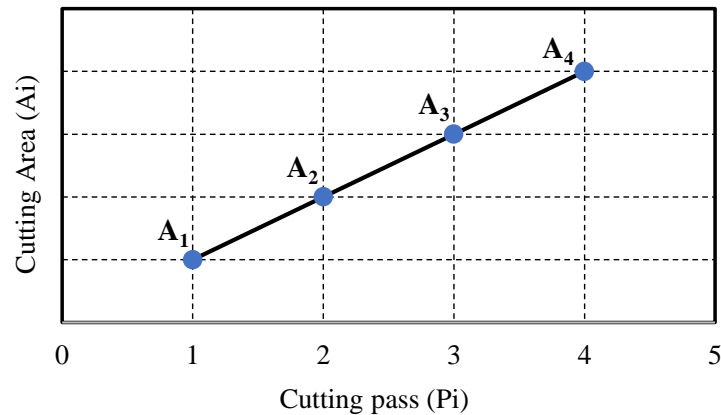


**Figure 2.5: Graphical representation of the dependence between cutting area and cutting pass: a) CCT implementation**

The increasing trend observed in the graphical representation of the dependence between cutting area and cutting pass exposes some disadvantages of the current strategy. Without knowing the tool breakage point, as the fabrication process progresses the breakage could be reached; therefore, leading to tool failure. This fact is dependent on the overall depth of the V-groove to be manufactured as well as the set chip thickness.

## 2.2.2    Toolpath Planning

MatLab was as used a postprocessor on both implementations. The analytical calculation of the cutting on both variants allowed the tracing and storing of depths of cut. These were then used for the generation of NC code used for machining, as well as for an illustration of the tool path trajectory. As mentioned before, the fundamental kinematics of the axial strategy allows for the straightforward programming of its tool path. Having established cutting parameters such as feed rate of engagement, cutting and retraction the NC program was constructed. Through the use loop structures the NC code was written

by commanding the tool tip to go at specific location with specific speed and performing basic G-code commands such as lines and arcs.

After the generation of the NC code, a tool path was plotted as shown in Figure 2.7. Even though the tool path displayed is for the CCT implementation, it does not differ much from that of the CCA since the only difference between their tool path is the constant and varying depth of cut. Since the tool path illustration is not a complete illustration of the cutting process, it was further verified with Vericut.



MatLab        VERICUT        Experiment
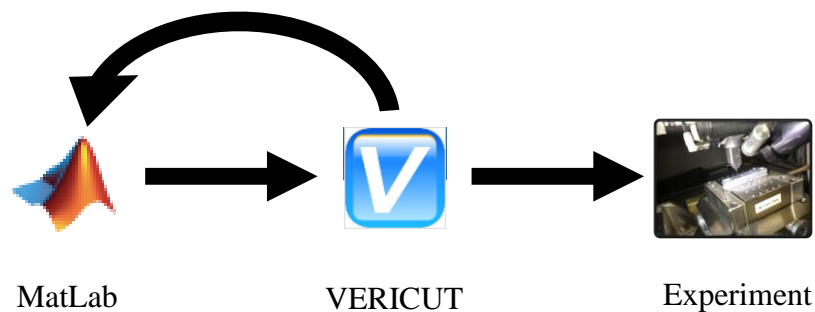
**Figure 2.6: Post processor flow**

Vericut allowed not only allowed the verification of the tool path, but it also allowed an accurate visualization of the V-groove structure created as illustrated in Figure 2.7.
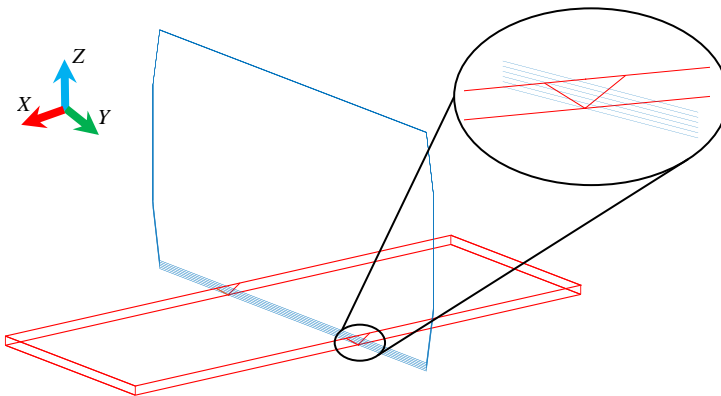


**Figure 2.7: Tool Path illustrator for CTC**

A constructed CAD model of the machining center allowed for the accurate simulation of the fabrication process of the V-groove microstructure using the NC code generated in

Matlab. The flow of the post processing phase is illustrated on Figure 2.6. After the simulation of the cutting process in Vericut (Figure 2.8), the NC code was iterated for any mistakes observed before loading it in the machining center. This guaranteed the safety of the experiment as well as the avoidance of any unexpected error in the tool trajectory which would affect the resulting microstructure created.



(a)                          (b)
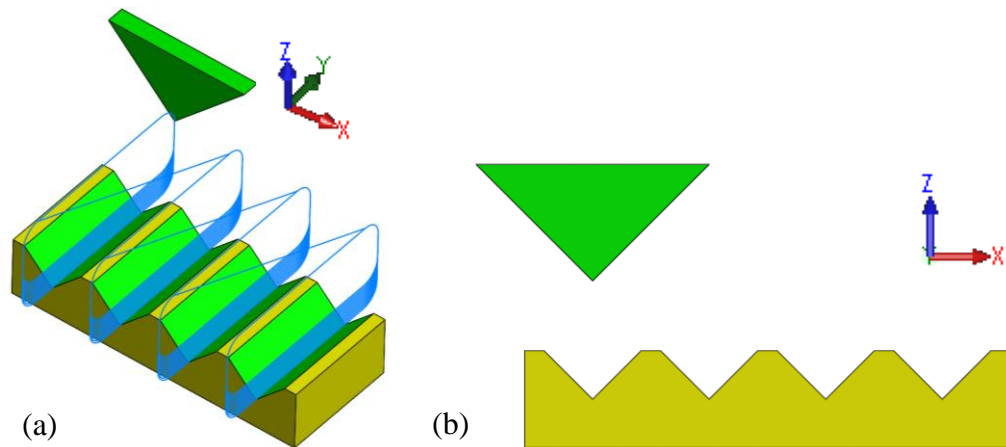
**Figure 2.8: Vericut fabricated V-grooves microstructures: (a) Isometric View with Tool path (b) Front View**

## 2.2.3    Simulation methods

Chip formation is a process during machining in which material is removed from the workpiece in the form of numerous tiny chips. Understanding chip formation regarding the chip types, shapes as well as the stress distribution would help the prediction of cutting forces and thermal behavior to avoid unexpected vibration and thermal damage [63]. To do this, the finite element models of machining processes are very popular for simulating chip formation. The reason is to minimize labor cost and save time by reducing expensive experimental tests. Moreover, the estimation of some physical phenomena such as the distribution of stress and strain under machining conditions is quite difficult to accomplish with experimental tests. Finite element method (FEM) provides a convenient method to visualize material performance under different machining conditions. Therefore, the prediction of chip types and chip shapes under

different operating conditions is one of the significant benefits provided by FEM simulations.

In metal cutting processes, often three types of chip formation occur: continuous chips, serrated chips, and discontinuous chips, which are produced as a result of the cutting deformation mechanism, operating parameters, and workpiece mechanical and thermal properties [63]. The continuous chip is often considered to be an ideal chip that generates stable cutting forces; however, it is not desired for automated machining because the continuous chips may obstruct the machining process, which may lead to unpredictable damage on the machined surface, cutting tool or machine tool. To minimize these problems, serrated chips that are easier to break and remove are preferred during automated machining [64].

Finite element analysis of chip formation can be modelled either by using Eulerian formulation or Lagrangian formulation [63]. In a Eulerian-based model, there is no need to define chip separation criterion because cutting is simulated from the steady state; however, it is required to define the initial chip shape, so it is not very realistic for investigating machining chip formation [63]. Conversely, the Lagrangian formulation can allow simulating chip formation without defining initial chip shape from incipient to the steady state. It gives more realistic results as a prediction of chip geometry and other machining-deduced phenomenal parameters, such as stress, strain, and force. However, the Lagrangian formulation needs a chip separation criterion to enable chip separation from the workpiece.

Recently, three other methods have been utilized to predict chips: material failure (damage) models based on fracture mechanics, flow stress models which take thermal softening and straining hardening into account with continuous adaptive remeshing, and Arbitrary- Lagrangian-Eulerian (ALE) adaptive meshing [63]. The first one considers the fracture mechanics concept to initiate a crack and followed by crack growth to form chips according to degradation criterion. The last two produce chips due to the plastic flow of material over the tool tip without crack formation. Moreover, the material failure model

and adaptive remeshing are used together to achieve further improvement in chip formation in some models.

Explicit FEA is generally preferred in cutting simulation because explicit analyses guarantee to converge. A progressive failure model needs a properly defined damage evolution technique. In Abaqus, which is the software used in current thesis, damage evolution can be conducted by defining either equivalent plastic displacement or fracture energy dissipation.

In metal cutting, simulation results are often considered as dependent on mesh size so called mesh sensitivity [63]. In cutting simulation at large deformation when using a progressive failure model in Abaqus, element characteristics length could be increased to reduce the mesh dependency. However, this was not done for the current simulations, a reasonable element size given the depth of cut was, rather, used. In the determination of element size, there are two main constraints that should be taken into account: (1) mesh element size should be relatively high to obtain a reasonable computation time and (2) the results should be similar to the experimental results in terms of chip morphology and cutting force generation [63]. The current FEA analysis of the axial strategy does not aim to thoroughly study the chip formation process, however, it seeks for insights on cutting mechanics of the strategy which will be further validated with experimental results.

## 2.2.3.1   The model

As previously mentioned, in this thesis all simulations were performed in Abaqus explicit FEM software. C3D8R elements, 8-node linear brick, reduced integration point with hourglass control are used in the workpiece model. Element size in cutting region (top middle section of the workpiece) is 1.5 x1.5 µm in cross-section and 2.5µm in length. Although the cutting tool is meshed, a rigid body constraint is applied to the cutting tool in the simulations. Figure 2.10 illustrates the meshed tool with a non-uniform mesh, this is due the fact that the cutting edges of the tool were seeded to refine the mesh at the cutting region. Cutting tool speed of 500 mm/min is used for all simulations, as this is the speed used for experiments. Workpiece boundary conditions are shown in Figure 2.9.

The penalty contact method with a constant friction coefficient ($\mu = 0.30$) is applied between the tool and workpiece. The choice of the friction coefficient relied on available literature [65]. The contact of was defined by the setting the defined pairs of the tool and workpiece to interact with each other. Here, it was important to set the interaction of the cutting layer with itself to prevent penetration during material deformation. The simulation is not modelled considering the adiabatic heating effect on since heating effects are not critical for the cutting techniques used here. Moreover, it would significantly increase the simulation time. Element deletion technique is used to allow element separation to form a chip.
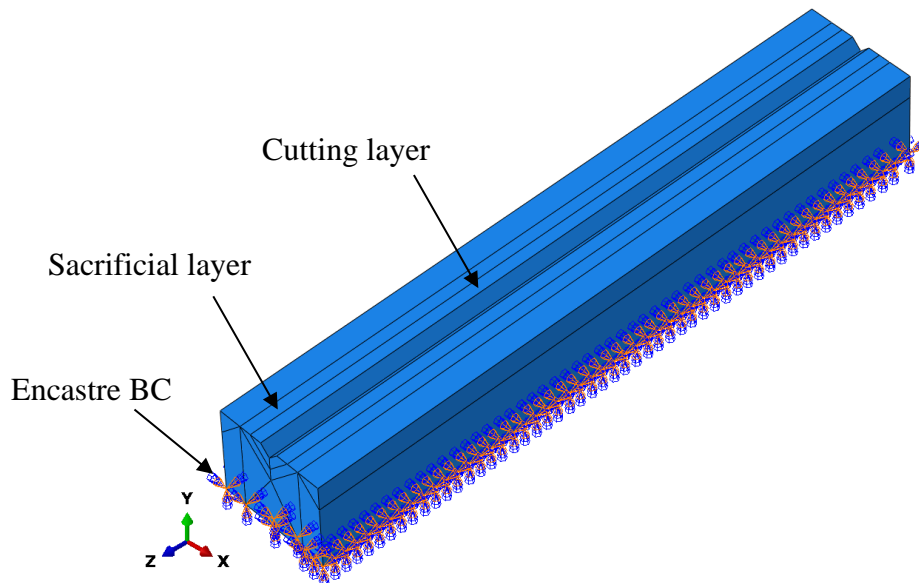


**Figure 2.9: FEA Workpiece with BC, sacrificial and cutting layer**

Furthermore, a sacrificial layer is used to allow chip separation (Figure 2.9), this will prevent the simulation from terminating due to excessively distorted elements caused by inconvenient damage parameters. Damage criterion and element deletion is applied to entire workpiece elements. The analysis was performed using finite element method with Langrangian approach and element erosion.

In addition, the model was created with the following parameters: box- shaped workpiece with 500 x 250 x 2250 µm. The small dimensions of the cross-section of the workpiece rely on the fact that only the first three passes of the strategy were simulated. Moreover,

with an exception to the first pass across the workpiece, all passes had the previous groove already cut on the workpiece. This was done to avoid complications with remeshing techniques. In the analysis, the cutting tool is assumed to be a rigid body with monocrystalline diamond parameters: density 3520 kg/m$^3$ elastic modulus 1050 GPa, Poisson's ratio 0.1. Geometric variables of the tool are as follows: rake angle $\gamma = 0°$, clearance angle $\beta= 10°$ and an included angle $\alpha=90°$. The material on the workpiece is selected as aluminum 6061-T6, which has the following properties: density 2700 kg/m$^3$, Young's modulus E=70 GPa, fracture strain 0.5, yield stress 260 MPa.
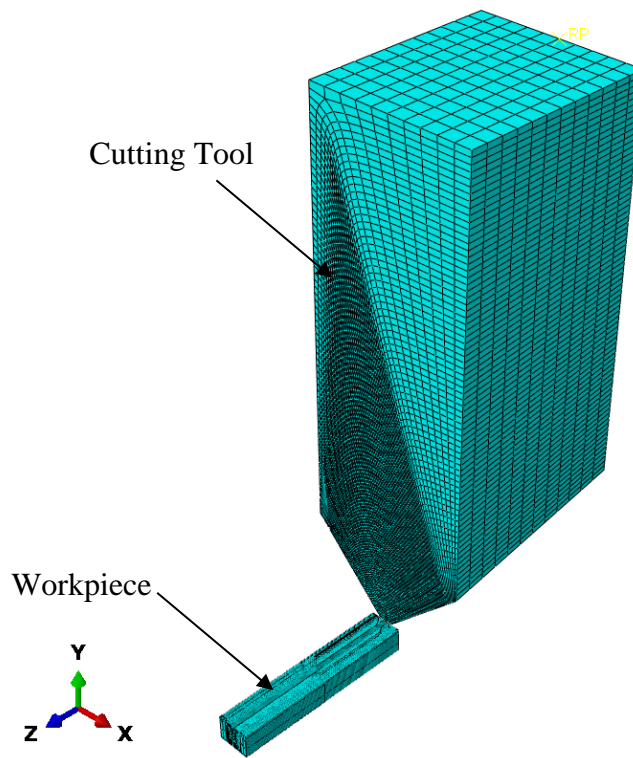


**Figure 2.10: FEA model assembled**

Flow stress modeling of workpiece material is very important to achieve satisfactory results from metal cutting simulation. In the analysis, 6061-T6 is selected as workpiece material since it is the one used for the experiments. Johnson-Cook constitutive models are used in the current analysis. The parameters for isotropic and kinematic hardening are as follows: elastic modulus 70 GPa, Poisson's ratio 0.33, yield stress 260 MPa. The parameters of Johnson-Cook obtained by experiment are as follows: A=324.1 MPa,

B=113.8 MPa, n=0.42, C=0.002, m=1.34, reference strain rate = 1 [66]. The failure model parameters for Johnson-Cook model are as follows: D1=-0.77, D2=1.45, D3=0.47, D4= 0, D5=1.6 [66]. As for the failure criterion, a displacement damage evolution criterion was used with a displacement at failure of 1µm.

## 2.2.3.2    Results and analysis

Figure 2.11 illustrate the results of the Von Mises stress distribution on the workpiece for passes 1 and 2. Simulating multiple passes helped not only the assessment of the accuracy of the model, but also allowed the observation of the chip formation and cutting force trend in multiple passes, the first passes across the workpiece allowed for this observation.
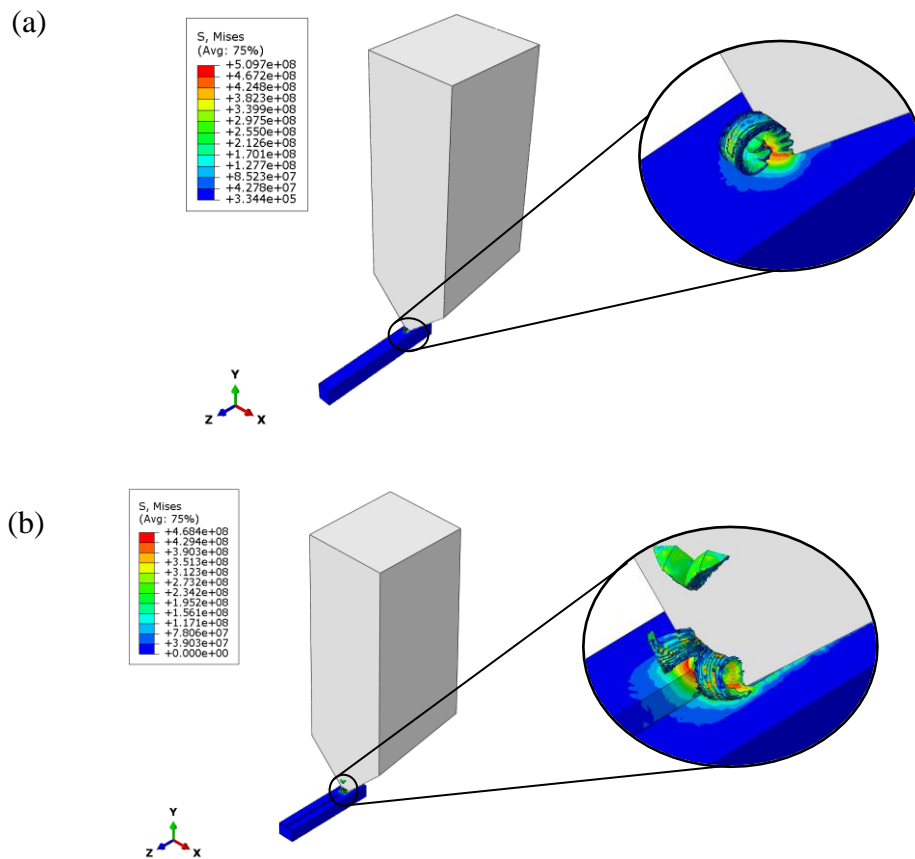


**Figure 2.11: Von-Mises stress plot results: (a) Pass 01 and (b) Pass 02**

The simulations were conducted at constant chip thickens of 15µm. As one can see, the model elements have essential hourglass distortion that requires an additional investigation, this is clearly seen on the results of the second pass across the workpiece.

A continuous chip forms as results of the first pass across the workpiece (Figure 2.12). This continuous chip from the first pass was further validated against the experimental results. The chip morphology is in good agreement with common machining theories relating tools with zero rake face and continuous chips. Negative rake face tools cause higher compression results in tearing stress increasing in the primary shear region, which in turn promotes segmentation, then eventually separation of each segment. Since material strength in the primary shear region decreased with increasing straining, ultimate fracture occurs when the predefined damage evolution criterion is satisfied.
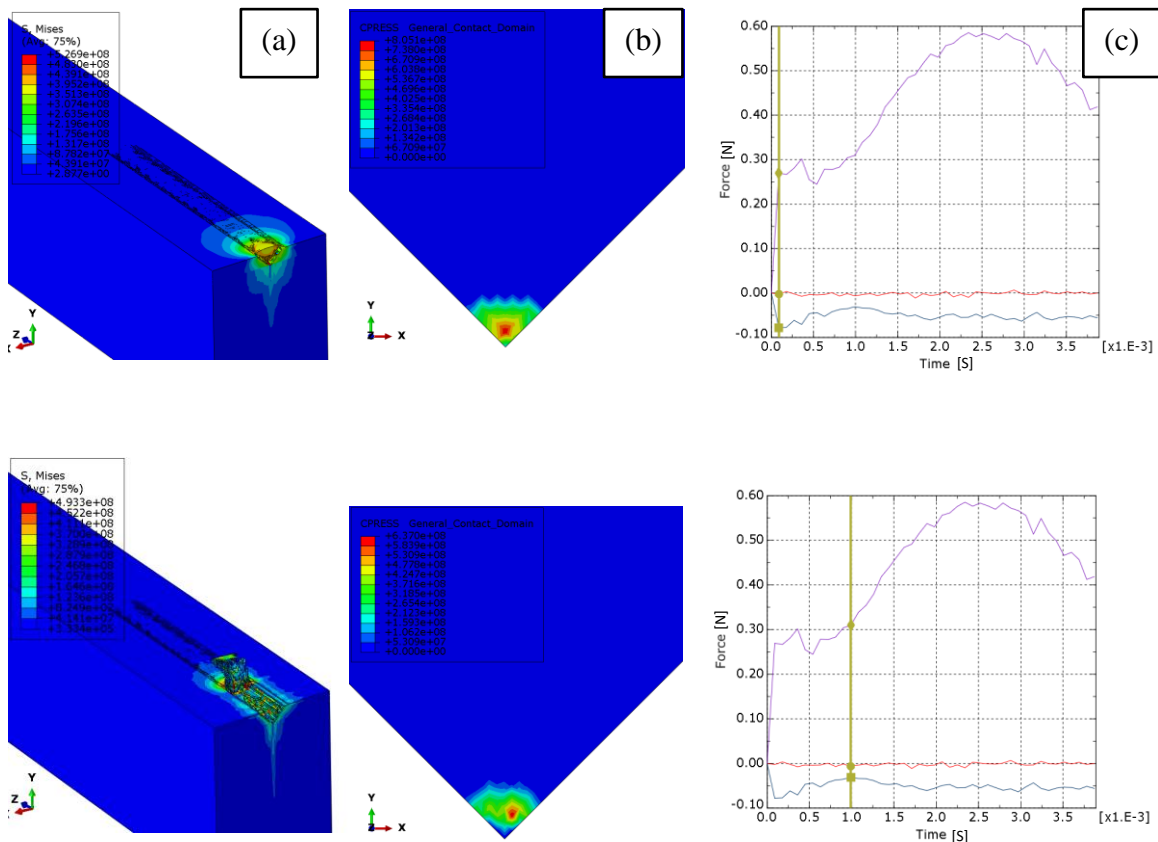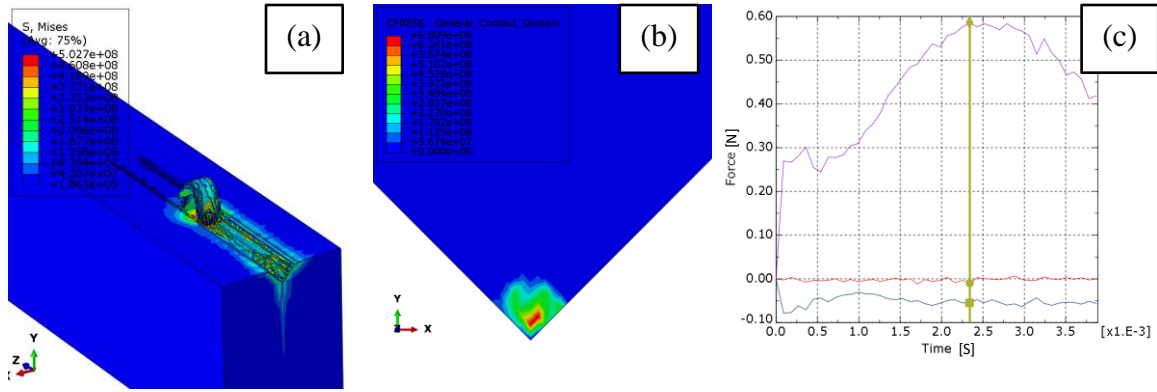
**Figure 2.12: Snapshots of FEA results for pass 01 of CCT: (a) workpiece; (b) Cutting tool: (c) Cutting forces**

The cutting force redistribution on the cutting tool is important aspect of the simulation. This redistribution is shown by the change of the contact stress pattern displayed on the cutting tool. This redistribution of the cutting force manifested on the force plots and fluctuations. The cutting force plot shown in Figure 2.12 illustrates a rise in the force magnitude due to the same redistribution. The cutting area pushed by the tool just when it touches the workpiece is less compared to moments after the chip starts to roll.
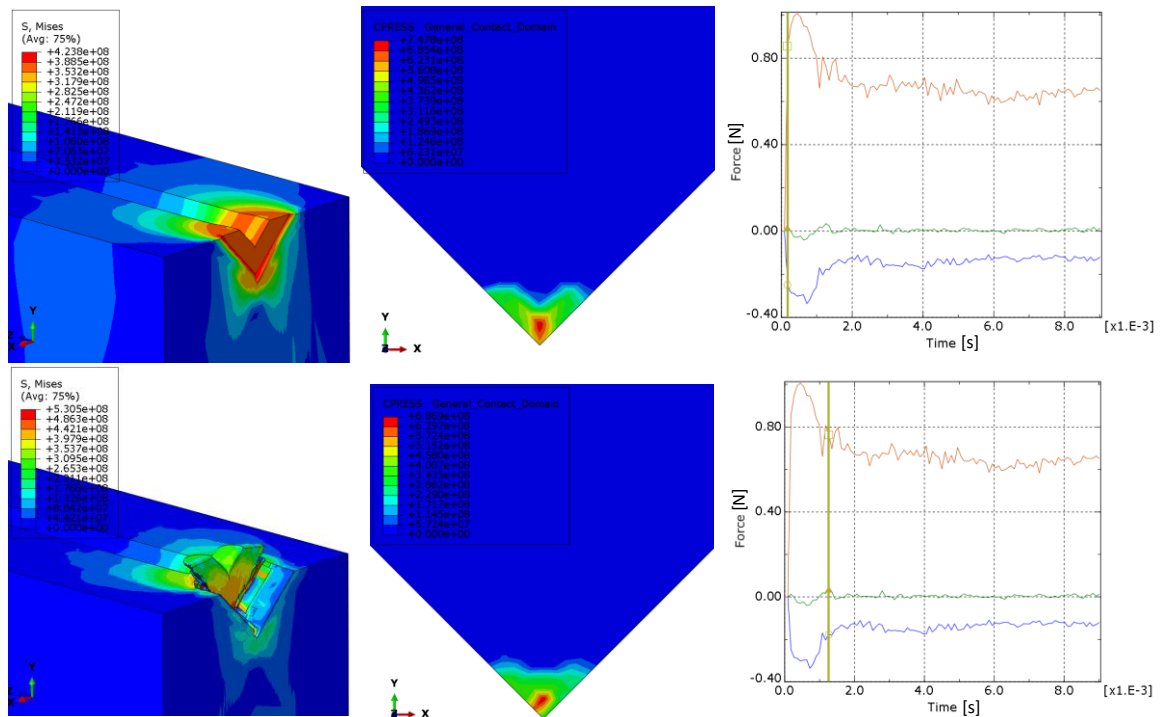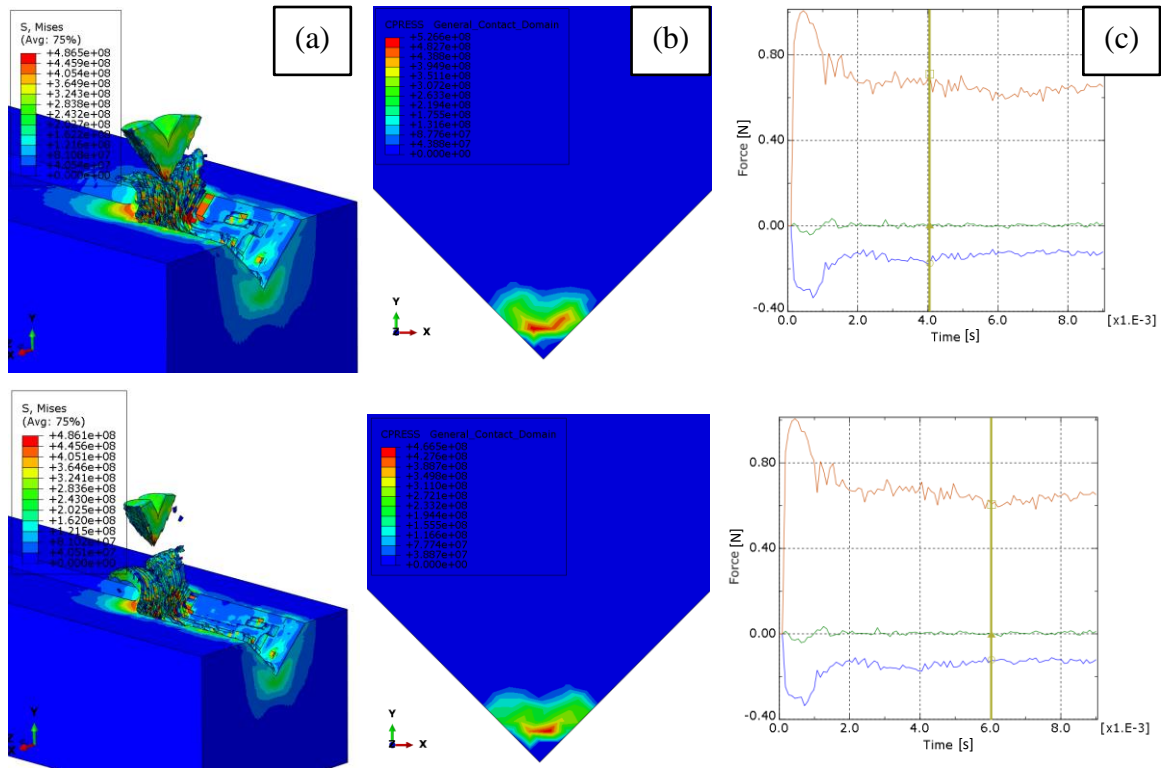
**Figure 2.13: Snapshots of FEA results for pass 02 of CCT: (a) workpiece; (b) Cutting tool: (c) Cutting forces**

The same chip morphology is observed on the second pass (Figure 2.13). However, it is observed that the initially single chip starts to separate between the two faces of the V-groove. Experimental results revealed that this is not the case; therefore, further investigation is required for the model developed. The cutting force on the second pass, however, shows a transient response. This is due to fact it was simulated for a longer period at which the cutting force seems to stabilize, that it becomes almost constant as the chip is removed from the workpiece. The cutting forces illustrated on both passes (Figure 2.12 and Figure 2.13) show very satisfactory agreement with the experimental results later presented here.

## 2.2.4    Experimental Setup

Figure 2.14 depicts a detailed representation of the experimental setup, having its core element represented by the Kugler Microgantry Nano 5x micromachining center. To capture the three principal axis components of the cutting force, a three-axis Kistler

9256C2 dynamometer was mounted atop of the machine C-axis and underneath the workpiece.
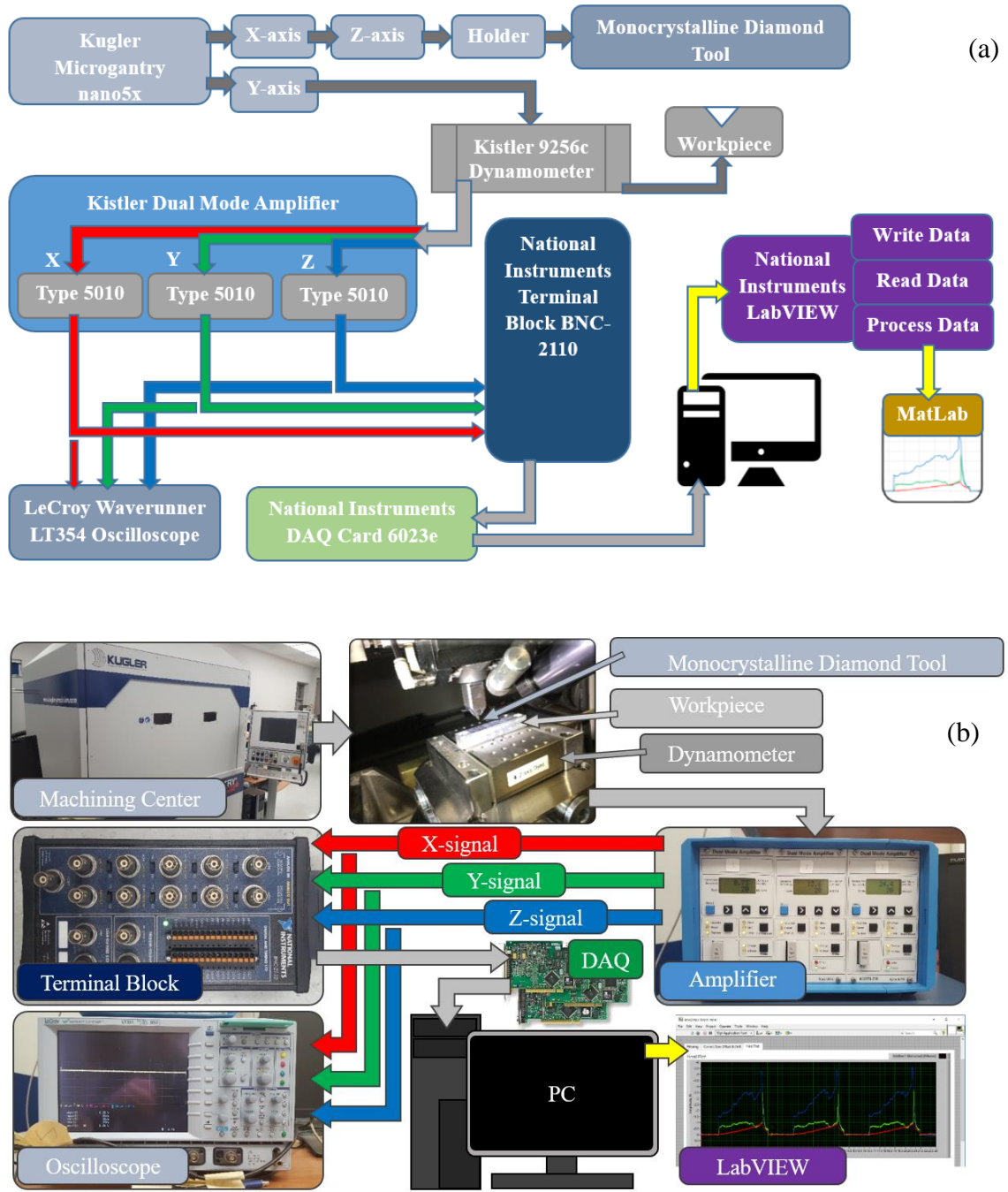


Figure 2.14: Experimental setup representations: a) block diagram; b) photographic

The signal captured by the dynamometer was amplified and further split into X, Y, and Z components. To allow signal monitoring, the amplifier was connected to a LeCroy Wayerunner LT354 oscilloscope through a National Instruments terminal block. Finally, a National Instruments 6023e data acquisition card was also connected to the terminal block to allow data storage for subsequent processing.

The tool used in this study consists of a monocrystalline diamond and its carbide holder (Figure 2.15). The diamond insert has a set rake angle of 0°, whereas the clearance angle was prescribed at 10° on both symmetrical cutting facets.
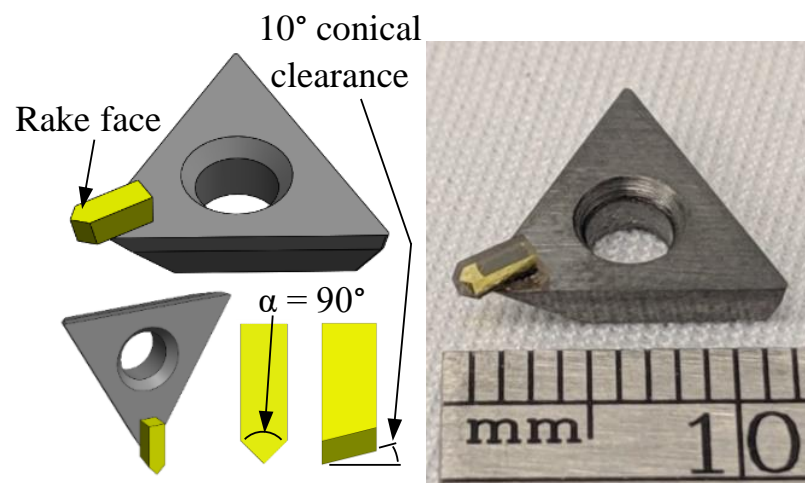


**Figure 2.15: V-shaped monocrystalline diamond single point cutting tool**

Moreover, the diamond insert was ground and lapped to achieve a symmetrical 0° included angle. This angular value has a direct effect in the geometry if the generated V-grooves. On both implementations, it allowed the fabrication of symmetrical V-groove microstructures.

Both implementations of the axial cutting strategy were tested on an aluminum 6061 block. The results and analysis follow in the next sections.

## 2.2.5    Experimental Results and Analysis

Table 2.1 summarizes the experimental parameters used during the experiments involving the implementation with CTC. Following data acquisition procedure, advanced

signal processing was applied to the recorded data using Matlab sofware. During the processing of the data, a low pass filter was applied on the converted LabView-formatted data to filter the high-frequency noise.

**Table 2.1. Summary of experimental conditions for CCT**

| Feed rate (mm/min) | 500 |
|---|---|
| Chip thickness (μm) | 5, 10, 15 |
| Coolant | Isoparaffin mist |
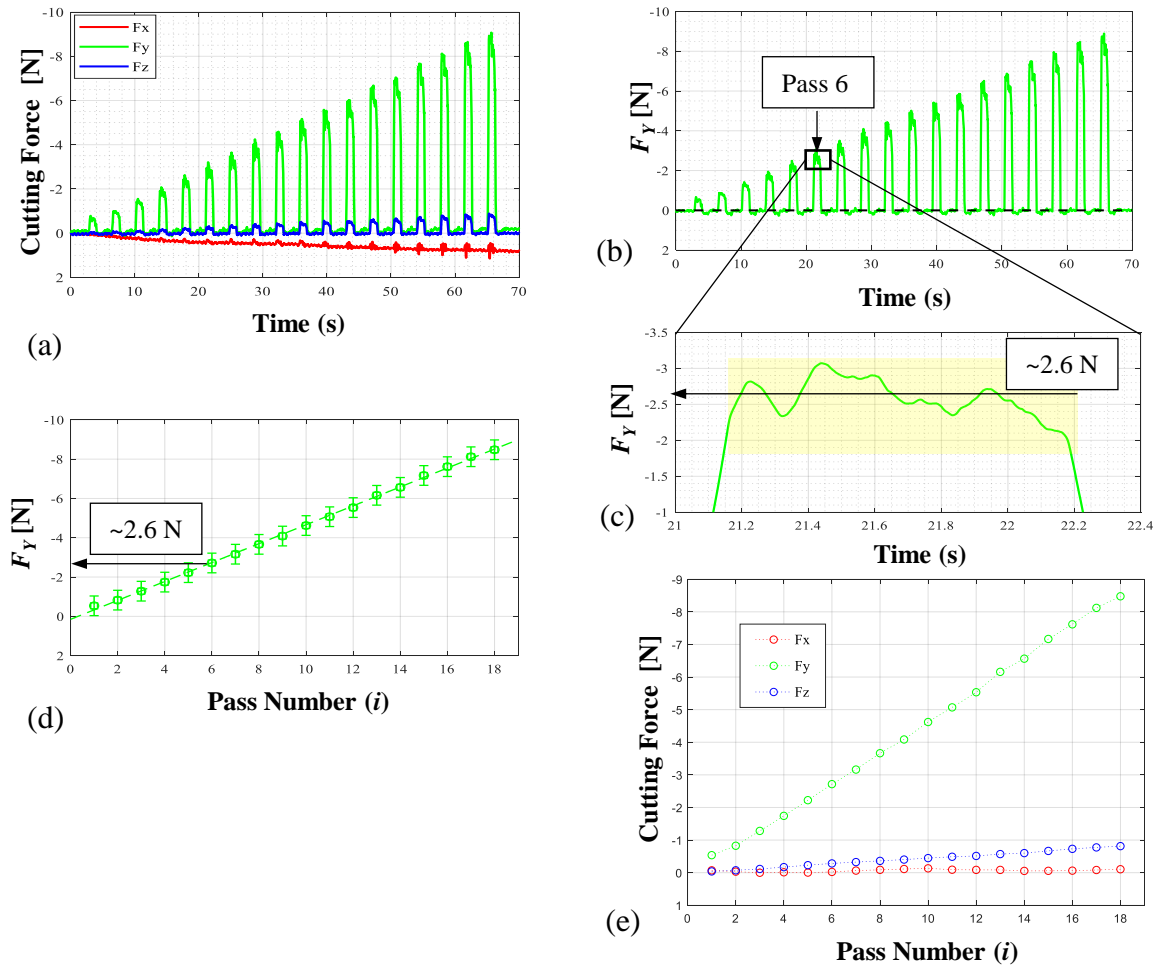


**Figure 2.16: Cutting force measurements for CCT: (a) raw data; (b) $F_Y$ with measurement drift corrected; (c) sample of average $F_Y$ calculation; (d) average $F_Y$ variation during microgroove cutting; (e) average cutting force components.**

For this purpose, a moving average filter with a sampling rate of 2 kHz – essentially matching the sampling rate of the NI DAQ system – and a window of 200 data points was used. The filtering stage, allowed the extration of the quasi-static component of the cutting force in all directions (X,Y, and Z). Figure 2.16(a) shows the raw-filtered data for a chip thickness of 10μm. Each pulse of the cutting force signal is associated with a new pass across the workpiece. The analysis presented herein will remain focused on $F_Y$ since it represents the main component of the cutting force on the feed direction.

During the second stage of the processing of the data, the measuremnt system drift was corrected. This was done by using a second second order linear regression to determine the mean of the data to be broght down to zero. This data corresponds to noncontact situations between tool and workpiece. Once the slope of the drifting mean was determined, the appriate values were subtracted and the drift was eliminated for all three components of the the cutting force (Figure 2.16 (b)).

A more careful analysis of the data presented in Figure 2.16 reveled $F_Y$ signal fluctuations on each indivuidal pulse. This is a consequence of the intial impact between the tool and the workpiece which is translated into a damped vibratory response on the signal. To process these variables pulses, the peak $F_Y$ values were averaged for each V-groove cut/pulse across the workpiece and then plotted against passes (Figure 2.16d). The error bars represent the standard deviation of the raw but drift-corrected acquired data.

A graphical representaion of all cutting force components is illustraded on Figure 2.16e for the entire duration of V-groove fabrication. According to these results, $F_X$ remains consistent with the overall tool kinematics, which does not allow moveemnt outside of the Y-Z plane, nearing zero. $F_Z$, however, has non zero values most likely due to the upward force exerted by the chip on the tool. According to prior predictions, $F_Y$ component follows a linear dependence with respect to the number of passes. Moreover, a strict dependence to chip thickness also exists (see Figure 2.17)
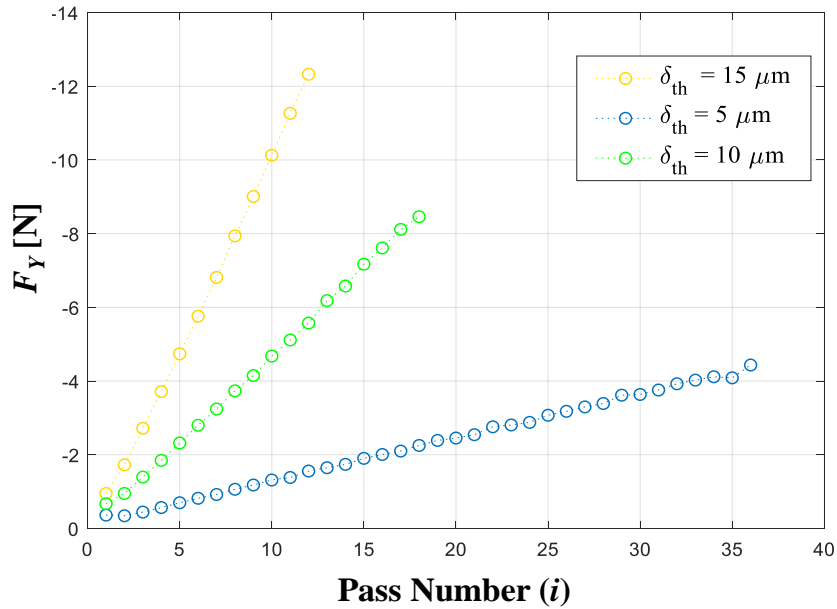
**Figure 2.17: Correlation between the main component of the cutting force and chip thickness: a) CCT implementation;**

The correlation between the main components of the cutting force and chip thickness showed in Figure 2.17 reveal a tradeoff between the machining time and force magnitudes. Intuitively, smaller constant chip thicknesses make the fabrication process take a longer time, however with small force magnitudes. Since higher force magnitudes maybe directly related to tool wear, smaller thickness maybe more desirable than higher ones.

In addition to cutting force results, the quality of the V-groove surface was assessed by means of optical profilometer. For this purpose, the workpiece was tilted at an angle of 45° to enable a horizontal positioning of the V-groove facets. This is an essential prerequisite of an accurate surface quality measurement. A representative illustration of V-groove topography is presented in Figure 2.18.
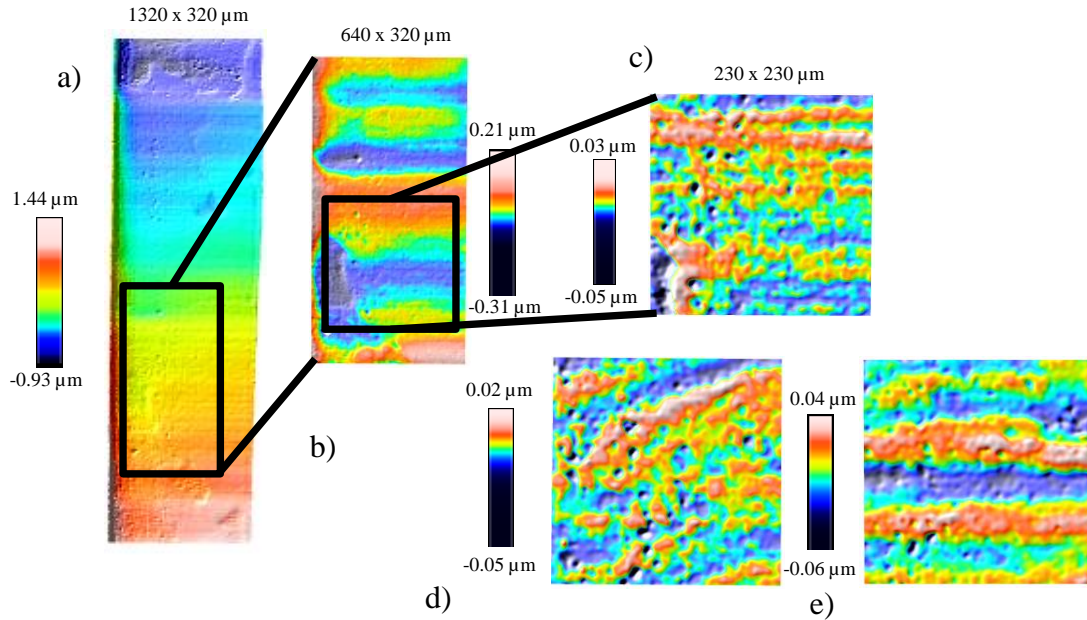
**Figure 2.18: Surface quality results for CTC: (a) raw data; (b) data with planar tilt removed; V-groove surface topography for: (c) 5 µm chip thickness; (d) 10 µm chip thickness; (e) 15 µm chip thickness.**

The spatial inclination that is present and visible in the raw data (Figure 2.18a) was corrected in such a way that its mean was positioned on zero (Figure 2.18b). Next, a filter with a cutoff wavelength of 80 µm (ISO 16610-61) was applied to remove surface waviness and retain just roughness. The final postprocessed topographic data is presented in Figure 2.18 d-e for various chip thickness values.

**Table 2.2: Summary of surface quality measurements for CCT**

| Chip thickness (µm) | $S_a$ (nm) |
|---|---|
| 5 | 5.4128 |
| 10 | 5.7310 |
| 15 | 13.895 |

Table 2 presents a summary of the results of the areal average surface roughness measurements (Sa). These results imply that ultraprecise structure with the optical surface quality (< 10 nm) is attained by means of the proposed single point cutting procedure. It is important to note that the effect of the cutting strategy on the surface quality it is somewhat indirect. The cutting force generated by the strategy is the one that

significantly affects the surface quality, then it turns the control of the surface quality by the use of the strategy and indirect control.

## 2.3 Axial Cutting Strategy with Constant Cutting Area

### 2.3.1 Mechanics of CCT Implementation

According to the developed constant cutting area strategy, the distance between points $P_1$, $P_2$, $P_3 \ldots P_N$ (Figure 2.19) and the associated chip thickness ($\delta_i$) is not constant since it is governed by a constant cutting area. By starting with a predefined minimal final chip thickness ($\delta_{min} = \delta_N$), the post-processor generates all intermediate passes from last to first (i.e., $P_N$ to $P_1$), which yields the gradually increasing chip thickness ($\delta_i$) from first to last cut (i.e., $\delta_1$ to $\delta_N$) (Figure 2.19).
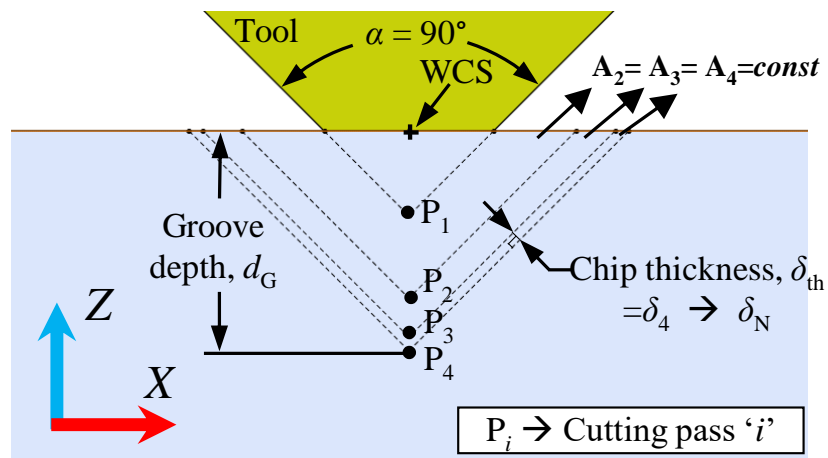


**Figure 2.19: Axial cutting of V-grooves with constant chip thickness**

The very first pass $P_1$ typically has a cutting area less than or equal to the specified constant area, the main obstacle being the accurate setting o the Z-height of the tool with respect to the WCS. This is also influenced by the small depth-of-cut ($< 20\ \mu m$) and workpieces tolerances. The analytical formulation of the proposed strategy starts by calculating initially the area to be maintained constant based on the desired final chip thickness ($\delta_N$) and final geometry of the V-groove. Subsequently, the position of the cutting tip which corresponds to the depth of cut for each pass is calculated by means of the selected constant cutting area in reverse sequential order.

Figure 2.20 illustrates the typical geometry of the V-groove. Eqs. 1-7 are formulated based on the cutting depth and V-groove included angle, and by employing elementary trigonometric relationship it is possible to determine the constant cutting area of material being removed ($A_i$).
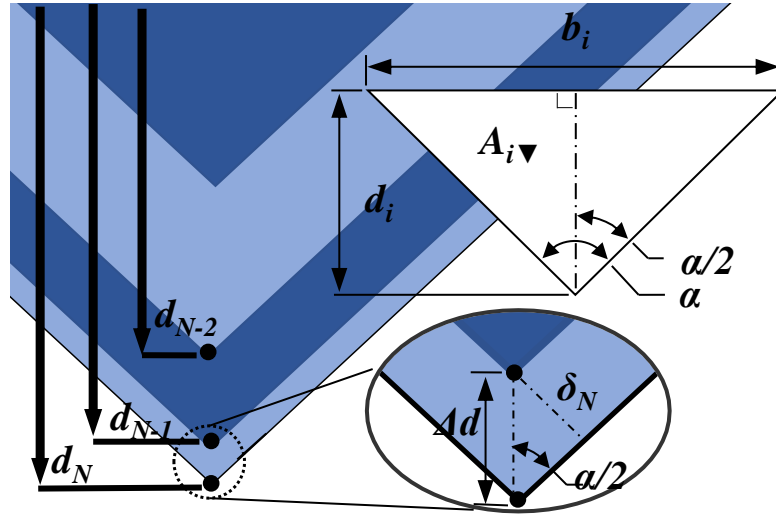


**Figure 2.20: Geometric parameters associated with the symmetrical V-groove characterized by an included angle α of the CCA implementation**

The analytical calculations of the constant cutting area and variable depth-of-cut have been initialized from the bottom of the groove in order to minimize their complexity. As mentioned before, the constant cutting area is predetermined by the thickness value of the last cutting pass ($\delta_N$). Following this calculation, the present thickness of the last pass permits the determination of the last change in depth, $\Delta d_N$, from the final depth of the groove ($d_{Groove} = d_N$), as indicted in Equations 2.5-2.6.

$$\Delta d_i = \delta_i / \sin(\alpha / 2) \quad \textbf{(2.5)}$$

$$d_i = d_{i+1} - \Delta d_{i+1} \quad i = 1,2,3\ldots(N\text{-}1) \ \textbf{(2.6)}$$

In addition, the base of the full triangle depth calculated as in Equation 3 can be combined with Equation 1 to calculate the area of a full depth triangle as shown in equation 4. After that, the constant cutting area is obtained by subtracting the full depth

triangle area of the current profile ($A_{\blacktriangledown}$) from the area associated with the previous depth of cut ($A_{\blacktriangledown(N-1)}$) and similar iterative formulation can be used after that.

$$b_i = 2d_i \tan(\alpha/2) \quad \textbf{(2.7)}$$

$$A_{\blacktriangledown i} = b_i d_i / 2 = d_i^2 \tan(\alpha/2) \quad \textbf{(2.8)}$$

$$A_{const} = A_i = A_{\blacktriangledown i} - A_{\blacktriangledown(i-1)}, \, i = 2, 3 \ldots N \quad \textbf{(2.9)}$$

$$A_{\blacktriangledown(i-1)} = A_{\blacktriangledown i} - A_{const} \quad \textbf{(2.10)}$$

The formulas above will ensure that the cut performed at $d_{(N-1)}$ will be characterized by the same $A_{const}$. The upcoming depth of cut $d_{(N-2)}$ is determined by:

$$d_i = \sqrt{A_{\blacktriangledown i} \tan(\alpha/2)} \quad \textbf{(2.11)}$$
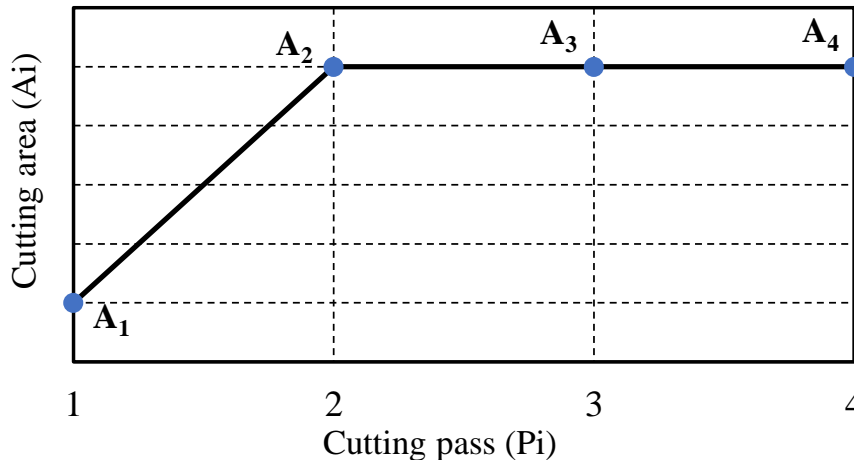


**Figure 2.21: Graphical representation of the dependence between cutting area and cutting pass for the CCA implementation**

The analytical dependence of the cutting area on cutting pass/depth is shown in Figure 2.21. From the calculation above it can be seen how the very first pass will be characterized by a cutting area less than $A_{const}$.

The graphical representation of the dependence between cutting area and cutting pass illustrate the constant trend with an exception of the first cut, which is affected the setting of the tool Z-height. Due to the known proportionality between the cutting area and the cutting force, it is expected that the cutting force will exhibit the same trend as the one sown in  Figure 2.21.

## 2.3.2    Simulation methods

Figure 2.22 and Figure 2.23 illustrate the simulation results for the CCA implementation, modeled with the same conditions as the CCT implementation. The last chip thickness was set as 5µm for all passes. The same chip morphology as the CCT was observed with the chip separation of both faces. Even though this requires further investigation, the success of the simulation consists on the magnitude and trend of the cutting force.
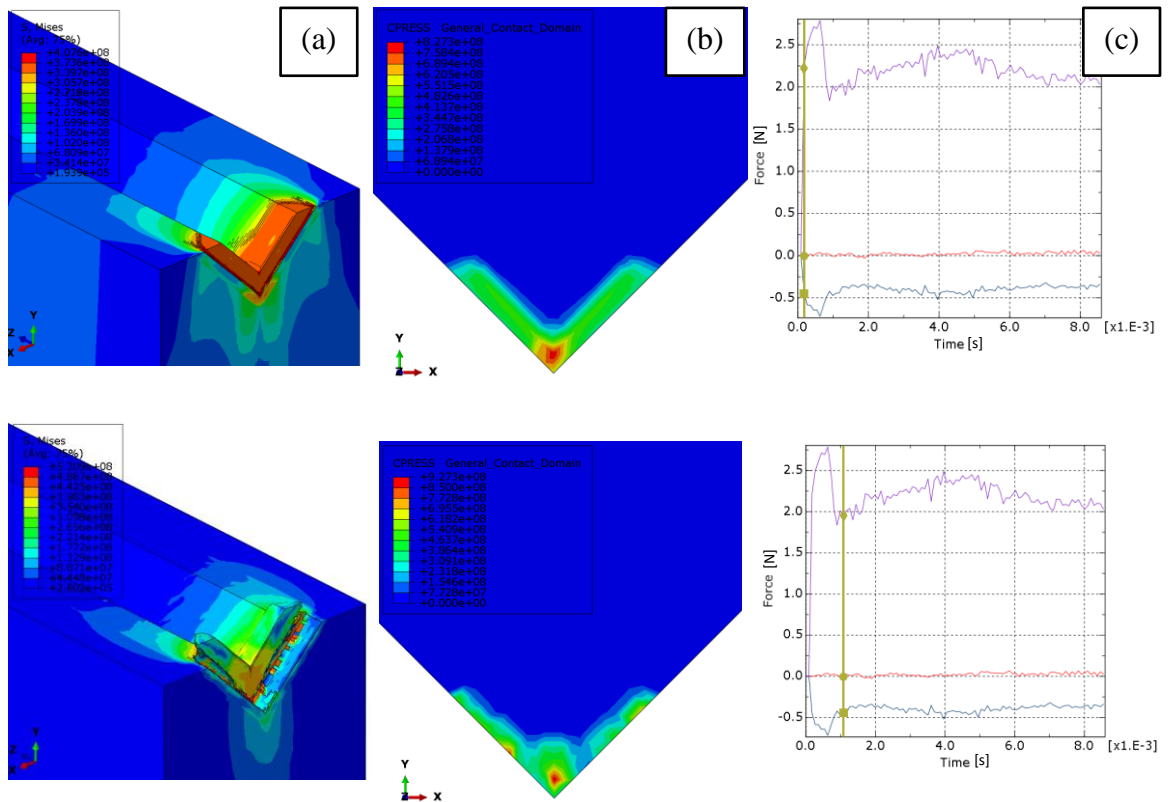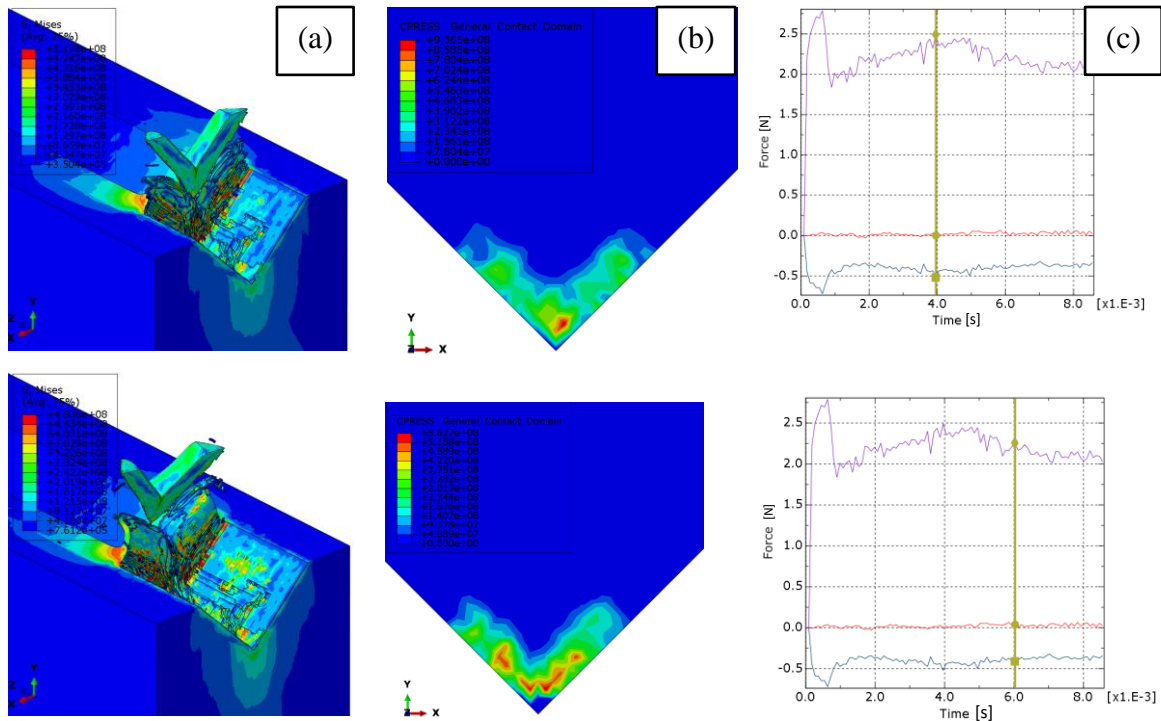
**Figure 2.22: Snapshots of FEA results for pass 02 of CCA: (a) workpiece; (b) Cutting tool: (c) Cutting forces**

Passes 2 and 3 reveal a constant trend of the cutting force and with a magnitude that is within a good agreement with the experimental results. One the cutting tool is also noticeable the redistribution of the cutting forces as it progresses across the workpiece. This reveals as the fluctuations on the cutting force plots. Interestingly, fluctuations are also observed on the experimental results. Although this needs to be further investigated, it may be hypothesized that the same cause underlines both cases. In addition, the force results on both passes revealed the cutting force in the feed direction ($F_Y$)represented the highest magnitude displayed on the force plot. The small magnitude of the force in the Z-direction is explained by the chip exerting an upward force in the cutting tool. As mentioned before, this will be furthered validated with the experimental results.
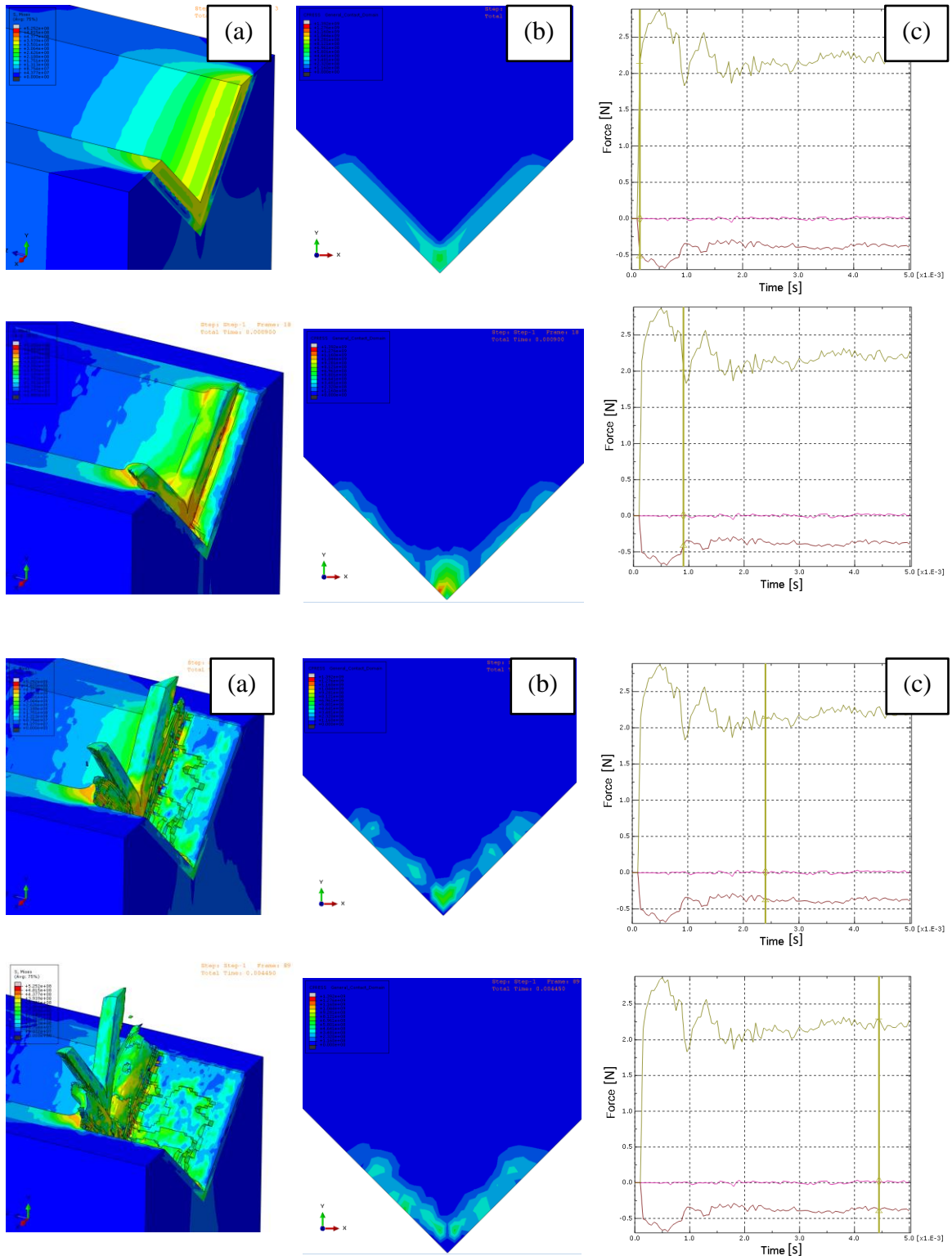
**Figure 2.23: Snapshots of FEA results for pass 03 of CCA: (a) workpiece; (b) Cutting tool: (c) Cutting forces**

## 2.3.3    Experimental Results and Analysis

Table 3 summarizes the process parameters used in cutting experiments.

**Table 2.3: Summary of experimental conditions for CCA**

| Feed rate (mm/min) | 500 |
|---|---|
| Final chip thickness (µm) | 5, 10, 15 |
| Coolant | Isoparaffin mist |

A similar approach to the one used in the previous chapter was used here to process the data stored during the experiments.
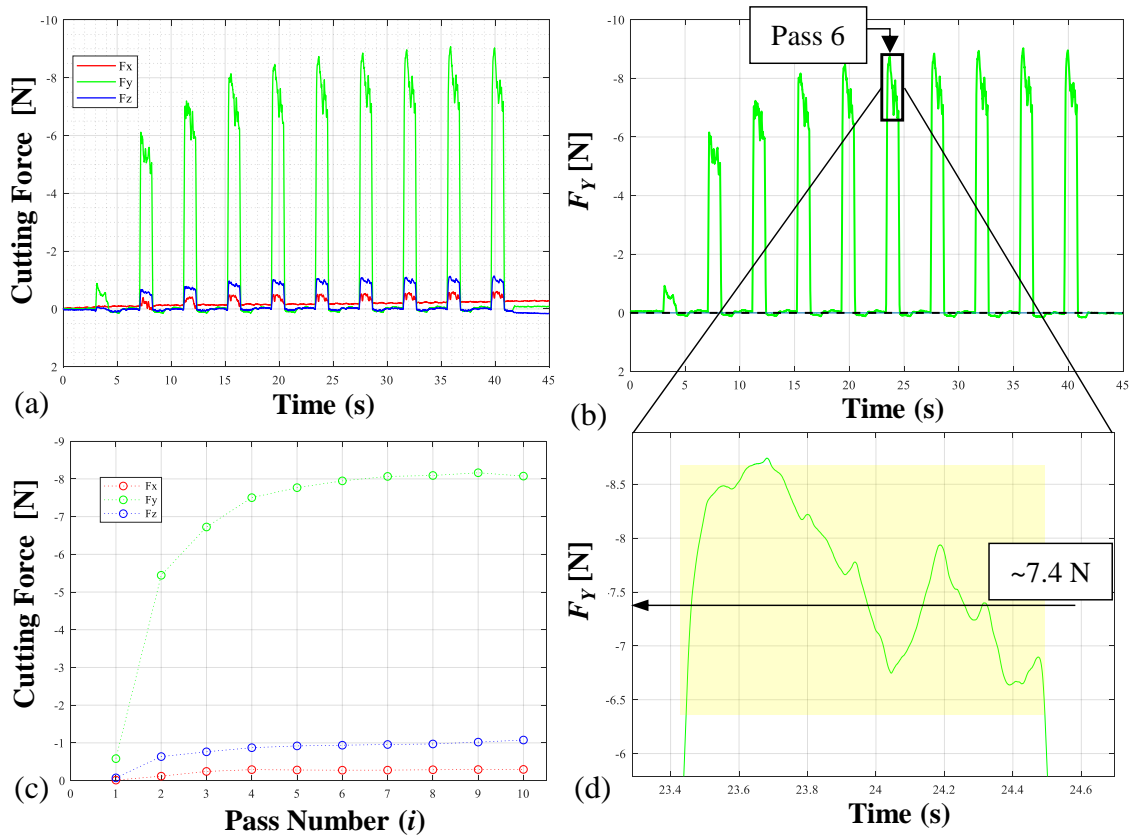


**Figure 2.24: Cutting force analysis for CCA: (a) raw data; (b) drift-corrected $F_Y$ component; (c) typical $F_Y$ fluctuation and $F_Y$ average value; (d) average cutting force values.**

A moving average low pass filter with a sampling rate of 2 kHz – essentially matching the sampling rate of the NI DAQ system – and a window of 200 data points was used, as well as the same technique to correct the drift of the data. The cutting cycle displayed in Figure 2.24 include a final cutting pass characterized by a chip thickness of 10 µm.

Having finished the processing of the data, the average values for each component of the cutting force during the engage/stable V-groove cutting are presented in Figure 2.24. As the previous variant of the axial strategy, $F_X$ was measured at negligible values and $F_Z$ also displays the effect of the upward friction between the tool and the chips as they are removed.

As anticipated, the largest contributor to the axial cutting force is $F_Y$ and its magnitude remains quasi-constant throughout the entire V-groove fabrication process. However, $F_Y$ seems to slowly increase in the first couple of cutting passes until it stabilizes. This increasing trend of $F_Y$ in the first couple of passes might imply that V-groove cutting force in not only dependent on the area of material removed (according to the "classical" material removal rate theory), but also on the chip thickness/cutting depth which on the current case slowly decreases until the fabrication of the groove is finished. However, it can safely be assumed that the area of material removed remains the most important contributor on the axial force value. The relative influence of the two variables on $F_Y$ can be represented analytically as:

$$F_Y = C_A A_i + C_\delta \delta_i \ , \ C_A >> C_\delta \quad \textbf{(2.12)}$$

where $C_A$ and $C_\delta$ are proportionality coefficients. While at this point it cannot be provided a clear reason behind the influence of chip thickness on axial force, it could be contemplated here that cutting depth-related differences in shear plane formation and dynamics of the cutting chip formation might play a role. Figure 2.25 shows the correlation between the main components of the cutting force and chip thickness for the CCA implementation. From this figure, the same conclusions could be taken as in the correlation for the CCT implementation. The same tradeoff between force magnitude and machining time is revealed. In addition to this, is also observed that cutting force is stabilized faster for small chip thicknesses.
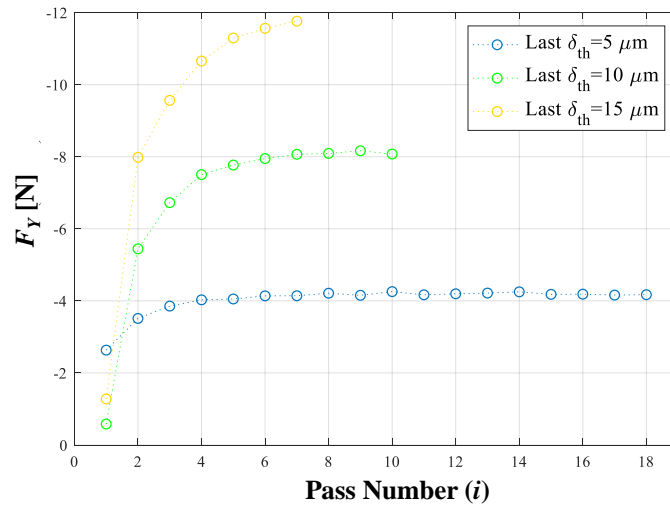
**Figure 2.25: Correlation between the main component of the cutting force and chip thickness of the CCA implementation**
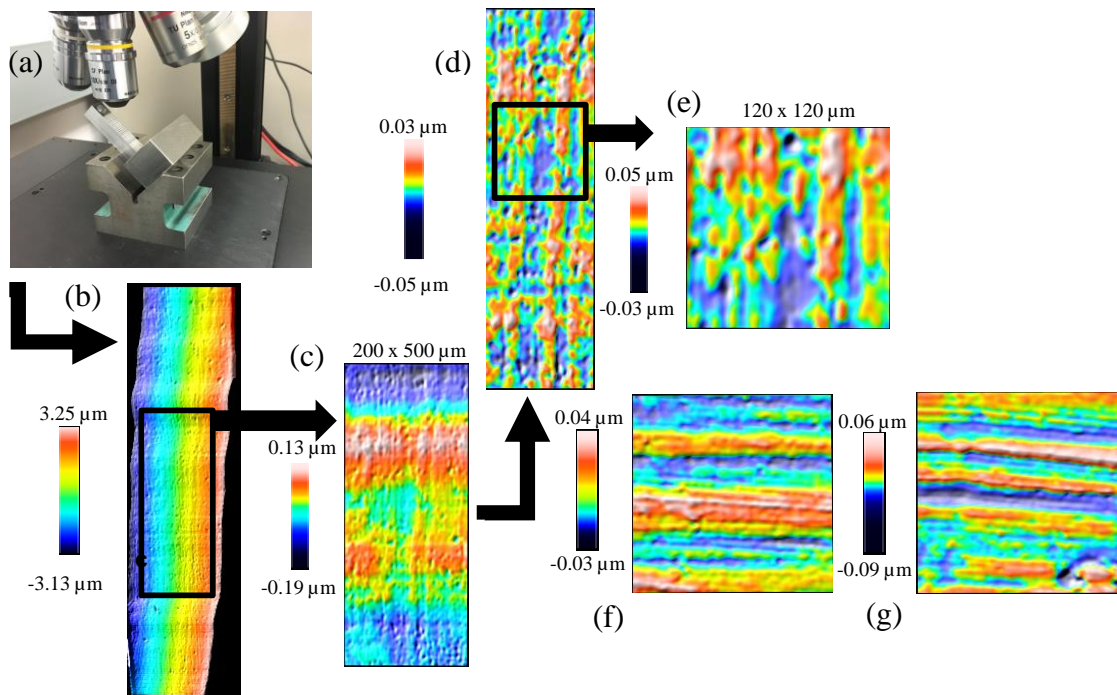


**Figure 2.26: V-groove surface quality for CCA: (a) measurement set-up, (b) raw topographic data, (c) post-planar form removal data, (d) isolated surface roughness; V-groove surface topography for last chip thickness set as: (e) 5 µm; f) 10 µm; g) 15 µm.**

This might indicate the effect of chip thickness in the magnitude of the cutting force reduces with the decrease of the chip thickness. In other words, the cutting area term showed in equation 8 becomes more predominant as the chip thickens is reduced.

In addition to cutting force, surface quality the micro V-grooves were also assed here by mean of high-resolution optical profilometer. The process used to assess the surface quality is similar to the one presented in the previous variant of the cutting strategy. From the raw data measurement of the application of the high pass filter, the final result of the sequential data processing steps presented in Figure 2.26. The results presented on Table 2.4 suggest that an areal surface roughness can be generated through the proposed cutting strategy. These results confirm the common machining theory that of using the smallest pass in the last cut to ensure the best surface quality.

**Table 2.4. Summary of surface quality measurements for CCA**

| Last Chip thickness (µm) | $S_a$ (nm) |
|---|---|
| 5 | 9.77 |
| 10 | 12.98 |
| 15 | 13.97 |

Chapter 3

# 3    One-Side Cutting Strategy

Building from the foundation set with the investigation of the conventional strategy for V-groove manufacturing in chapter 2, a second strategy is investigated using a non-conventional way for fabrication. As opposed to the axial strategy, material removal follows a pattern of cutting from one side of the groove until the last pass on the opposite side. Here, the V-groove is fabricated from one side only; consequently, making use of one cutting edge of the tool. Besides providing an alternative for the fabrication of V-grooves, the proposed strategy aims to eliminate the formation of burrs that happens in the use of conventional strategies as well the breakage/bend of the tips of the groove tips when high aspect ratio arrays are fabricated. The development of the one-side strategy is thoroughly presented in this chapter which its two variants, that is the CCT and the CCA.

## 3.1    Definition and Implementations of the One-Side cutting strategy

The current cutting strategy is termed "one-side" due to the nature of its kinematics. Here, the tool not only moves in the YZ plane, but it also moves along the negative X-axis. In all cutting passes, the tool follows a repeated sequence of down-across-up in the YZ plane before it transitions to the next cutting pass moving in the X-axis (Figure 3.1a). As illustrated in Figure 3.1b cutting will take place while the tool travels from $P_a$ to $P_b$ in the negative Y-direction. This is followed by an upward ancillary motion that prepares the tool to transition to the cutting of the following chip. The transition occurs from $P_b'$ to $P_a'$ as shown in Figure 3.1a.

The presentation of the one-side cutting strategy also involves two main variants: cutting with constant chip thickness (CCT) and cutting with constant cutting area (CCA). Here, the core characteristic of CCT remains the representation by the constant value of its chip thickness ($\delta_{th} = const$). The constant chip thickness translates into a constant depth of cut associated with points $P_1$, $P_2$, $P_3$ and $P_4$ as illustrated in Figure 3.2. However, despite the constant depth of cut, the area and volume of material being removed increases on each cutting pass ($A_{th} = var$). Therefore – as shown in the previous – the magnitude of the

cutting force increases linearly with each pass. This linear increase is caused by the known proportionality between cutting force and area of material removed.
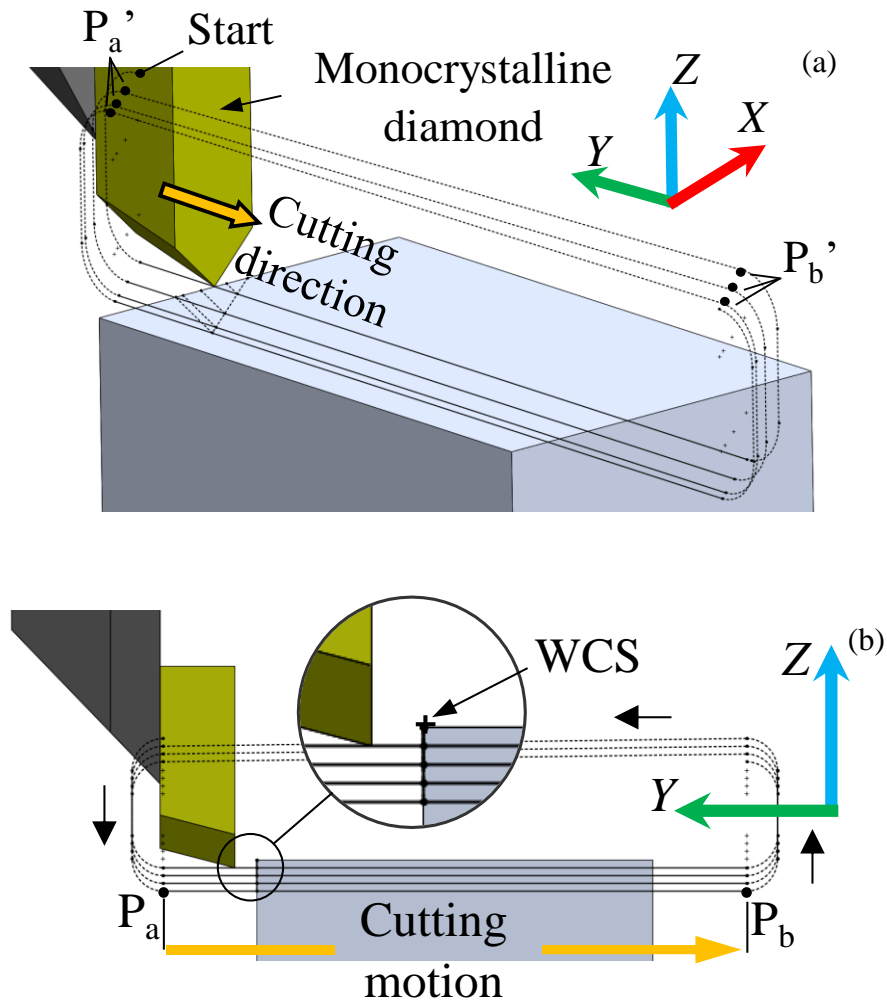


**Figure 3.1: Cutting kinematics: a) Isometric view; b) side view along the +X direction**

With the maxim amount of load that can be tolerated by the tool remaining unknown in the beginning of the cutting process, the constantly increasing cutting forces may have negative impact on tool life, wear and surface quality even though only one edge of the cutting is used. Therefore, sudden tool breakages remain possible. The CCA, however, still alleviates some of the aforementioned limitations of the CCT technique. The direct relationship between the cutting area and cutting force implies that cutting force will

remain constant in the current CCA implementation. As such, unlike CCT, cutting force thresholds can be set in advance in order to avoid tool overload/breakage. However, the effect of using of a single tool edge remains an interesting aspect, wich will be further explored on both implementations.

## 3.2 One Side Cutting Strategy with Constant Chip Thickness

### 3.2.1 Mechanics of CCT Implementation

In the CCT implementation, the tool steps down further at the beginning of the new "across" motion and is always positioned at the bottom of the groove that will be cut (Figure 3.2). The constant chip thickness ($\delta_{th}$) at which the profile is being cut makes the distance between the $P_1$, $P_2$, $P_3$, and $P_4$ points to remain constant.  The only exception from this rule might be constituted by the first pass across the workpiece that might happen at a layer thickness that is smaller than $\delta_{th}$. This is typically caused by the impossibility to adequately determine the position of the tool tip.

The one-side cutting strategy employs cutting with a constant chip thickness at each pass across the workpiece. Nevertheless, the first cut typically has a chip thickness smaller than δth. The small chip thickness ($< 20$ μm) and workpiece surface tolerances make the accurate setting of the Z-height of the tool tip relatively difficult. Because of this, the first across cut at d1 is always accompanied by an inherent error. By assuming that this error is within the range of $\Delta d$ $(\Delta d = d_n - d_{n-1})$, then $d_1 = \Delta d_{-\Delta d}^{+0.0}$ . In this strategy, the chip thickness is assumed as constant, therefore after the first cutting pass, the depth becomes $d_n = (d_{n-1} + \Delta d)_{-\Delta d}^{+0.0}$ . Based on the error in setting d1 value and by assuming that a negligible manufacturing error is associated with tool's included angle ($\alpha$), the error with respect to the cross-section area can be determined as $e_A = A_{-\Delta d^2}^{+0.0}$ .
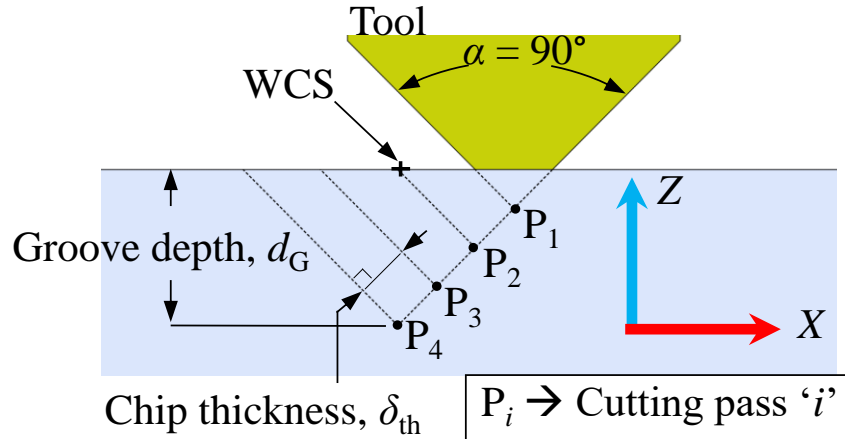
**Figure 3.2: Axial cutting of V-groove with constant chip thickness**

The following analytical relationships can be established based on the geometrical dependencies between the parameters used to characterize V-groove cutting motions (Figure 3.3):

$$\Delta d = \delta_{th} / \sin(\alpha / 2) \quad \textbf{(3.1)}$$

$$b_i = 2d_i \tan(\alpha / 2) \quad \textbf{(3.2)}$$

$$A_{i\blacktriangledown} = b_i d_i / 2 = d_i^2 \tan(\alpha / 2) \, \textbf{(3.3)}$$

In the above relationships, the combination between depth of cut ($\Delta d$ in (3.1)) and base of the triangle ($b_i$ in (3.2)) enables determination of the cutting area of the first cut (*i.e.*, a complete triangle in Figure 3.4) as shown in (3.3). However, this type of calculation is not valid for the subsequent cuts that are depicted by the alternating blue-toned colours in Figure 3.4, for which triangular area subtraction has to be used.
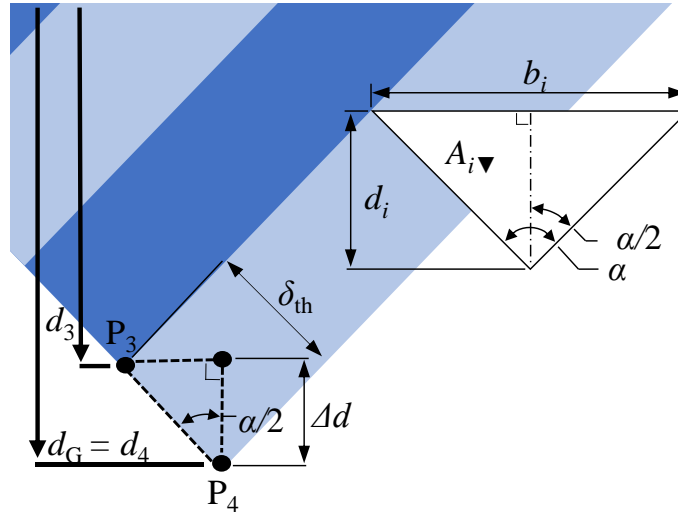
**Figure 3.3: Geometric parameters associated with the symmetrical V-groove characterized by an included angle α: a) CCT implementation**

$$A_i = A_{i\blacktriangledown} - A_{(i-1)\blacktriangledown} \quad \textbf{(3.4)}$$

An overview of cutting area calculations is presented in Figure 3.5. The linear dependence noticeable in the plot will be validated further against experimental measurements of the main component of the cutting force, essentially acting along Y-axis direction.
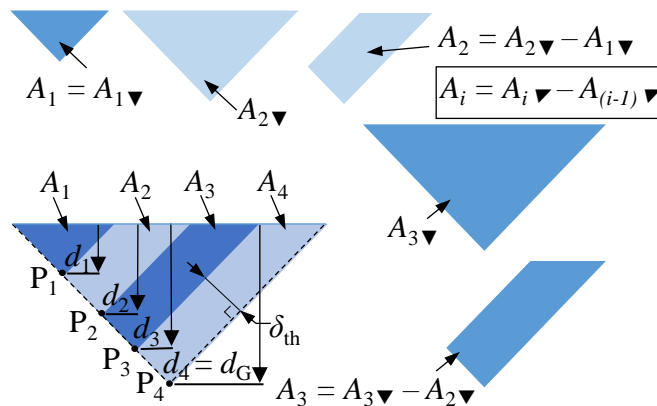


**Figure 3.4: Dependence between cutting area and cutting pass for CCT implementation**
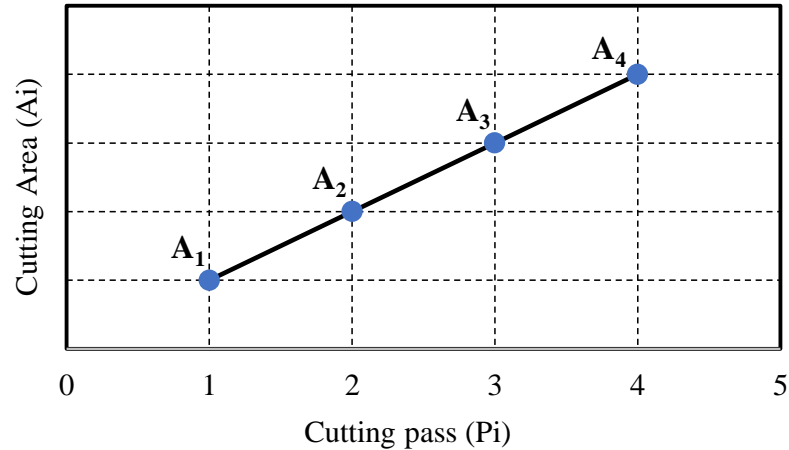
**Figure 3.5: Graphical representation of the dependence between cutting area and cutting pass of the CCT implementation**

Although, the trend of the dependence between the cutting area and cutting pass of the CCT implementation shown in Figure 3.5 resembles the one shown in the previous chapter for the axial cutting strategy, the mainly differ in the magnitude. The magnitude of the cutting area, which affects the magnitude of the cutting force, is smaller in the one-side cutting strategies due to the use of a single cutting edge of the tool.

## 3.2.2    Toolpath Planning

Here, the same software programs mentioned in in chapter were used for postprocessing and toolpath planning: MatLab and Vericut. The analytical calculations of the depth of cut/cutting area allowed the generation tool path for visualization as well as an NC code for machining. Figure 3.6 illustrates the toolpath plotted using MatLab, which is similar for both implementations of the one-side cutting strategy.

Vericut allowed not only allowed the visualization and verification of the tool path, but it also allowed an accurate visualization of the V-groove structure created as illustrated in Figure 3.7. A constructed CAD model of the machining center allowed for the accurate simulation of the fabrication process of the V-groove microstructure. Figure 3.7 illustrates the stages of the fabrication process simulated in Vericut. After the simulation of the cutting process in Vericut, the NC code was iterated for any mistakes observed

before loading it in the machining center. This guaranteed the safety of the experiment as well as the avoidance of any unexpected error in the tool trajectory which would affect the resulting microstructure created.
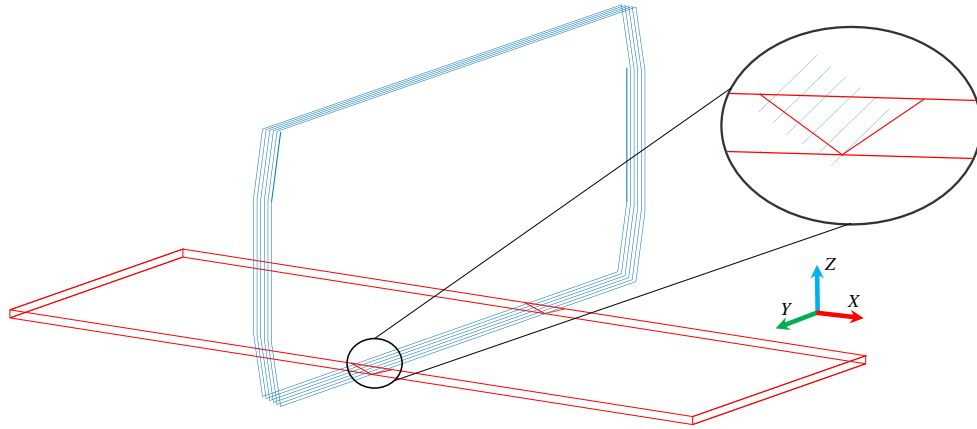


**Figure 3.6: Tool Path illustrator for CTC**

(a)

(b)
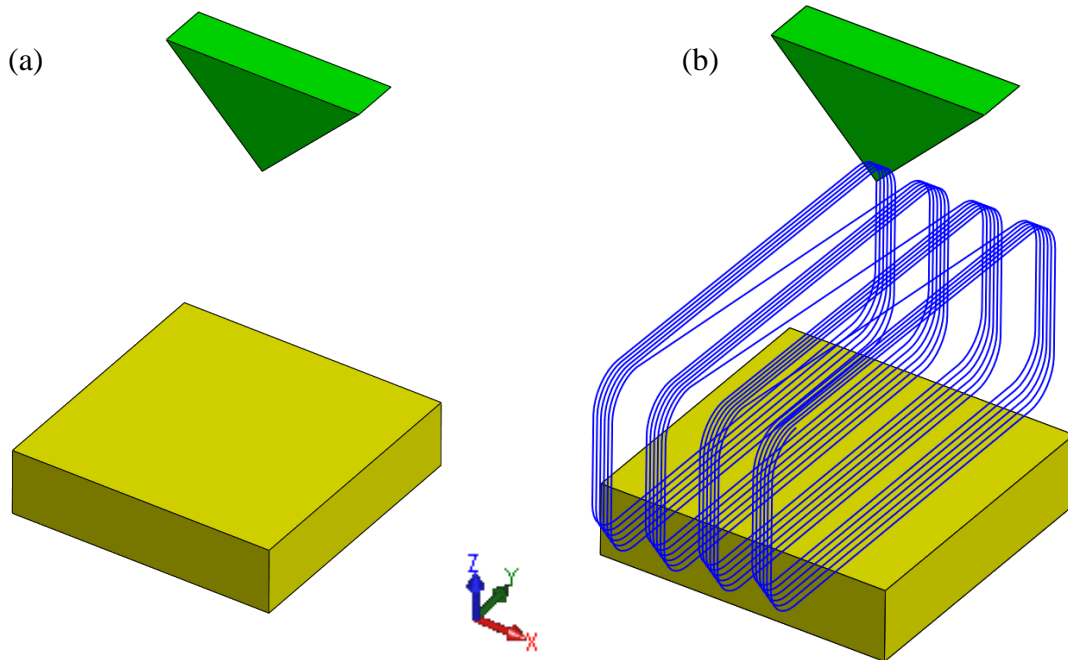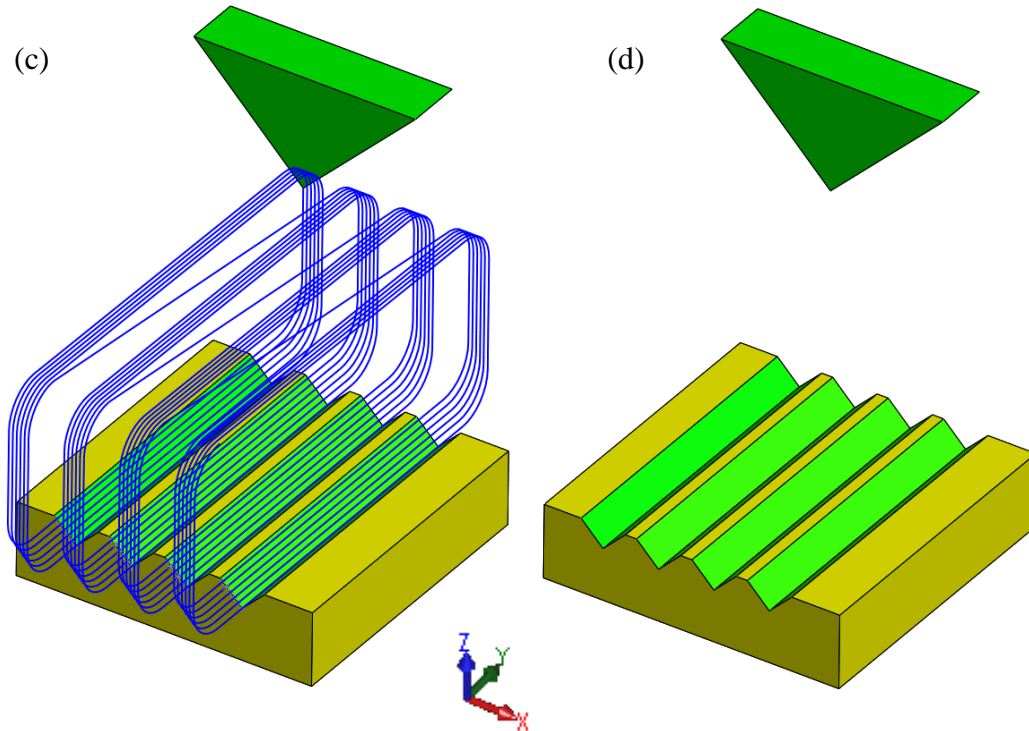
**Figure 3.7: Vericut fabricated V-grooves microstructures: (a) Uncut workpiece; b) Illustration of toolpath; (c) Cut grooves with toolpath; (d) Final grooves**

## 3.2.3    Simulation methods

Here, the simulation was run in Abaqus/Explicit with the same workpiece properties and model setup presented in the previous chapter.
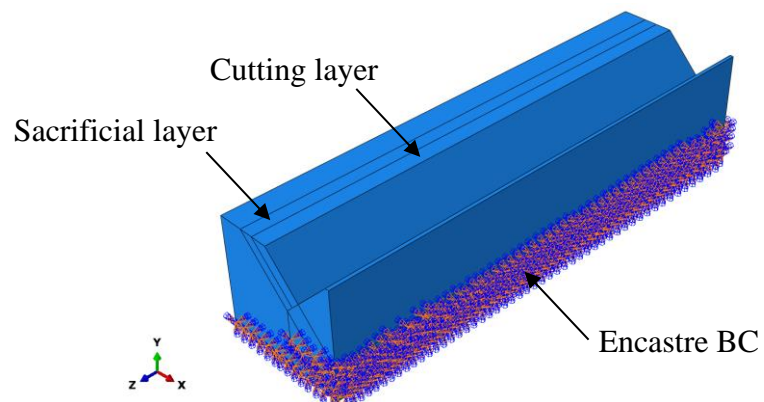


**Figure 3.8: Workpiece with BC and partitions**

Figure 3.8 illustrates the workpiece with a preexistent cut and the partitions made. The mesh size remained the same since the cut is also done with 15µm constant chip thickness.
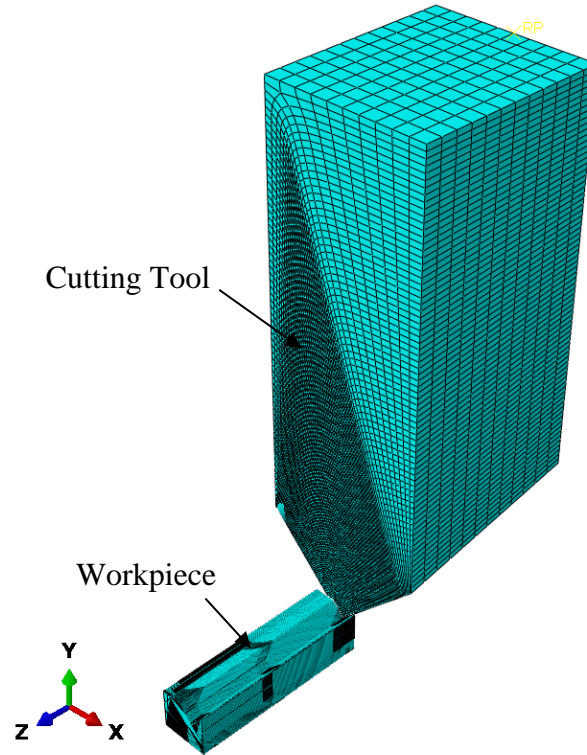


**Figure 3.9: Assembled model**

Figure 3.8 not only illustrates the assembled model, but also the quality of the mesh. As mentioned above, the element size remained the same as the one set in the previous chapter. This allowed the generation of the results to be presented here.

Passes 02 and 03 across the workpiece were simulated and the results are shown in Figure 3.10 and Figure 3.11. From these results it can be observed the generation of continuous chips, which match the morphology of the chips generated during the experiments. The cutting forces shown on the results, also show a good agreement with the magnitudes recorded during the experiments, later presented here. The magnitude of the simulated cutting forces lies within a 23% accuracy when compared to the

experimental ones. In addition, the results in both passes indicate the linear trend of cutting force, verifying the proportionality between the cutting force and the cutting area.
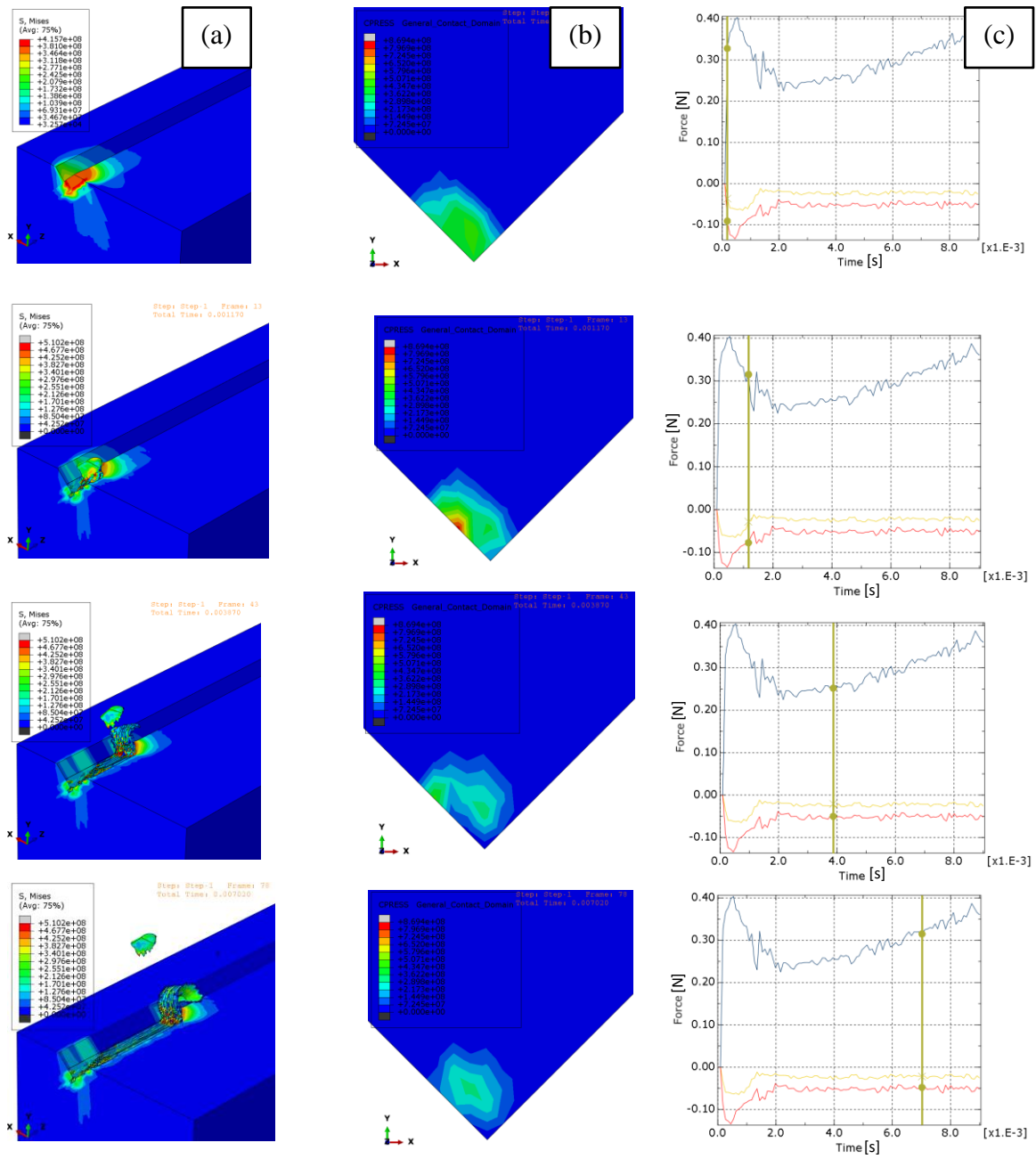


**Figure 3.10: Snapshots of FEA results for pass 02 of CCT: (a) workpiece; (b) Cutting tool: (c) Cutting forces**
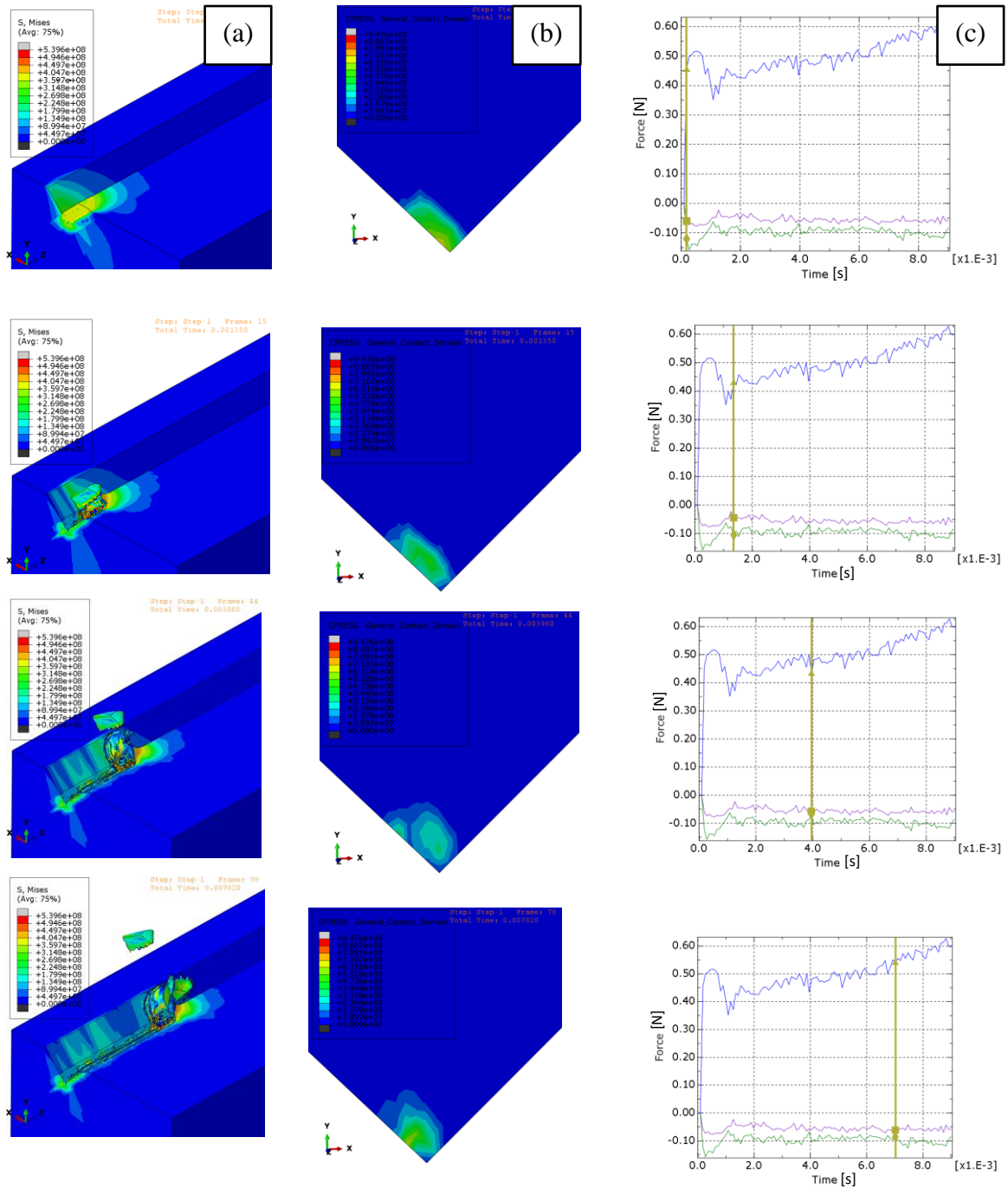
**Figure 3.11: Snapshots of FEA results for pass 03 of CCT: (a) workpiece; (b) Cutting tool: (c) Cutting forces**

## 3.2.4    Experimental Results and Analysis

The following experimental analysis used the same experimental setup described in the previous chapter. Table 3.1 summarizes the experimental parameters used during the experiments involving the implementation with CTC. All cutting trial were performed on an aluminum alloy 6061 workpiece. Following data acquisition procedure, advanced signal processing was applied to the recorded data using Matlab sofware. During the processing of the data, a low pass filter was applied on the converted LabView-formatted data to filter the high-frequency noise.

**Table 3.1. Summary of experimental conditions for CCT**

| Feed rate (mm/min) | 500 |
|---|---|
| Chip thickness (µm) | 5, 10, 15 |
| Coolant | Isoparaffin mist |
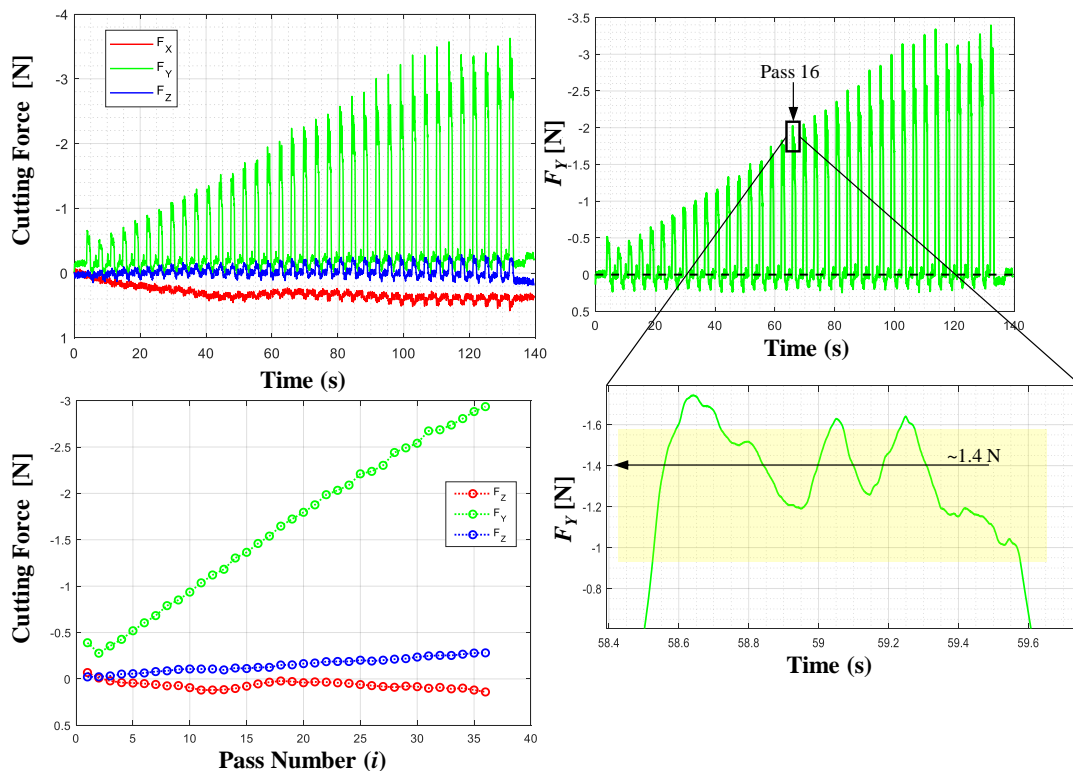


**Figure 3.12: Cutting force measurements for CTC: a) raw data; b) F$_Y$ with measurement drift corrected; c) sample of average F$_Y$ calculation; d) average F$_Y$ variation during microgroove cutting; e) average cutting force components.**

A LabView-based data acquisition system was used to monitor and record cutting force measurements. Figure 3.12 depicts an overview of the results obtained for cuts performed with a 10 µm chip thickness. As a data processing detail, a low-pass filter with a 10 Hz cut-off frequency was used to remove the high-frequency noise.

Data filtering enabled the extraction of the quasi-static component of the cutting force (Figure 3.12a). The analysis presented is focused on $F_Y$ (i.e., the component along the feed direction) since this represents the main contributor to the 3D cutting force magnitude as well as final surface quality of the V-groove facets. Each pulse in the cutting force signal (Figure 3.12a) represents a cut across the workpiece.

The next step in the processing of the data aimed the elimination of the cutting force drift introduced by the measuring system. This was done by subtracting the linear trend extracted from data regions associated with time intervals when tool was disengaged from the workpiece. After the drifting slope of the signal was determined and subtracted from raw measurements, all three cutting force components have returned to a quasi-null no-load value (Figure 3.12b).

A more in-depth analysis of the data presented in Figure 3.12c reveals that $F_Y$ signal fluctuations are present. It can be speculated that this might be a consequence of the initial impact between tool and workpiece, possibly translated into a damped vibratory response captured by the data acquisition system. The average values for each cutting force component are presented in Figure 3.12d. As expected, $F_X$ was measured at negligible values. Although in the kinematics of the strategy there is movement in the X-direction, the tool only goes along the Y-axis while it is in contact with the workpiece. $F_Z$, however, is not negligible and seems to slowly increase in magnitude. This might be a consequence of increased friction in the rake face of the tool. According to the predictions presented in Figure 3.5, $F_Y$ component follows a linear dependence with respect to the cutting passes. In addition to this, a strict dependence to chip thickness also exists as shown in Figure 3.13.
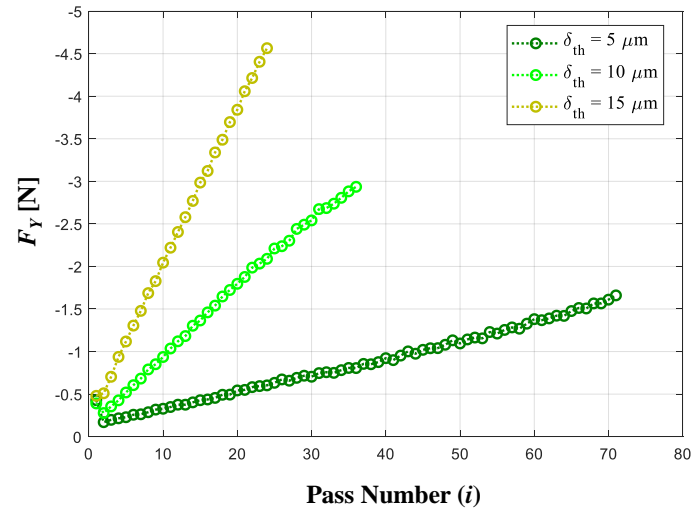
**Figure 3.13: Correlation between the main component of the cutting force and chip thickness of the CCT implementation**
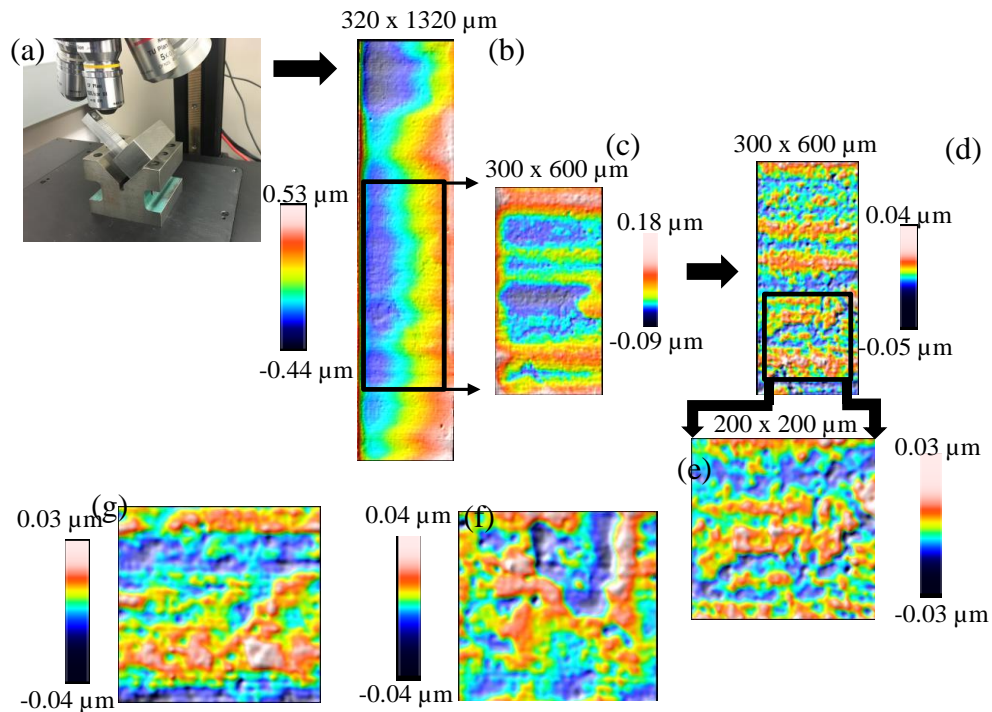


**Figure 3.14: Surface quality results for CTC: a) raw data; b) data with planar tilt removed; V-groove surface topography for: c) 5 μm chip thickness; d) 10 μm chip thickness; e) 15 μm chip thickness.**

Here we observe the same tradeoff between cutting forces magnitudes and machining time revealed in the previous chapter for the axial strategy. However, the magnitude of the cutting forces here are much lower when compared to those of the axial strategy. This is mainly due to the use of one cutting edge of the tool.

In addition to cutting force magnitude, the quality of V-groove facets was assessed by means of an optical profilometer. To accurately assess the surface quality of the microstructures, workpiece was tilted at 45° (Figure 3.14a), such that V-groove facets became normal to microscope's main measurement direction. A typical representation of V-groove facet is shown in Figure 3.14b.

The inclination present in the raw data (Figure 3.14b) caused by out-of-normal condition between V-groove facet and measurement direction was digitally eliminated via form plane removal technique (Figure 3.14c). Following this, a filter with cut-off wavelength of 80 µm according to ISO 16610-61 was applied to remove the surface waviness and retain just its roughness (Figure 3.14d). The final postprocessed topographic data is presented in Figure 3.14e-g. Table 2 summarizes the results of the areal average surface roughness measurements (Sa).

**Table 3.2: Summary of surface quality measurements for CCT**

| Chip thickness (µm) | $S_a$ (nm) |
|:---:|:---:|
| 5 | 6.3 |
| 10 | 8.4 |
| 15 | 9.8 |

The results presented on Table 3.2 reveal the strategy's ability to create ultraprecise structures with areal surface roughness.

## 3.3   One Side Cutting Strategy with Constant Cutting Area

### 3.3.1   Mechanics of CCT Implementation

According to the one-side constant-area strategy, the distance between points $P_1$, $P_2$,…$P_N$ and associated chip thickness ($\delta_i$) cannot be constant since it is determined by the preset

'constant cutting area' constraint. More specifically, by starting with a minimal final chip thickness ($\delta_{min} = \delta_N$), the developed post-processor has generated all intermediate cutting passes from the last to the first (i.e., $P_N$ to $P_1$), which in turns results in a gradually increasing chip thickness ($\delta_i$).
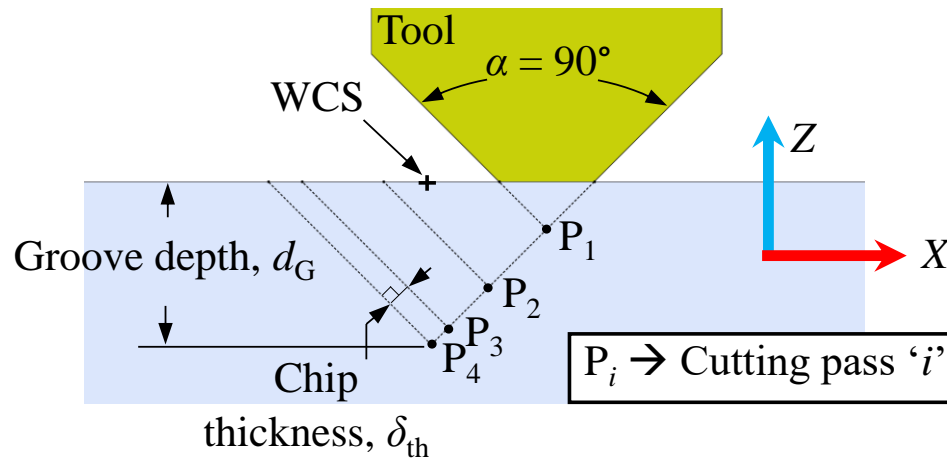


**Figure 3.15: Axial cutting of V-groove with constant cutting area**

The current strategy employs cutting with a constant cutting area. However, the first cut typically has a cutting area less than or equal to the desired 'constant area' parameter. This is mainly caused by a combination between the small chip thickness and workpiece surface tolerance that prevent the accurate setting of the Z-height of the tool tip. The main parameter of the analytical formulation is constituted by the area to be maintained throughout all passes. This value is heavily dependent on the desired final chip thickness ($\delta_N$). Subsequently, the position of the cutting tip for each cutting pass can be determined by means of the preset constant cutting area

The typical geometry of the V-groove is characterized by the cutting depth ($d_i$) and the groove included angle ($\alpha$) as shown in Figure 3.16. In order to determine the constant area of material being removed ($A_i$), trigonometric relationships involving cutting depth ($d_i$) and groove included angle ($\alpha$) were used to generate Eqs. 3.5-3.11.
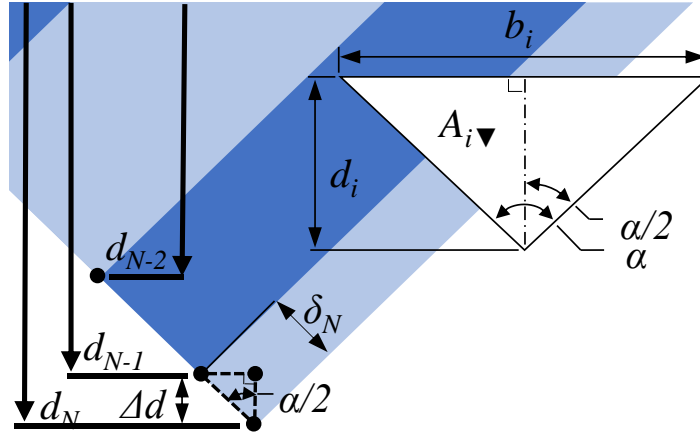
**Figure 3.16: Geometric parameters associated with the symmetrical V-groove characterized by an included angle α for the CCA implementation**

To minimize complexity, the analytical calculations of the constant cutting area and variable depth-of-cut have been initialized from the bottom of the V-groove profile. The chip thickness of the last cutting pass ($\delta_N$) enables determination of the second last depth-of-cut ($d_{N-1}$), subtracting the last change in depth, $\Delta d_N$, from the final depth of the groove ($d_{Groove}=d_N$), as indicated in Eqs. 3.5-3.6.

$$\Delta d_i = \delta_i / \sin\left(\alpha/2\right) \text{ (3.5)}$$

$$d_i = d_{i+1} - \Delta d_{i+1} \ i = 1,2,3\ldots(N\text{-}1) \text{ (3.6)}$$

In addition, the base of a full depth triangle illustrated in Eq. 3.7 can be combined with Eq. 3.7 to calculate the full area of a triangle as shown in Eq. 3.8. After that, the constant cutting area is obtained by subtracting the full depth triangle area of the current profile ($A_\blacktriangledown$) from the area of associated with the previous depth of cut ($A_{\blacktriangledown(N\text{-}1)}$) and similar iterative formulations can be used after that.

$$b_i = 2d_i \tan\left(\alpha/2\right) \text{(3.7)}$$

$$A_{\blacktriangledown i} = b_i d_i / 2 = d_i^2 \tan\left(\alpha/2\right) \text{ (3.8)}$$

$$A_{const} = A_i = A_{\blacktriangledown i} - A_{\blacktriangledown (i-1)}, \ i = 2, 3\ldots N \ \textbf{(3.9)}$$

$$A_{\blacktriangledown (i-1)} = A_{\blacktriangledown i} - A_{const} \ \textbf{(3.10)}$$

The formulas above will ensure that the cut performed as $d_{(N-1)}$ will be characterized by the same $A_{const}$. The following depth of cut ($d_{(N-2)}$) is determined by Eq. 3.11.

$$d_i = \sqrt{A_{\blacktriangledown i} / \tan(\alpha / 2)} \ \textbf{(3.11)}$$

Based on these calculations, the analytical dependence of cutting area on cutting pass/depth is illustrated in Figure 3.17. As shown in the graph, the very first cut/pass remains the only one characterized by a cutting area equal or less than $A_{const}$.
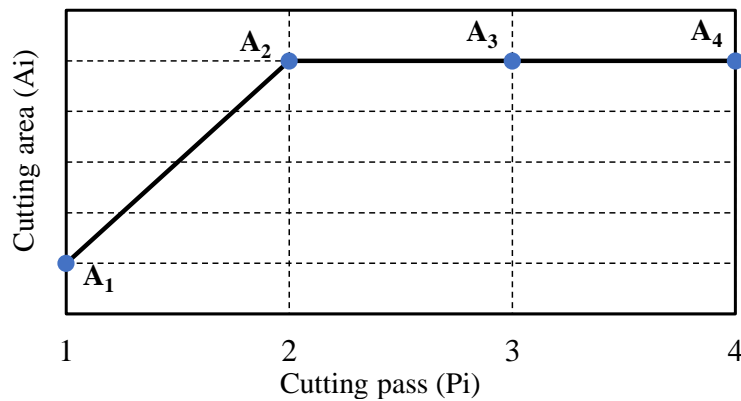


**Figure 3.17: Graphical representation of the dependence between cutting area and cutting pass: for the CCA implementation**

The common characteristic of cutting with a constant cutting area, makes the graphical representation of the dependence between cutting area and cutting pass show in Figure 3.17 be similar to one presented in the previous chapter. However, both strategies differ in magnitude. The amount of material removed during the cutting with the axial strategy is greater when compared which the one-side cutting strategy. This difference becomes very clear for observation on the force plots, due to the fact that the amount of material removed is directly proportional to cutting force.

## 3.3.2 Simulation methods

The results shown Figure 3.18 Figure 3.19 illustrate the formation of a continuous chip as well as cutting forces within a 18% accuracy when compared to the experiment results. In addition, they also illustrate the constant trend of the cutting force. Here the constant cutting area is characterized by a set final chip thickness of 5µm.

Moreover, one's attention is turned to the magnitude of the cutting force which are significantly higher than those for CCT implementation. This magnitude is explained by the fact that the smallest chip here is set as 5µm. As described in the previous sections, the subsequent chips have thickness higher than 5µm, however with the same cross-sectional cutting area. The redistribution of the cutting force in the cutting tool is also noticed here, manifesting as fluctuations on the force plots.
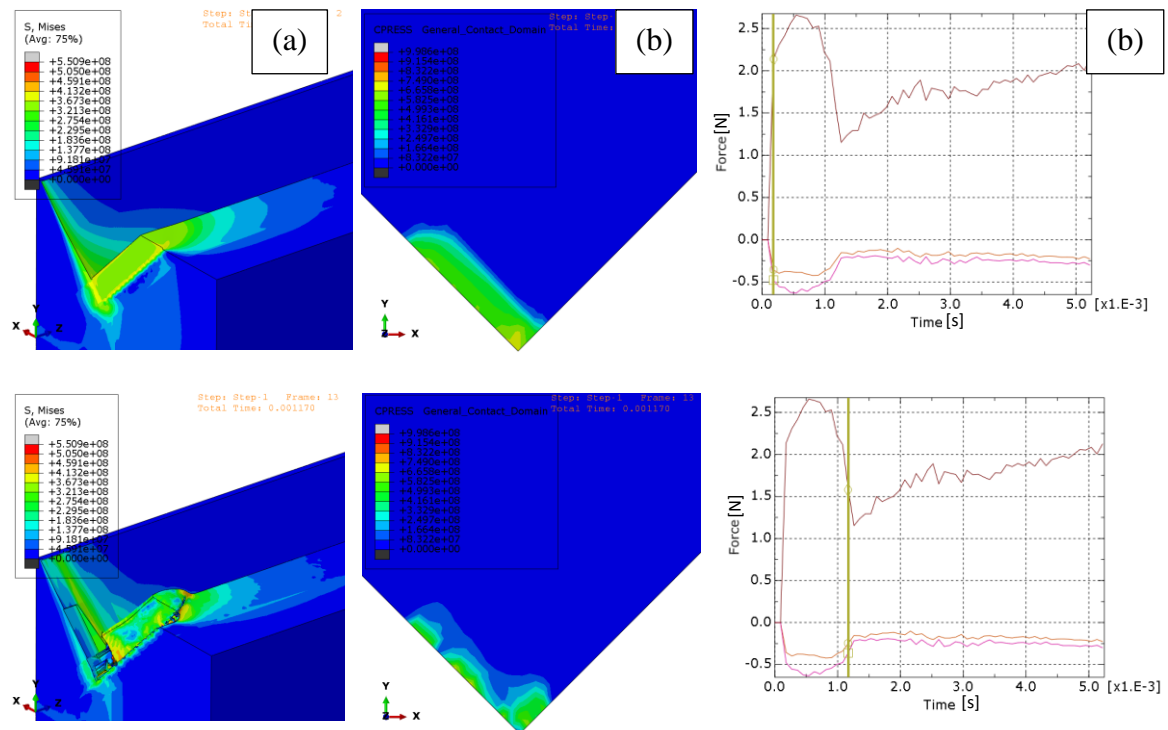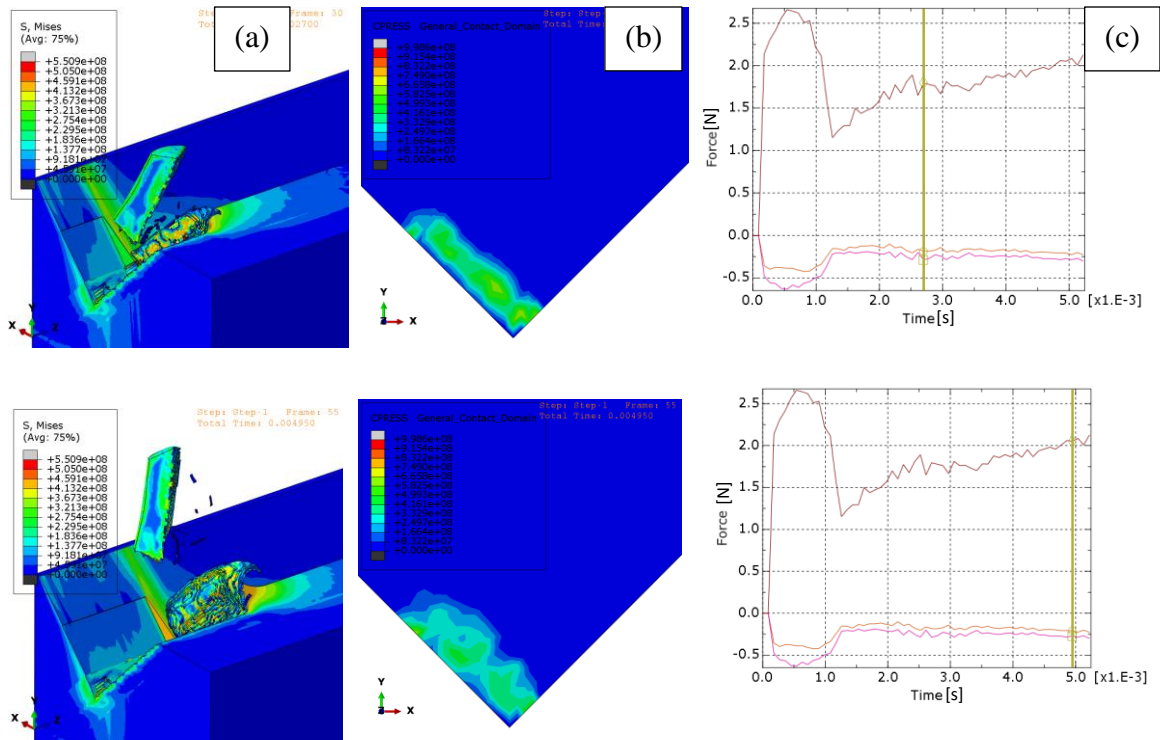
**Figure 3.18: Snapshots of FEA results for pass 02 of CCA: (a) workpiece; (b) Cutting tool: (c) Cutting forces**
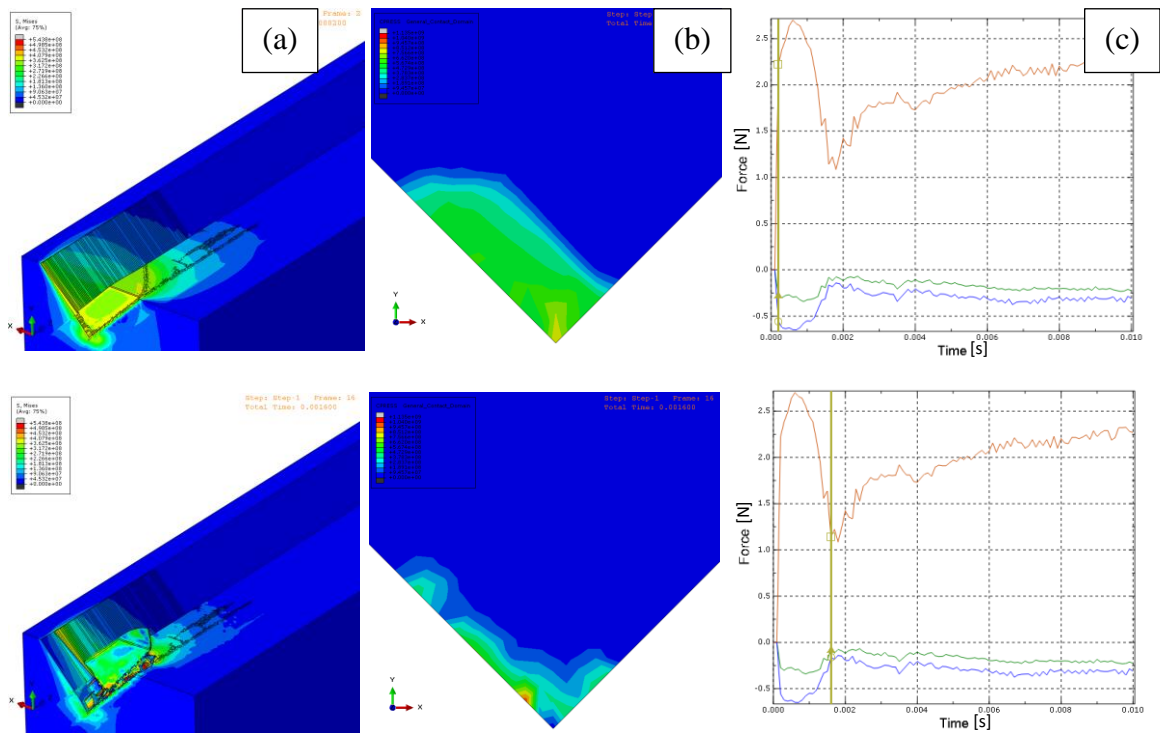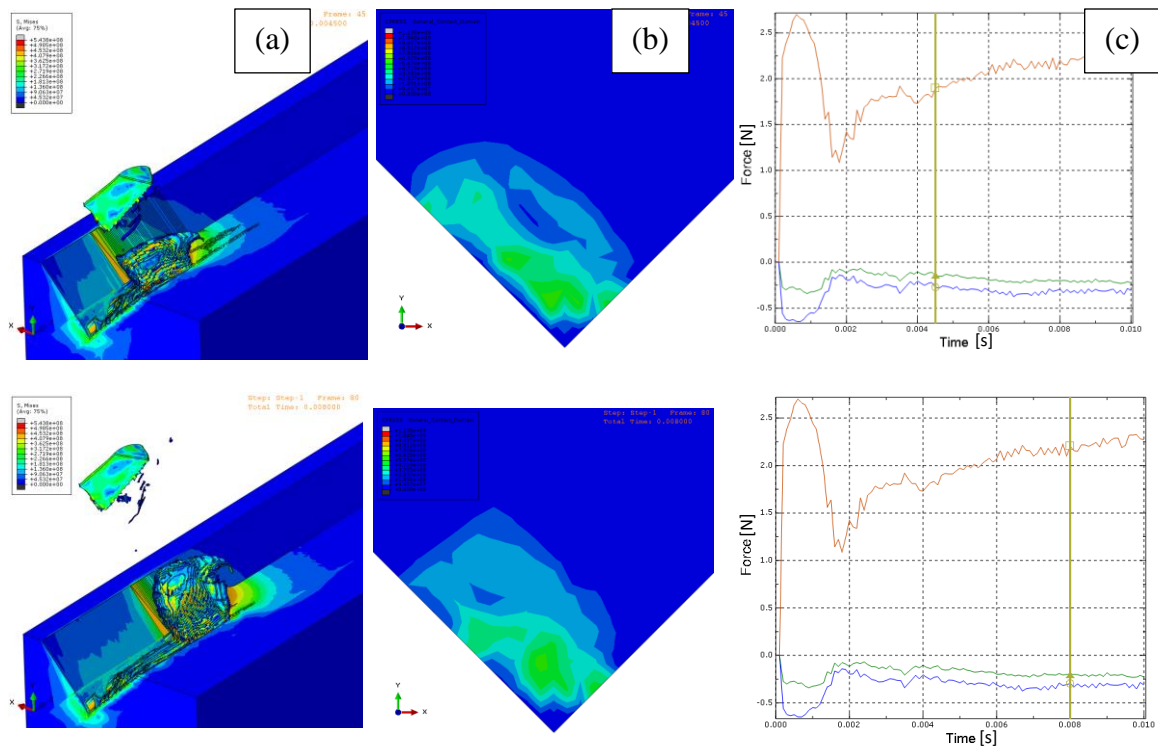
**Figure 3.19: Snapshots of FEA results for pass 03 of CCA: (a) workpiece; (b) Cutting tool: (c) Cutting forces**

On both passes the same response is observed on the force profile. The initial spike in magnitude can be explained by the illustration of the redistribution of the cutting force on the tool, which shoes that a greater area is pushed against. As the tool progresses across the workpiece, this redistribution changes and the magnitude of the cutting force becomes more stable.

### 3.3.3    Experimental Results

Table 3.3 summarizes the experimental parameters used in the study of the CCA implementation of the one-side cutting strategy. Cutting trials were also performed on an aluminum 6061 block.

**Table 3.3: Summary of experimental conditions for CCA**

| Feed rate (mm/min) | 500 |
|---|---|
| Final chip thickness (µm) | 5, 10, 15 |
| Coolant | Isoparaffin mist |

The previously developed LabVIEW-based data acquisition system was used to record cutting force data. Figure 3.20 depicts an overview of the results obtained, diplaying a last chip thickens set as 10 µm.
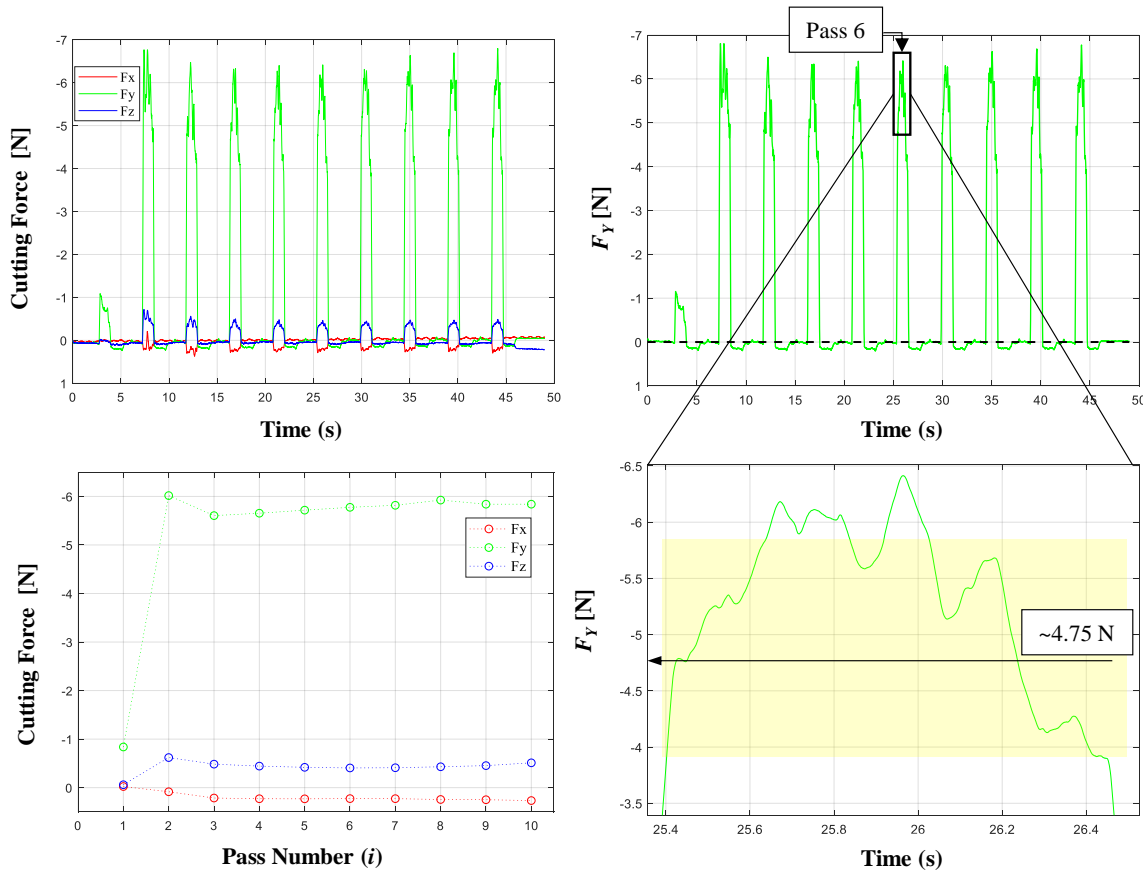


**Figure 3.20: Cutting force analysis for CCA: a) raw data; b) drift-corrected $F_Y$ component; c) typical $F_Y$ fluctuation and $F_Y$ average value; d) average cutting force values.**

The components of the force ($F_X$, $F_Y$, $F_Z$) were measured for an entire cycle of a V-groove fabrication. Following the processing of the data, a low pass moving average filter with a sampling rate of 2 kHz and a window of 200 data points was used filter was used

to smooth the high-frequency noise from the raw data. This step yielded the filtered raw data of all cutting forces presented in Figure 3.20a. The analysis presented here is focused on $F_Y$ (cutting force component along the feed direction) since this represents the main contributor to the 3D cutting force magnitude and surface quality formation. Each pulse in the cutting force signal (Figure 3.20a) represents a single cut across the workpiece.

As presented on previous chapters, the next step in data processing focused on the elimination of the visible data drift that was likely introduced by the employed measurement system. Figure 3.20b shows the resulting horizontally levelled position of the forces. Here, the force signals exhibited the same fluctuations on each pulse (Figure 3.20c), possibly caused the initial impact between the tool and workpiece, which was processed by taking an average value of all each pulse corresponding to a pass across the workpiece.  The average values for each component of the cutting force are presented in Figure 3.20d.  As expected, $F_X$ was measured at a negligible value. $F_Z$, however, is not negligible and seems to be maintained fairy at a constant value. As previously mentioned, $F_Y$ constitutes the largest contributor to the axial cutting force and its magnitude remained constant throughout the entire V-groove fabrication process, with the only exception being the first pass which is affected by the previously explained challenge in setting the tool Z-height.
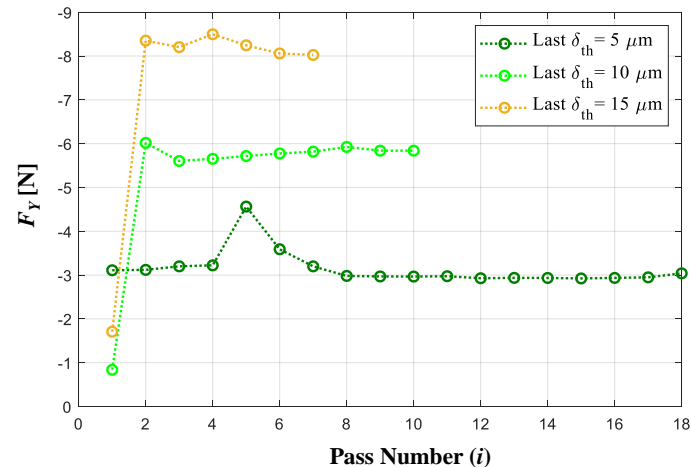


**Figure 3.21: Correlation between the main component of the cutting force and chip for the  CCA implementation**

Figure 3.21 illustrates the correlation between the main components of the cutting force and the chip chips for the CCA implementation. Here the same tradeoff between the low force magnitudes for lower chip thicknesses and short machining time for higher chip thicknesses is observed. However, the force magnitude gets one's attention. Here the force magnitudes are observed higher than in the CCT implementation. This maybe explained by the fact the chips are thicker for the CCA implementation, which accommodate the constant cutting area.
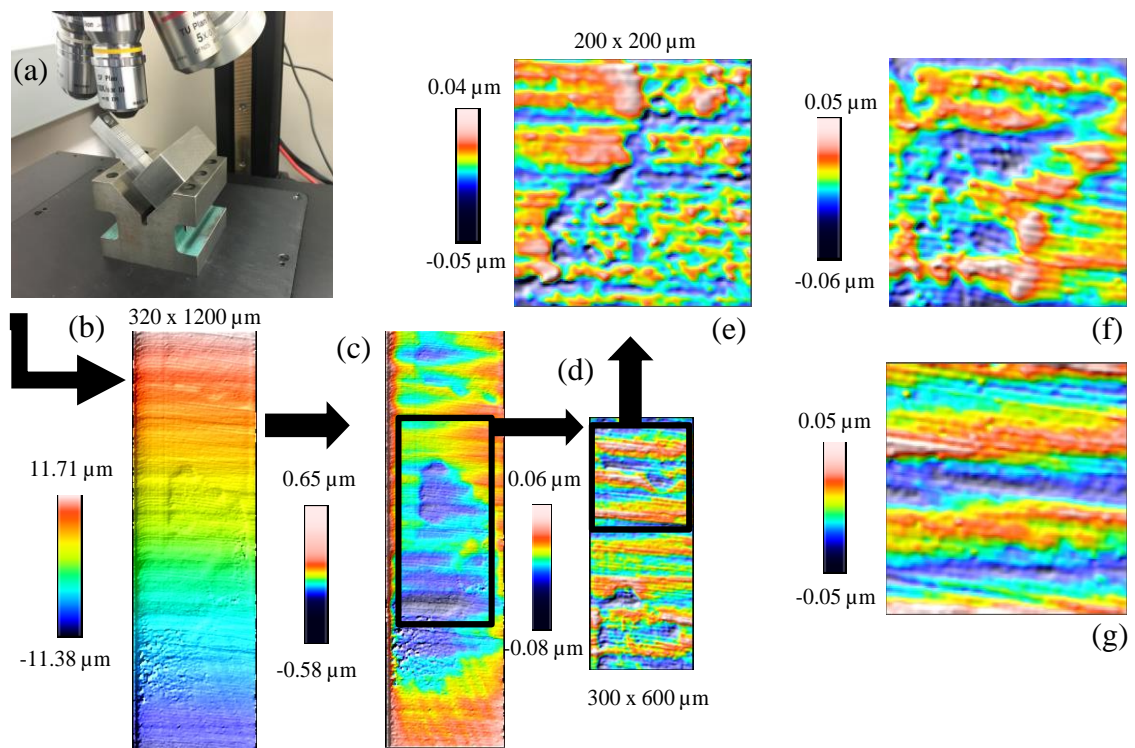


**Figure 3.22: V-groove surface quality for CCA: a) measurement set-up, b) raw topographic data, c) post-planar form removal data, d) isolated surface roughness; V-groove surface topography for last chip thickness set as: e) 5 µm; f) 10 µm; g) 15 µm.**

In addition to the cutting force results, the surface of the micro grooves were assessed by means of an optical profilometer. The procedure here, was not different than the one presented on previous chapters. Starting from the tilt of the workpiece by a 45° angle to

accurately measure the surface generated (Figure 3.22*a*), the effect of the effect of the remaining inclination was then removed through a planar removal technique (Figure 3.22*b*). Again, the last previous step was followed by the application of a filter with a cutoff wavelength of 80µm (ISO 16610-61) in order to eliminate surface waviness and retain only its roughness (Figure 3.22*d*). The final topographic data is shown in Figure 3.22*e*. The resulting roughness presented on Table 3.3 reveals that the cutting strategy is capable of producing ultraprecise surfaces.

**Table 3.4: Summary of surface quality measurements for CCA**

| Chip thickness (µm) | $S_a$ (nm) |
|---|---|
| 5 | 9.77 |
| 10 | 12.33 |
| 15 | 14.75 |

Chapter 4

# 4    Alternating Flank Cutting Strategy

On this last strategy, new approach is explored, making use of both cutting edges, however, alternatively. This approach aims to gradually remove a small amount of material from the desired groove; therefore, exerting less force. In contrast to one-side cutting strategy, material removal follows a pattern going from the sides of groove to the center. The presentation of the strategy starts with a general description, followed by the development of the mechanical model. The previous section is followed, by the description of the tool path planning, a presentation of simulation methods, and, finally, a presentation and discussion of experimental results.

## 4.1    Alternating Flank Cutting

The nature of the kinematics of the current strategy the major influence on terming it as "alternating flank cutting". Similar to the one-side cutting strategies, the tool not only moves in the YZ plane, but it also moves along the X-axis. However, here both cutting edges of the toll are used alternatively.
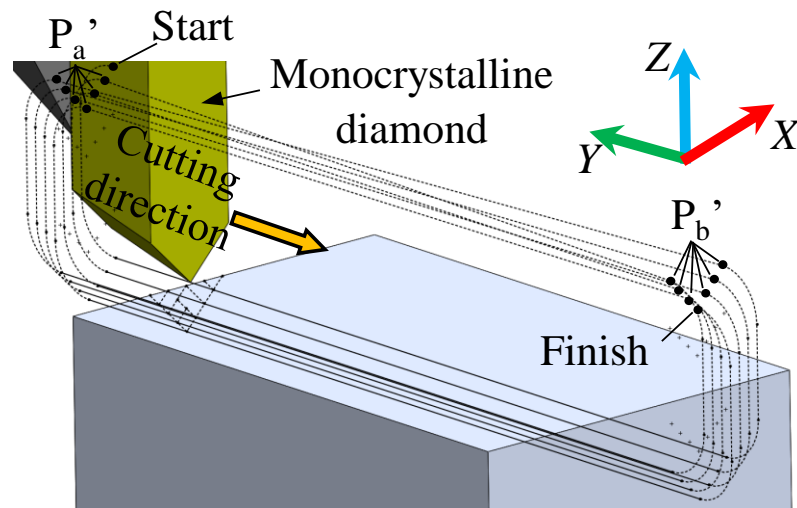


In all cutting passes, the tool follows a repeated sequence of down-across-up in the YZ plane before it transitions to the next cutting pass moving in the X-axis (Figure 4.1a). Moreover, as illustrated in Figure 4.1b, cutting will take place while the tool travels from

$P_a$ to $P_b$ in the negative Y-direction. This is followed by an upward ancillary motion that prepares the tool to transition to the cutting of the following chip. The transition occurs from $P_b$' to $P_a$' as shown in Figure 4.1a.
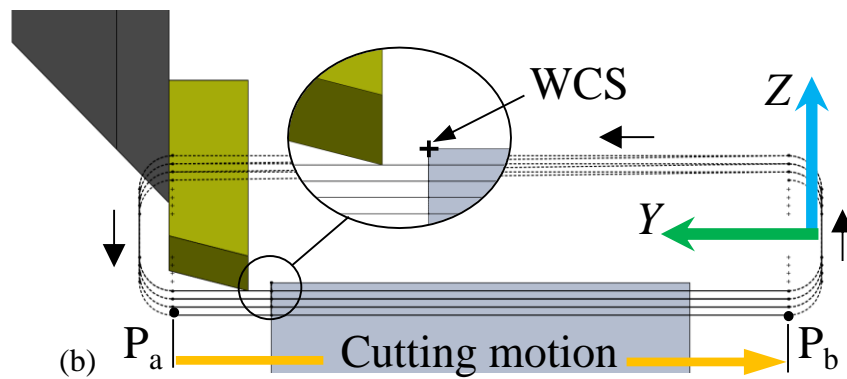


**Figure 4.1: Cutting kinematics: a) Isometric view; b) side view along the +X direction**

## 4.1.1    Mechanics of alternating flank cutting strategy

As in the previous strategies, the tool steps down further at the beginning of the new "across" motion and is always positioned at the bottom of the groove that will be cut (Figure 4.2).
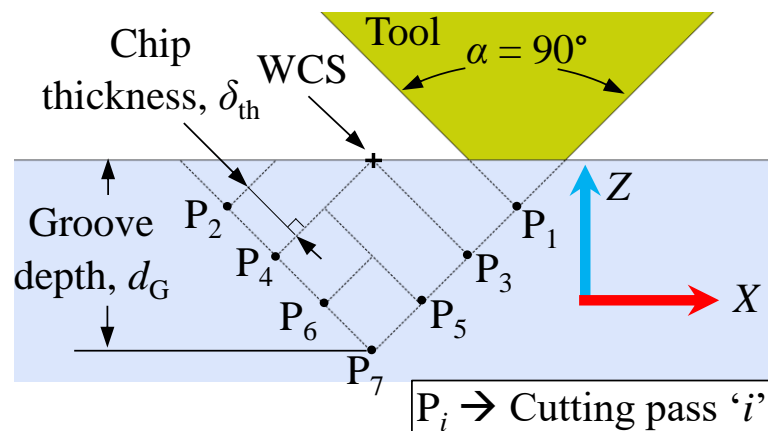


**Figure 4.2: Axial cutting of V-grooves: a) with constant chip thickness**

The constant chip thickness ($\delta_{th}$) at which the profile is being cut makes the distance between the points $P_1,\ldots P_7$ to remain constant. As in the previous chapters, the only exception from this rule might be constituted by the first two passes ($P_1$ and $P_2$) across the workpiece that might happen at a layer thickness that is smaller than $\delta_{th}$. This is typically caused by the impossibility to adequately determine the position of the tool tip. Nevertheless, the first cut typically has a chip thickness smaller than $\delta_{th}$.

The first cuts across the workpiece $d_1$ and $d_2$ (Figure 4.4) are, again, accompanied by an inherent error. This is mainly caused by the small chip thickness ($< 20$ μm) and workpiece surface tolerances that make the accurate setting of the tool tip relatively difficult. By assuming that this error is within the range of $\Delta d$ ($\Delta d = d_n - d_{n-1}$), then $d_1 = \Delta d^{+0.0}_{-\Delta d}$. In this strategy, the chip thickness is assumed as constant, therefore after the first cutting pass, the depth becomes $d_n = (d_{n-1} + \Delta d)^{+0.0}_{-\Delta d}$. Based on the error in setting $d_1$ value and by assuming that a negligible manufacturing error is associated with tool's included angle ($\alpha$), the error with respect to the cutting area can be determined as $e_A = A^{+0.0}_{-\Delta d^2}$.

Here in the alternating flank cutting the typical geometry of the V-groove is, also, characterized by cutting depth ($d_i$) and groove included angle ($\alpha$) as shown in Figure 4.3. However, the formulation to determine the cutting area of material being removed ($A_i$) is divided in two parts, the first part relying on trigonometric relationships of triangles and the second one relying simply to geometry of rectangles.

For the first part of the cutting area formulation, Eqs. 4.1-4.4 are formulated based on the typical parameters and by employing elementary trigonometric relationships. The analytical relationships can be established.

$$\Delta d = \delta_{th} / \sin(\alpha / 2) \text{ (4.1)}$$

$$b_i = 2d_i \tan\left(\alpha / 2\right) \text{(4.2)}$$

$$A_{i\blacktriangledown} = b_i d_i / 2 = d_i^2 \tan\left(\alpha / 2\right) \text{(4.3)}$$
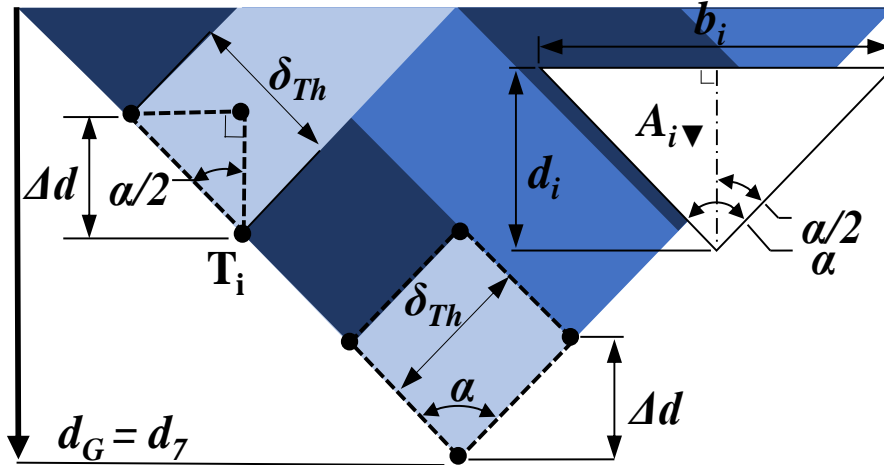
**Figure 4.3: Geometric parameters associated with the symmetrical V-groove characterized by an included angle α for alternating flank cutting strategy**

$$A_i = A_{i\blacktriangledown} - A_{(i-1)\blacktriangledown} \textbf{ (4.4)}$$

In the above relationships, the combination between depth of cut ($\Delta d$ in (4.1)) and base of the triangle ($b_i$ in (4.2)) enables determination of the cutting area of the first cut (*i.e.*, a complete triangle in Figure 4.4) as shown in (4.3). However, this type of calculation is not valid for the subsequent cuts that are depicted by the alternating blue-toned colours in Figure 4.4, for which triangular area subtraction has to be used. Point $T_i$ marks the transition from triangular geometrical analysis to the rectangular. The area of the first rectangle can be calculated as in Eq. 4.6, where $d_i'$ corresponds to the length of the first rectangle which can be calculated as in 4.5.

$$d_i' = d_i / \cos(\alpha / 2) \textbf{ (4.5)}$$

$$A_i' = d_i' \delta_{Th} \textbf{ (4.6)}$$

$$A_n = A_{n-1} - n\delta_{Th}^2 , n = 1, 2\ldots N \textbf{ (4.7)}$$

$$A_{n+1} = A_n \textbf{ (4.8)}$$

For the subsequent cuts the cutting area can be calculated as in 4.7, where the square of the chip thickness is subtracted from the previous area calculated.
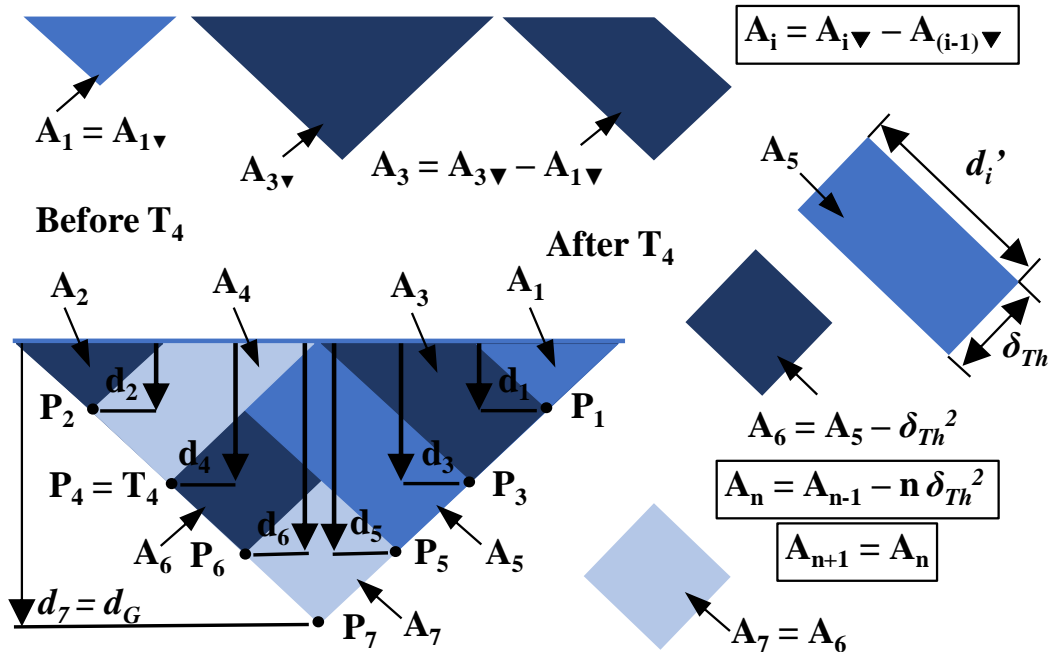


**Figure 4.4: Dependence between cutting area and cutting pass for alternating flank cutting strategy**

An overview of cutting area calculations is presented in Figure 4.5. The trend shown in the of the plot is somewhat obvious from Figure 4.5. Triangular cutting area are perfectly duplicated until the transition to the rectangular ones. The cutting pass after the transition represents the biggest cutting area. After this, the area is also duplicated as illustrated in Figure 4.5. The trend shown in the plot will be validated further against experimental measurements of the main component of the cutting force, essentially acting along Y-axis direction.
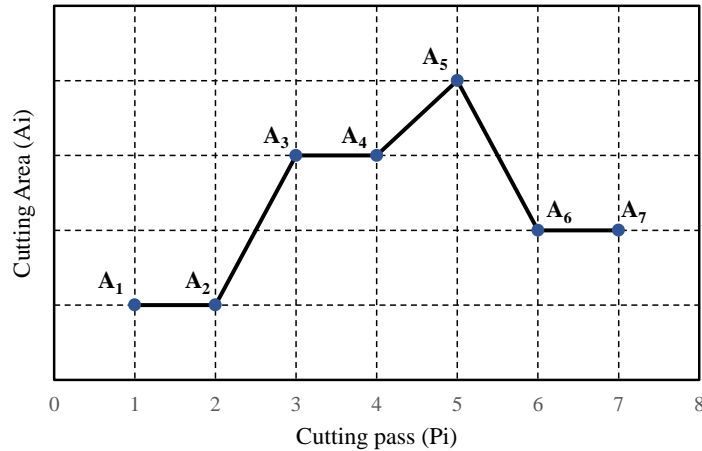
**Figure 4.5: Graphical representation of the dependence between cutting area and cutting pass for alternating flank cutting strategy**

## 4.1.2    Toolpath Planning

The analytical calculation of the cutting area allowed the tracing and storing of depths of cut. These were then used for the generation of NC code to be used for the machining of the grooves, as well as for an illustration of the tool path trajectory. For both activities, MatLab was as used a postprocessor. Moreover, cutting parameters such as feed rate during cutting engagement and retraction were also added in the postprocessor.

After the generation of the NC code, a tool path was plotted as shown in Figure 4.6. Since the tool path illustration is not a complete illustration of the cutting process, it was further verified with Vericut. The post processor flow for the alternating cutting strategy follows the same sequence ads one shown in the previous chapters.

Vericut allowed not only allowed the verification of the tool path, but it also allowed an accurate visualization of the V-groove structure created as illustrated in Figure 4.7. A constructed CAD model of the machining center allowed for the accurate simulation of the fabrication process of the V-groove microstructure using the NC code generated in Matlab.  After the simulation of the cutting process in Vericut, the NC code was iterated for any mistakes observed before loading it in the machining center. This guaranteed the

safety of the experiment as well as the avoidance of any unexpected error in the tool trajectory which would affect the resulting microstructure created.
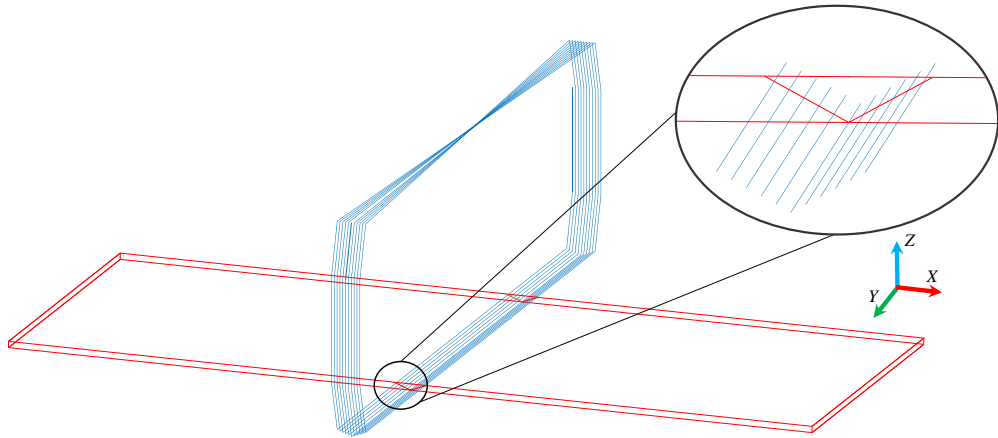


**Figure 4.6: Tool Path illustrator for CTC**

(a)  (b)

(c) (d)
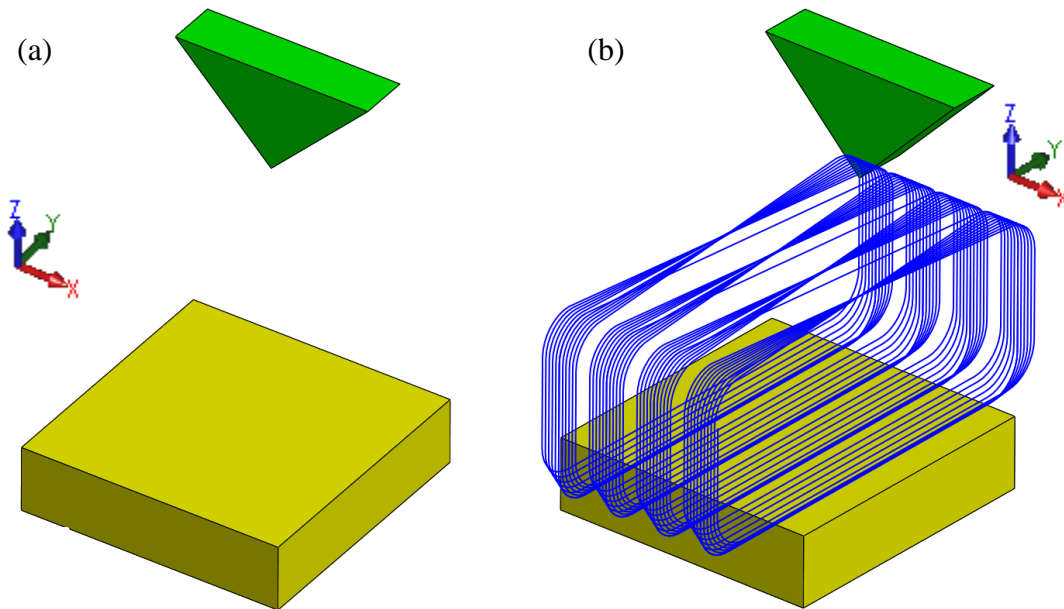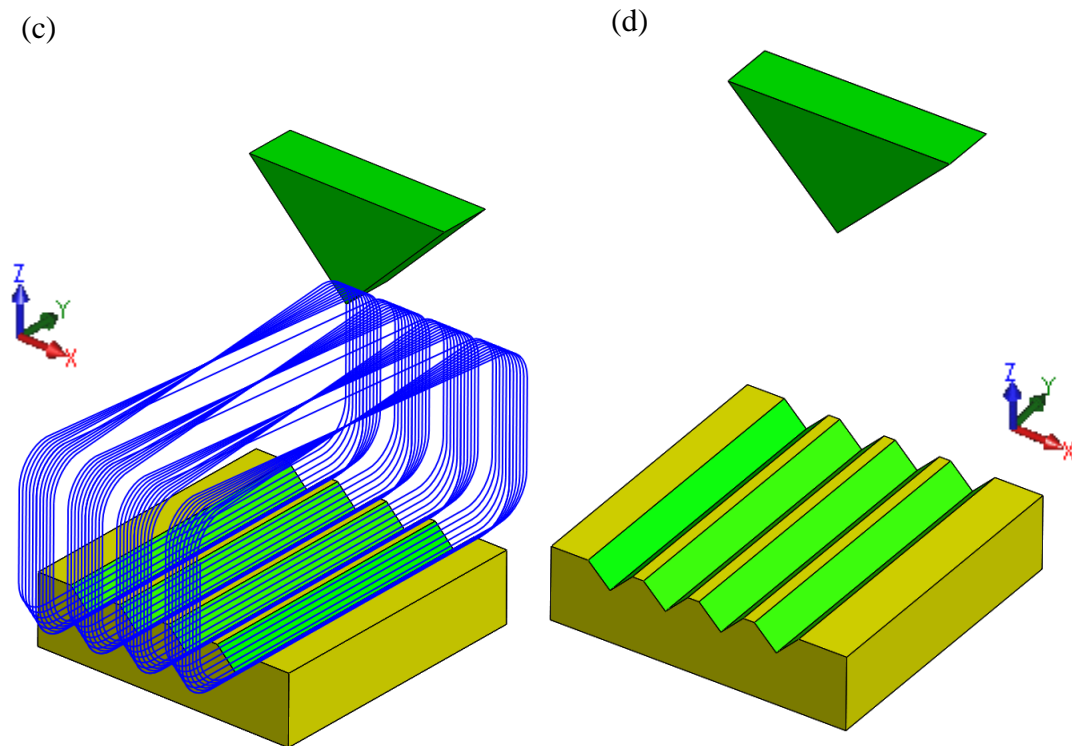


**Figure 4.7: Vericut fabricated V-grooves microstructures: (a) Uncut workpiece; b)**
**Illustration of toolpath; (c) Cut grooves with toolpath; (d) Final grooves**

## 4.1.3    Simulation methods

Here, the simulation was also run in Abaqus/Explicit with the same workpiece properties
and model setup presented in the previous chapters. Figure 4.8 illustrates the workpiece
with preexistent cuts and the partitions made. These cuts were made in order to avoid
remeshing complications. Moreover, they allowed the direct simulation of a specific
passes, representing rectangular areas rather than triangular ones. The mesh size
remained the same since the cut is also done with 15µm constant chip thickness. Passes
25 and 26 were selected for the simulation since the represent e first two passes after the
transition from triangular areas to rectangular areas occur. The

The results shown Figure 4.10 and Figure 4.11illustrate the formation of a continuous
chip as well as cutting forces within a 18% accuracy when compared to the experiment
results. In addition, they also illustrate the linear trend of the cutting force.
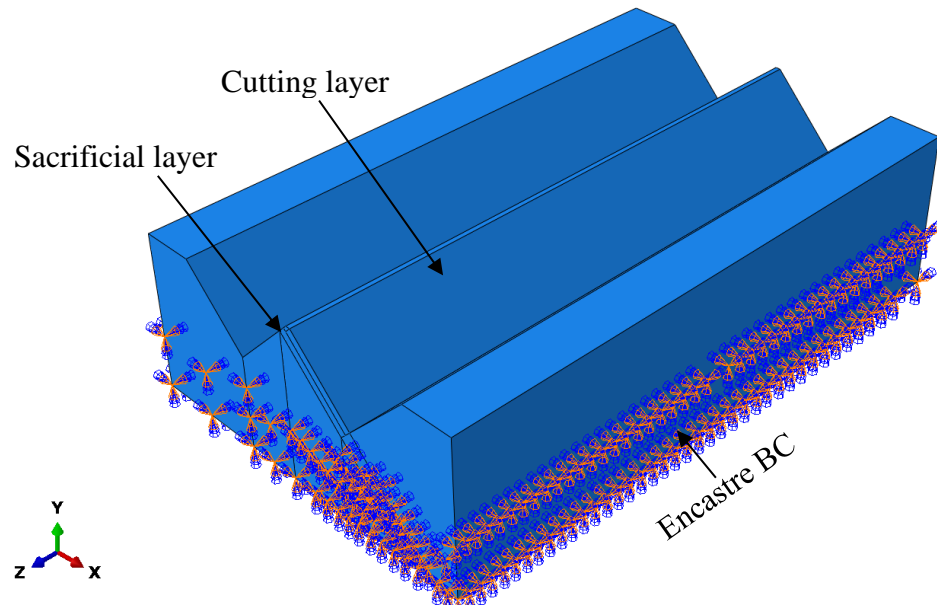
**Figure 4.8: Workpiece with BC and partitions**
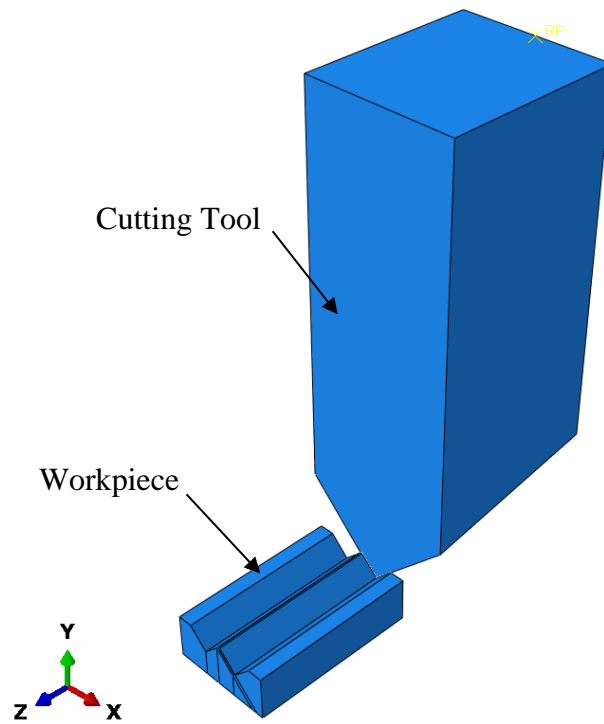


**Figure 4.9: Assembled model**
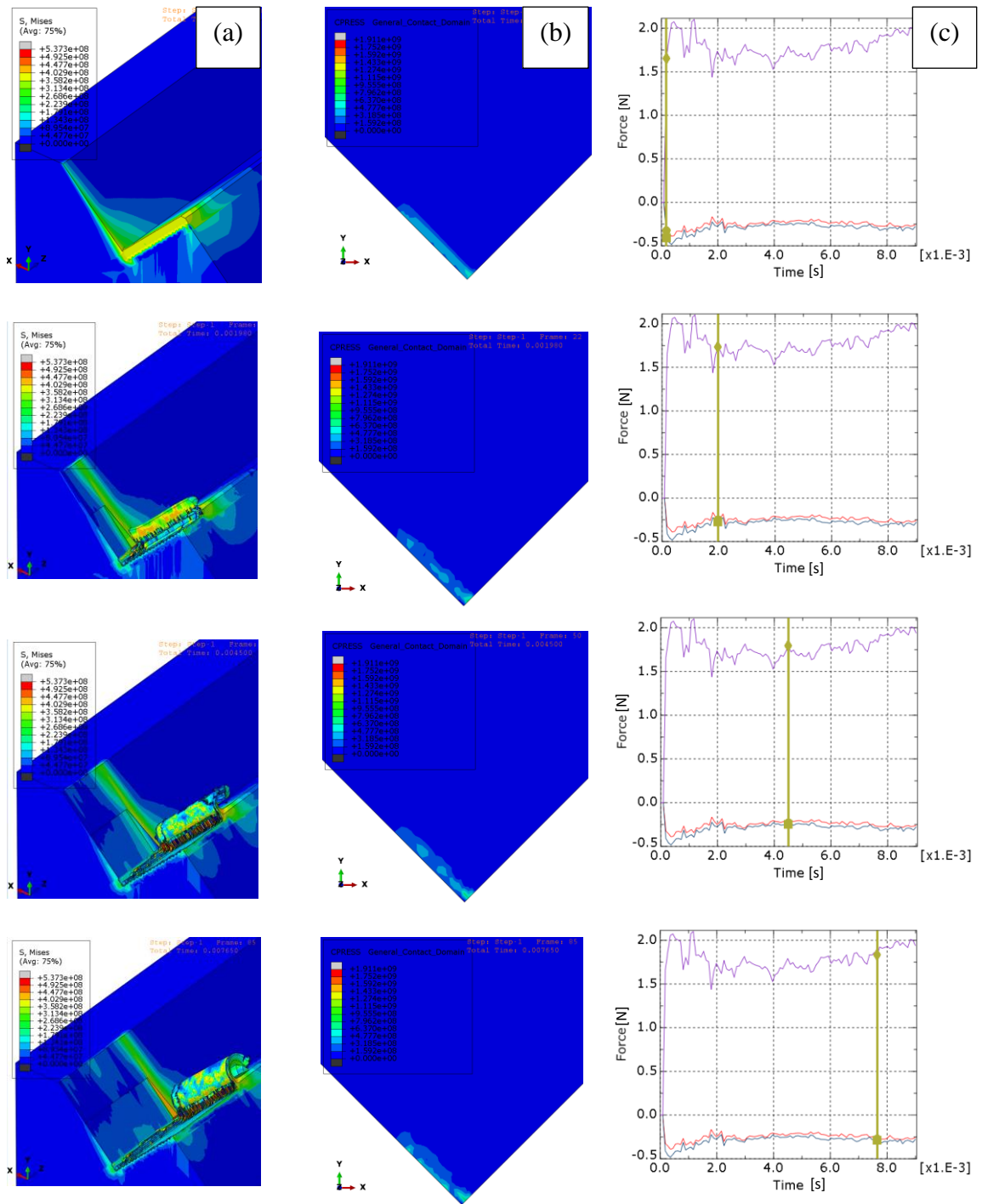
**Figure 4.10: Snapshots of FEA results for pass 25 of CCT: (a) workpiece; (b) Cutting tool: (c) Cutting forces**
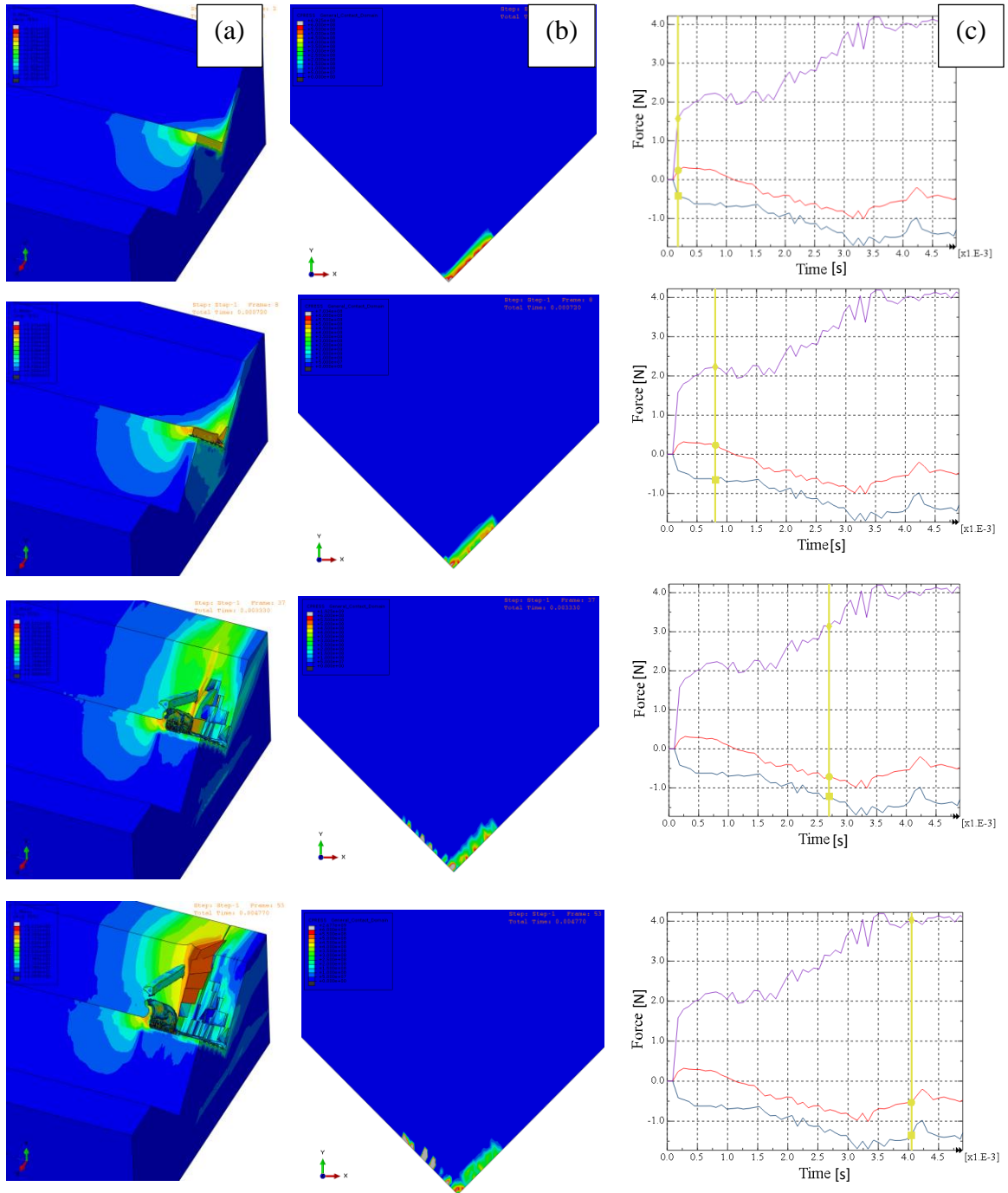
**Figure 4.11: Snapshots of FEA results for pass 26 of CCT: (a) workpiece; (b) Cutting tool: (c) Cutting forces**

Both passes across the workpiece reveal the loss of contact between the cutting tool and the workpiece. As mentioned before, this might explain the fluctuations of the cutting forces. However, further investigation needs to be done in order to confirm this.

### 4.1.4　Experimental Results and Analysis

Table 1 summarizes the experimental parameters used during the experiments involving the implementation of the alternating flank cutting strategy. The experiential setup used here was the same as the one described in chapter 2. All cutting trial were performed on an aluminum alloy 6061 workpiece. Following data acquisition procedure, advanced signal processing was applied to the recorded data using Matlab sofware. During the processing of the data, a moving average low pass filter was applied on the converted LabView-formatted data to filter the high-frequency noise.
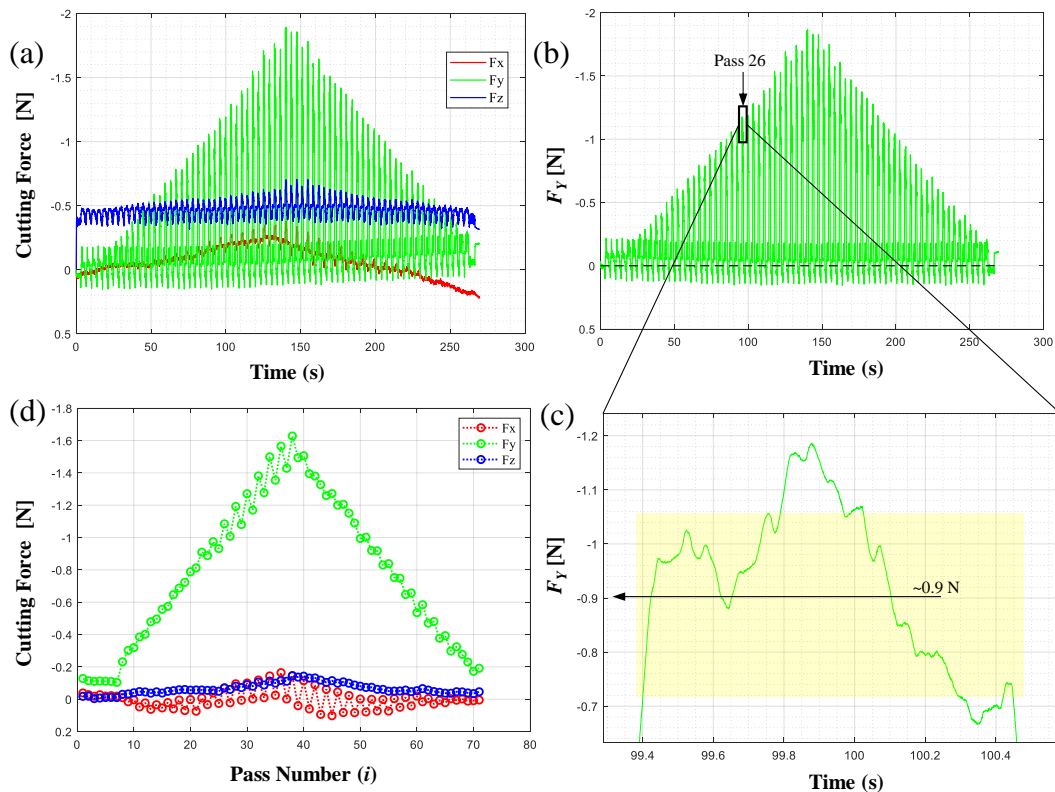


**Figure 4.12: Cutting force measurements for CTC: a) raw data; b) $F_Y$ with measurement drift corrected; c) sample of average $F_Y$ calculation; d) average cutting force components.**

**Table 4.1. Summary of experimental conditions**

| Feed rate (mm/min) | 500 |
|---|---|
| Chip thickness (µm) | 5, 10, 15 |
| Coolant | Isoparaffin mist |

A LabView-based data acquisition system was used to monitor and record cutting force measurements. Figure 4.12 depicts an overview of the results obtained for cuts performed with a 10 µm chip thickness.

Data filtering enabled the extraction of the quasi-static component of the cutting force (Figure 4.12a). Again, the analysis presented is focused on $F_Y$, since this represents the main contributor to the 3D cutting force magnitude as well as final surface quality of the V-groove facets. Each pulse in the cutting force signal (Figure 4.12a) represents a cut across the workpiece.
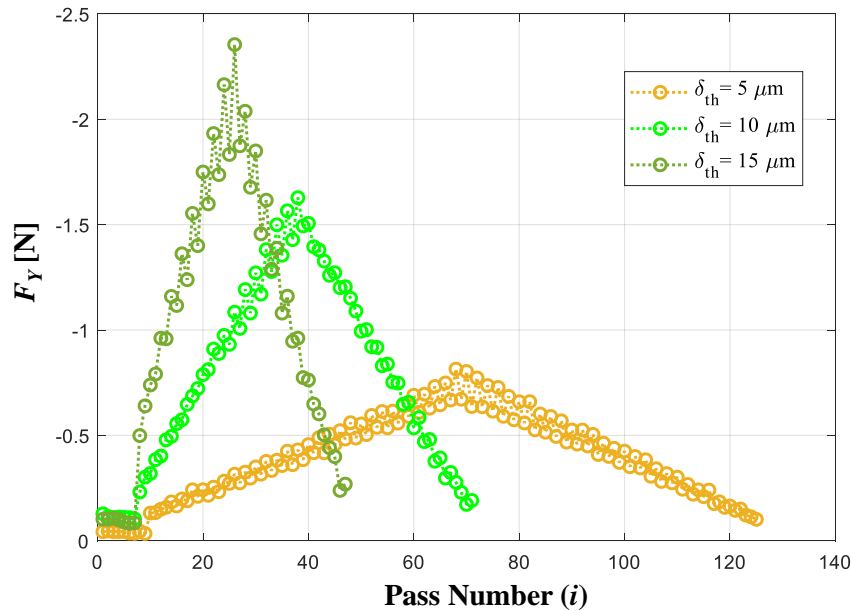


**Figure 4.13: Correlation between the main component of the cutting force and chip thickness**

The next step in the processing of the data followed the same sequence as the one presented on the previous chapters, going from the elimination of the cutting force drift introduced by the measuring system (Figure 4.12b) to the processing of the fluctuations

on each pulse as illustrated in Figure 4.12c. The average values for each cutting force component are presented in Figure 4.12d. $F_X$ demonstrates some fluctuations in the middle portion, that is during the transition from triangular areas to rectangular, however it negligible everywhere else. $F_Z$. however, is not negligible and shows a somewhat constant value. These values might be the result of friction in the rake face of the tool during cutting. According to the predictions presented in Figure 4.5, $F_Y$ component follows same dependence with respect to the cutting passes. In addition to this, a strict dependence to chip thickness also exists as shown in Figure 4.13.
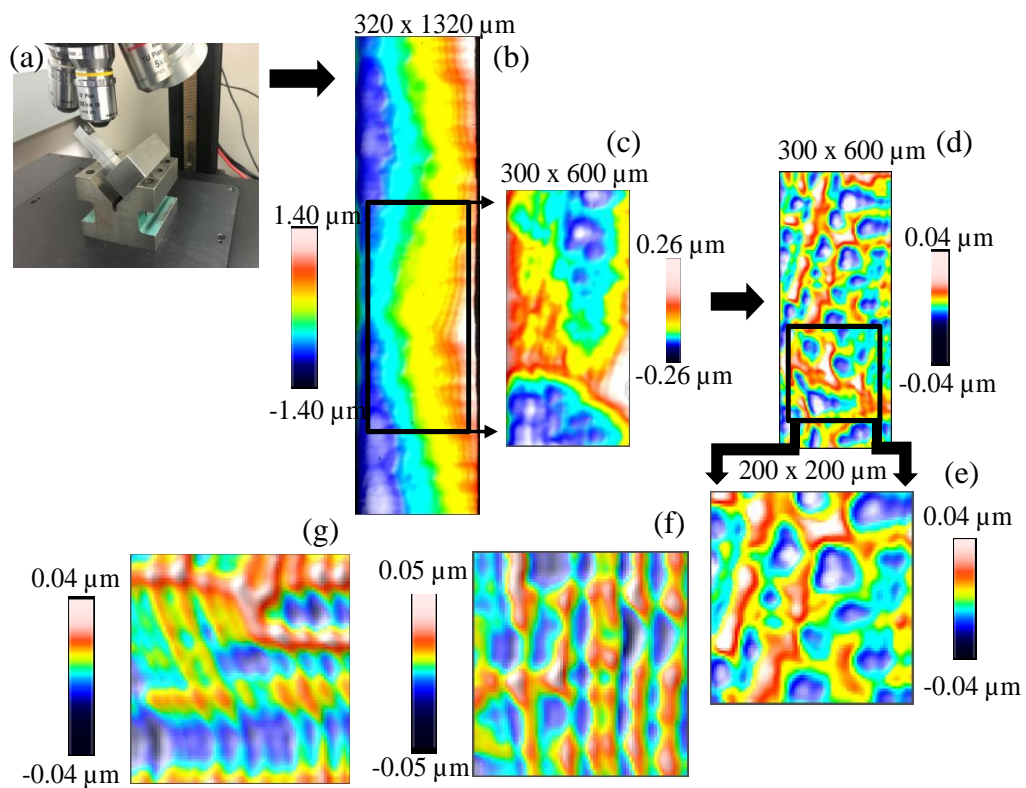


**Figure 4.14: Surface quality results for CTC: a) raw data; b) data with planar tilt removed; V-groove surface topography for: c) 5 μm chip thickness; d) 10 μm chip thickness; e) 15 μm chip thickness.**

Figure 4.13 illustrates the correlation between the main components of the cutting force and the chip thickness. Here, the same tradeoff between the low force magnitudes for lower chip thicknesses and short machining time for higher chip thicknesses is observed. However, the force magnitude gets one's attention, being very low. The maximum force reached with the current strategy is approximately 2.4N (Figure 4.13) for the thickest chip thickness. This is a significantly lower magnitude when compared to other strategies presented in the previous chapters. Moreover, the trend of the force illustrated when $\delta_{th}$=5µm is another interesting fact. The force level lies within an interval of approximately 0-0.8N. This could lead one to conclude that much lower chip thicknesses would result in a narrower interval, making the cutting force become constant.

In addition to the cutting force results, the surface of the micro grooves was assessed by means of an optical profilometer. The procedure here, was not different than the one presented on previous chapters. Starting from the tilt of the workpiece by a 45° angle to accurately measure the surface generated (Figure 4.14*a*), the effect of the effect of the remaining inclination was then removed through a planar removal technique (Figure 4.14*b*). Again, the last previous step was followed by the application of a filter with a cutoff wavelength of 80µm (ISO 16610-61) in order to eliminate surface waviness and retain only its roughness (Figure 4.14*d*). The final topographic data is shown in Figure 4.14*e*. The resulting roughness presented on Table 4.2 reveals that the cutting strategy is capable of producing ultraprecise surfaces.

**Table 4.2. Summary of surface quality measurements**

| Chip thickness (µm) | $S_a$ (nm) |
|---|---|
| 5 | 9.83 |
| 10 | 10.13 |
| 15 | 10.31 |

Chapter 5

# 5    Summary, Conclusions and Future Work

## 5.1   Summary and Conclusions

The work presented in this thesis outlines the development of three cutting strategies to be used during V-groove fabrication through ultraprecise single point cutting. The profile of the groove is produced by either maintaining a constant thickness of the cut or constant cutting area in the developed axial strategy and on-side cutting strategy. During the alternating flank cutting strategy, the profile of the groove is generated by maintaining a constant thickness of cut. The constant chip thickness implementation on both the axial and one-side cutting strategy revealed a linear relationship between the number of passes/depth of the cut and the magnitude of the cutting force as measured along the feed direction. The existence of this relationship is the result of the comparison performed between analytical and experimental results. This relationship is a consequence of the direct proportionality between the quasi-static components of the cutting force and the area and volume of material being removed at each pass. Moreover, a consistent/constant relationship exists between the number of passes/depth of the cut and the magnitude of the cutting force (as measured along the feed direction) for the constant cutting area implementation of both strategies. During the alternating flank cutting, however, an inconstant relationship was revealed. In this case, the relationship is a direct consequence of the increasing triangular area for a certain depth of cutting, followed by the decreasing rectangular area in the last part of cutting.

In addition, the results of the surface topography measurements have confirmed that all investigated strategies are not only capable of generating ultraprecise surfaces, but also that smaller chip thicknesses produce a better surface quality (as typically expected in common machining practice). The most significant contributions of the present study revolve around the analytical formulation presented for multi-pass single point cutting of V-grooves with constant chip thickness. The experimental data acquired on cutting force magnitude has validated the analytically inferred linear dependence between the area of the material being removed and depth of cut/number of passes. However, other effects –

that were potentially attributed to chip removal challenges and/or initial shock/contact between tool and workpiece – were also present in a sense that cutting forces did not have a perfectly constant magnitude during V-groove cutting.

The development of a CCA implementation for both axial and one-side cutting strategies enables the control of the cutting force, allowing avoidance tool breakage point and a better control of the final surface quality of the microgroove. Moreover, both one-side and the alternating flank cutting strategies have significant benefits not only on the magnitude of the cutting forces generated ($< 4$ N for $\delta_{th}= 15\mu$m), but also may bring significant reduction of burrs and improve the fabrication of high aspect rations grooves. The bending of the tips of the arrays could be significantly minimized with the innovative kinematics of both strategies. The low cutting force significantly affects the surface quality.

Even though the purpose of this work was not to rank the strategies in terms of which one is the best, it most certainly provides a toolbox with different strategies to be used dependent on the grooves geometry to be made.

## 5.2  Future Work

The analysis presented in the current study sets the foundation for further development of future and more efficient cutting strategies to be used in ultraprecise single point cutting of V-grooves. Among them, constant cutting area implementation of the alternating flank cutting strategy could represent an immediate investigational priority. Moreover, a development for process planning in multi-groove fabrication also constitutes as future work of this thesis. Here, the strategies' abilities for fabrication of high aspect ratio V-groove arrays could be explored, as well as functional surfaces with enhanced friction, wettability, and aerodynamics properties. This exploration will include scanning electron images (SEM) to better quantify the performance of the implementations of each strategy.

As a continuation of the work of this thesis, it is of value to also explore the cutting tool performance during the cutting process with each of the strategies. Tool breakage point

and tool wear are important parameters to explore both qualitatively and quantitively during the use of a constant chip thickness implementation and a constant cutting area. Further extension of this work also includes looking at the benefits of controlling stresses and cutting forces in a closed loop experimental setup.

Moreover, the simulation models have to be further improved to more closely match the acquired experimental results. Current results of the cutting force in the feed direction stand within an acceptable accuracy, however this could be improved.  With the improvement of the simulation models, a mesh sensitivity analysis could be performed. Moreover, different cutting speeds of the cutter could be simulated for different materials in order verify the generic application of the FEA model of each strategy at different cutting conditions. Furthermore, a detailed study of the friction coefficient in numerous cutting conditions is needed for its proper application on the FEA models.

The geometrical dimensions of the grooves are primarily determined by the included angle of the tool (90°). Therefore, another possible extension direction of this work could aim to observe the effect of different tool angles on cutting force magnitude and surface quality. Moreover, the effect of using asymmetrical tools is also worth to be explored, particularly since asymmetrical V-grooves are useful for some applications. Finally, the knowledge generated in this work could be used towards the efficient manufacturing of other types of microstructures whose geometry matches that of the tool (square, rectangular, profiled grooves, etc.)

# References

[1] Fang, F., Wu, H., Liu, X., Lim, G., Liu, Y., and Ng, S., "Fabrication of micro grooves," Proc. Proc ASPE 18th Annu Meeting, Portland, USA, Citeseer.

[2] BIDDUT, A. Q., 2006, "Micro-grooving on electroless nickel plated die materials."

[3] Zhang, P., Liu, H., Meng, J., Yang, G., Liu, X., Wang, S., and Jiang, L., 2014, "Grooved organogel surfaces towards anisotropic sliding of water droplets," Advanced Materials, 26(19), pp. 3131-3135.

[4] Zheng, Y., Bai, H., Huang, Z., Tian, X., Nie, F.-Q., Zhao, Y., Zhai, J., and Jiang, L., 2010, "Directional water collection on wetted spider silk," Nature, 463(7281), pp. 640-643.

[5] Bhushan, B., and Jung, Y. C., 2011, "Natural and biomimetic artificial surfaces for superhydrophobicity, self-cleaning, low adhesion, and drag reduction," Progress in Materials Science, 56(1), pp. 1-108.

[6] Ionov, L., Houbenov, N., Sidorenko, A., Stamm, M., and Minko, S., 2006, "Smart microfluidic channels," Advanced Functional Materials, 16(9), pp. 1153-1160.

[7] Zhao, Y., Lu, Q., Li, M., and Li, X., 2007, "Anisotropic wetting characteristics on submicrometer-scale periodic grooved surface," Langmuir, 23(11), pp. 6212-6217.

[8] Bain, C. D., Burnett-Hall, G. D., and Montgomerie, R. R., 1994, "Rapid motion of liquid drops," Nature, 372(6505), pp. 414-415.

[9] Feng, L., Li, S., Li, Y., Li, H., Zhang, L., Zhai, J., Song, Y., Liu, B., Jiang, L., and Zhu, D., 2002, "Super-hydrophobic surfaces: from natural to artificial," Advanced materials, 14(24), pp. 1857-1860.

[10] Yoshimitsu, Z., Nakajima, A., Watanabe, T., and Hashimoto, K., 2002, "Effects of surface structure on the hydrophobicity and sliding behavior of water droplets," Langmuir, 18(15), pp. 5818-5822.

[11] Sun, C., Zhao, X.-W., Han, Y.-H., and Gu, Z.-Z., 2008, "Control of water droplet motion by alteration of roughness gradient on silicon wafer by laser surface treatment," Thin Solid Films, 516(12), pp. 4059-4063.

[12] Fang, G., Li, W., Wang, X., and Qiao, G., 2008, "Droplet motion on designed microtextured superhydrophobic surfaces with tunable wettability," Langmuir, 24(20), pp. 11651-11660.

[13] Wu, D., Chen, Q.-D., Yao, J., Guan, Y.-C., Wang, J.-N., Niu, L.-G., Fang, H.-H., and Sun, H.-B., 2010, "A simple strategy to realize biomimetic surfaces with controlled anisotropic wetting," Applied Physics Letters, 96(5), p. 053704.

[14] Liu, L., Jacobi, A. M., and Chvedov, D., 2009, "A surface embossing technique to create micro-grooves on an aluminum fin stock for drainage enhancement," Journal of Micromechanics and Microengineering, 19(3), p. 035026.

[15] Walboomers, X. F., and Jansen, J. A., 2001, "Cell and tissue behavior on micro-grooved surfaces," Odontology, 89(1), pp. 0002-0011.

[16] Den Braber, E., De Ruijter, J., Ginsel, L., Von Recum, A., and Jansen, J., 1998, "Orientation of ECM protein deposition, fibroblast cytoskeleton, and attachment complex components on silicone microgrooved surfaces," Journal of Biomedical Materials Research: An Official Journal of The Society for Biomaterials, The Japanese Society for Biomaterials, and the Australian Society for Biomaterials, 40(2), pp. 291-300.

[17] Curtis, A., and Clark, P., 1990, "The effects of topographic and mechanical properties of materials on cell behavior," Crit. Rev. Biocompat, 5(4), pp. 343-362.

[18] Wojciak-Stothard, B., Curtis, A., McGrath, M., Sommer, I., Wilkinson, C., and Monaghan, W., 1995, "Role of the cytoskeleton in the reaction of fibroblasts to multiple grooved substrata," Cell motility and the cytoskeleton, 31(2), pp. 147-158.

[19] Dunn, G., and Brown, A., 1986, "Alignment of fibroblasts on grooved surfaces described by a simple geometric transformation," Journal of cell science, 83(1), pp. 313-340.

[20] Dalton, B. A., Walboomers, X. F., Dziegielewski, M., Evans, M. D., Taylor, S., Jansen, J. A., and Steele, J. G., 2001, "Modulation of epithelial tissue and cell migration by microgrooves," Journal of Biomedical Materials Research: An Official Journal of The Society for Biomaterials, The Japanese Society for Biomaterials, and The Australian Society for Biomaterials and the Korean Society for Biomaterials, 56(2), pp. 195-207.

[21] Walboomers, X., Ginsel, L., and Jansen, J., 2000, "Early spreading events of fibroblasts on microgrooved substrates," Journal of Biomedical Materials Research: An Official Journal of The Society for Biomaterials, The Japanese Society for Biomaterials, and The Australian Society for Biomaterials and the Korean Society for Biomaterials, 51(3), pp. 529-534.

[22] Walboomers, X., Croes, H., Ginsel, L., and Jansen, J., 1998, "Growth behavior of fibroblasts on microgrooved polystyrene," Biomaterials, 19(20), pp. 1861-1868.

[23] Vernon, R. B., and Sage, E. H., 1995, "Between molecules and morphology. Extracellular matrix and creation of vascular form," The American journal of pathology, 147(4), p. 873.

[24] Erickson, H. P., 1994, "Reversible unfolding of fibronectin type III and immunoglobulin domains provides the structural basis for stretch and elasticity of titin and fibronectin," Proceedings of the National Academy of Sciences, 91(21), pp. 10114-10118.

[25] Den Braber, E., De Ruijter, J., Ginsel, L., Von Recum, A., and Jansen, J., 1996, "Quantitative analysis of fibroblast morphology on microgrooved surfaces with various groove and ridge dimensions," Biomaterials, 17(21), pp. 2037-2044.

[26] Walboomers, X., Monaghan, W., Curtis, A., and Jansen, J., 1999, "Attachment of fibroblasts on smooth and microgrooved polystyrene," Journal of Biomedical Materials Research: An Official Journal of The Society for Biomaterials, The Japanese Society for Biomaterials, and The Australian Society for Biomaterials, 46(2), pp. 212-220.

[27] Chang, C.-H., 2007, "Light guide plate and backlight module using the same," Google Patents.

[28] Chien, C.-H., and Chen, Z.-P., 2007, "Design and fabrication of the concentric circle light guiding plate for LED-backlight module by MEMS technique," Microsystem technologies, 13(11-12), pp. 1529-1535.

[29] Chien, C. H., and Chen, Z. P., "Fabrication of integrated light guiding plate for backlight system," Proc. Micromachining and Microfabrication Process Technology XI, International Society for Optics and Photonics, p. 610909.

[30] Feng, D., Yan, Y., Yang, X., Jin, G., and Fan, S., 2005, "Novel integrated light-guide plates for liquid crystal display backlight," Journal of Optics A: Pure and Applied Optics, 7(3), p. 111.

[31] Beranek, M. W., Hager, H. E., and Chan, E. Y.-J., 1999, "Optical subassembly with a groove for aligning an optical device with an optical fiber," Google Patents.

[32] Lin, Y.-S., Huang, C.-C., Liu, M.-Y., Yang, J.-J., Mu, C.-K., and Huang, Y.-R., 2003, "Optical fiber alignment element using integrated micro ball lens," Google Patents.

[33] Brinksmeier, E., Gläbe, R., and Flucke, C., 2008, "Manufacturing of molds for replication of micro cube corner retroreflectors," Production Engineering, 2(1), pp. 33-38.

[34] Milliken, N., Hamilton, B., Hussein, S., Tutunea-Fatan, O. R., and Bordatchev, E., 2018, "Enhanced bidirectional ultraprecise single point inverted cutting of right triangular prismatic retroreflectors," Precision Engineering, 52, pp. 158-169.

[35] Hussein, S., Hamilton, B., Tutunea-Fatan, O. R., and Bordatchev, E., 2016, "Novel retroreflective micro-optical structure for automotive lighting applications," SAE International Journal of Passenger Cars-Mechanical Systems, 9(2016-01-1407), pp. 497-506.

[36] Viswanath, P., 2002, "Aircraft viscous drag reduction using riblets," Progress in Aerospace Sciences, 38(6-7), pp. 571-600.

[37] Bushnell, D., "Turbulent drag reduction for external flows," Proc. 21st Aerospace Sciences Meeting, p. 227.

[38] Hirchell, E., 1989, "1.3 Messerschmitt-Bblkow-Blohm GmbH Military Aircraft Division Postfach 80 11 60, D-8000 M'unchen 80, FRG 2 Messerschmitt-B61kow-Blohm GmbH," Fluid Dynamics of Three-Dimensional Turbulent Shear Flows and Transition.

[39] Robert, J., "Drag reduction: an industrial challenge. Special Course on Skin Friction Drag Reduction," AGARD.

[40] Coustols, E., and Savill, A., 1992, "Turbulent Skin Friction Drag Reduction By Active and Passive Means. Part 2," OFFICE NATIONAL D'ETUDES ET DE RECHERCHES AEROSPATIALES TOULOUSE (FRANCE).

[41] Lee, S.-J., and Jang, Y.-G., 2005, "Control of flow around a NACA 0012 airfoil with a micro-riblet film," Journal of fluids and structures, 20(5), pp. 659-672.

[42] Suzuki, H., Moriwaki, T., Yamamoto, Y., and Goto, Y., 2007, "Precision cutting of aspherical ceramic molds with micro PCD milling tool," CIRP annals, 56(1), pp. 131-134.

[43] Flucke, C., Gläbe, R., and Brinksmeier, E., ""Diamond Micro Chiselling of Molding Inserts for Optical Micro Structures"," Proc. Proceedings of the 23rd Annual Meeting and 12th ICPE, Portland, pp. 92-95.

[44] Moriya, T., Nakamoto, K., Ishida, T., and Takeuchi, Y., 2010, "Creation of V-shaped microgrooves with flat-ends by 6-axis control ultraprecision machining," CIRP annals, 59(1), pp. 61-66.

[45] Fang, F., and Liu, Y., 2004, "On minimum exit-burr in micro cutting," Journal of Micromechanics and Microengineering, 14(7), p. 984.

[46] Wang, S., To, S., Chen, X., Wang, H., and Xia, H., 2014, "A study of the fabrication of v-groove structure in ultra-precision milling," International Journal of Computer Integrated Manufacturing, 27(11), pp. 986-996.

[47] Wang, S. J., Chen, X., Liu, Q., Zhou, C. Q., Liu, J. Q., and Yin, Z. Q., 2018, "Development of a precision grinding machine system for the fabrication of micro V-grooves array," The International Journal of Advanced Manufacturing Technology, 97(5), pp. 2141-2150.

[48] Yan, J., Kaneko, T., Uchida, K., Yoshihara, N., and Kuriyagawa, T., 2010, "Fabricating microgrooves with varied cross-sections by electrodischarge machining," The International Journal of Advanced Manufacturing Technology, 50(9-12), pp. 991-1002.

[49] Peng, Y., Jiang, T., and Ehmann, K., 2014, "Research on single-point diamond fly-grooving of brittle materials," The International Journal of Advanced Manufacturing Technology, 75(9-12), pp. 1577-1586.

[50] De Chiffre, L., Kunzmann, H., Peggs, G., and Lucca, D., 2003, "Surfaces in precision engineering, microengineering and nanotechnology," CIRP Annals, 52(2), pp. 561-577.

[51] San Wong, Y., and Hong, G. S., 2011, "A novel method for determination of the subsurface damage depth in diamond turning of brittle materials," International Journal of Machine Tools and Manufacture, 51(12), pp. 918-927.

[52] Steinkopf, R., Scheiding, S., Gebhardt, A., Risse, S., Eberhardt, R., and Tünnermann, A., "Fly-cutting and testing of freeform optics with sub-um shape deviations," Proc. Current Developments in Lens Design and Optical Engineering XIII, International Society for Optics and Photonics, p. 84860K.

[53] Zhao, Q., Guo, B., Yang, H., and Zhang, X., "A mechanistic cutting force model for diamond fly-cutting of microstructured surface," Proc. 4th International Symposium on Advanced Optical Manufacturing and Testing Technologies: Advanced Optical Manufacturing Technologies, International Society for Optics and Photonics, p. 728204.

[54] Neo, W. K., Kumar, A. S., and Rahman, M., 2012, "A review on the current research trends in ductile regime machining," The International Journal of Advanced Manufacturing Technology, 63(5-8), pp. 465-480.

[55] Yin, S., Ohmori, H., Uehara, Y., Shimizu, T., and Lin, W., 2004, "Micro V-groove grinding technique of large germanium immersion grating element for mid-infrared spectrograph," JSME International Journal Series C Mechanical Systems, Machine Elements and Manufacturing, 47(1), pp. 59-65.

[56] Cheng, M., Cheung, C., Lee, W., To, S., and Kong, L., 2008, "Theoretical and experimental analysis of nano-surface generation in ultra-precision raster milling," International Journal of Machine Tools and Manufacture, 48(10), pp. 1090-1102.

[57] Yan, X., Shirase, K., Hirao, M., and Yasui, T., 1999, "NC program evaluator for higher machining productivity," International Journal of Machine Tools and Manufacture, 39(10), pp. 1563-1573.

[58] Brinksmeier, E., Mutlugünes, Y., Klocke, F., Aurich, J., Shore, P., and Ohmori, H., 2010, "Ultra-precision grinding," CIRP annals, 59(2), pp. 652-671.

[59] Ruckman, J., Fess, E., and Li, Y., "Contour mode deterministic microgrinding," Proc. Proc 14th Ann Meeting of ASPE, pp. 542-546.

[60] Joao, D., Milliken, N., Bordatchev, E. V., and Tutunea-Fatan, O. R., 2019, "Axial strategy for ultraprecise single point cutting of V-grooves Case 1: constant chip thickness," Procedia Manufacturing, 34, pp. 440-445.

[61] Joao, D., Milliken, N., Tutunea-Fatan, O. R., and Bordatchev, E. V., 2019, "One-Side Cutting Strategy for Ultraprecise Single Point Cutting of V-grooves Case 1: Constant Chip Thickness," IFAC-PapersOnLine, 52(10), pp. 306-310.

[62] Lee, J.-M., Je, T.-J., Choi, D.-S., Lee, S.-W., Le, D., and Kim, S.-J., 2010, "Micro grooving simulation and optimization in the roughing stage," International Journal of Precision Engineering and Manufacturing, 11(3), pp. 361-368.

[63] Opoz, T. T., and Chen, X., 2016, "Chip formation mechanism using finite element simulation," Strojniški vestnik-Journal of Mechanical Engineering, 62(11).

[64] Xie, J., Bayoumi, A., and Zbib, H., 1996, "A study on shear banding in chip formation of orthogonal machining," International Journal of Machine Tools and Manufacture, 36(7), pp. 835-847.

[65] Markopoulos, A., and Manolakos, D., 2010, "Finite element analysis of micromachining," J Manuf Technol Res, 2(1-2), pp. 17-30.

[66] Akram, S., Jaffery, S. H. I., Khan, M., Fahad, M., Mubashar, A., and Ali, L., 2018, "Numerical and experimental investigation of Johnson–Cook material models for aluminum (Al 6061-T6) alloy using orthogonal machining approach," Advances in Mechanical Engineering, 10(9), p. 1687814018797794.

# Curriculum Vitae

| | |
|---|---|
| **Name:** | Delfim Joao |
| **Post-secondary Education and Degrees:** | Western University<br>London, Ontario, Canada<br>2015-2019 B.E.Sc.<br><br>Western University<br>London, Ontario, Canada<br>2019-2020 M.E.Sc. |
| **Honours and Awards:** | Dean's Honor List<br>2015-2016, 2016-2017, 2017-2018, 2018-2019 |
| **Related Work Experience** | Research Assistant<br>Western University<br>2018-2020<br><br>Teaching Assistant<br>Western University<br>2019-2020 |

**Publications:**

**Joao, D.**, Milliken, N., Bordatchev, E. V., & Tutunea-Fatan, O. R. (2020). One-side cutting strategy for ultraprecise single point cutting of V-grooves. Submitted in Apr. 2020 to *Journal of International Computer Integrated Manufacturing*.

**Joao, D.**, Milliken, N., Bordatchev, E. V., & Tutunea-Fatan, O. R. (2020). Axial strategies for ultraprecise single point cutting of V-grooves. Accepted pending revisions in *Precision Engineering*.

**Joao, D.**, Milliken, N., Bordatchev, E. V., & Tutunea-Fatan, O. R. (2020). Ultraprecise Single Point Cutting of V-grooves with Constant Cutting Area. Submitted in Nov. 2020 to *ASME Journal of Macro and Nano Manufacturing*.

**Joao, D.**, Milliken, N., Bordatchev, E. V., & Tutunea-Fatan, O. R. (2019). One-Side Cutting Strategy for Ultraprecise Single Point Cutting of V-grooves Case 2: constant chip thickness. *Proceedings of the 34th Annual Meeting of the American Society of Precision Engineering (ASPE)*, Pittsburgh, USA, Oct. 2019, pp. 325-330.

**Joao, D.**, Milliken, N., Bordatchev, E. V., & Tutunea-Fatan, O. R. (2019). Axial strategy for ultraprecise single point cutting of V-grooves Case 2: constant cutting area. *USB Proceedings of the 3rd World Congress on Micro and Nano Manufacturing (WCMNM 2019)*, Sep. 2019, Raleigh, USA, pp. 330-334.

**Joao, D.**, Milliken, N., Tutunea-Fatan, O. R., & Bordatchev, E. V. (2019). One-Side Cutting Strategy for Ultraprecise Single Point Cutting of V-grooves Case 1: Constant Chip Thickness. *USB Proceedings of the 13th IFAC Workshop on Intelligent Manufacturing Systems (IMS 2019)*, Aug. 2019, Oshawa, Canada, pp. 312-316.

**Joao, D.**, Milliken, N., Bordatchev, E. V., & Tutunea-Fatan, O. R. (2019). Axial strategy for ultraprecise single point cutting of V-grooves Case 1: constant chip thickness. *Procedia Manufacturing*, **34:**440-445 (*Proceedings of the 47th North American Manufacturing Research Conference (NAMRC 47)*, Jun. 2019, Erie, USA).

**Joao, D.**, Milliken, N., Tutunea-Fatan, O.R., Bordatchev, E.V., 2019, "Axial Strategy for Ultraprecise Single Point Cutting of V-grooves with Constant Cross-Sectional Cutting Area," USB Proceedings of the 2019 International Congress of Canadian Society for Mechanical Engineering (CSME 2019), Jun. 2019, London, Canada, pp. 152.